UNIVERSIDAD AUTÓNOMA DE BAJA CALIFORNIA
INSTITUTO DE INGENIERÍA
MAESTRÍA Y DOCTORADO EN CIENCIAS E INGENIERÍA

THESIS

"Low-dimensional II-VI group semiconductor heterostructures development for photosensitive materials application."

In fulfillment of the requirements for the degree of

DOCTOR OF PHILOSOPHY

Present

Laura Alejandra Reyes Verdugo

Adviser

Dr. Carlos Villa Angulo

Mexicali, B. C. México ***August 2020***

Dedicatoria

Dedico este trabajo primeramente a Dios, quien ha puesto los medios, me ha dado las fuerzas y sabiduría para llevar a cabo este proyecto.

A mis hijos Keiel y Nicolás, la razón y motor de mi vida.

A mi madre, quien con su apoyo y amor incondicional me ha ayudado a salir adelante.

Por qué su existencia en mi vida, hace que esta tenga sentido y me motiva e impulsa a continuar día a día.

Gracias, les amo.

Agradecimientos

A Dios, por medio de quien todo esto ha sido posible.

Al Dr. Carlos Villa Angulo por la oportunidad y confianza que depositó en mi para el desarrollo de este proyecto.

A mis mentores, compañeros, colegas y amigos de cada uno de los laboratorios donde se me dio la oportunidad de trabajar, colaborar y desarrollar este trabajo de investigación:

- *A la Universidad Autónoma de Baja California y al programa de Maestría y Doctorado en ciencias e Ingeniería (MYDCI) por promover y facilitar mi superación profesional y académica.*
- *Instituto de Ingeniería de la UABC; laboratorio de Física Aplicada, Laboratorio de bioinformática, Laboratorio de semiconductores, microelectrónica y nanotecnología LSMN, así como todos mis compañeros de laboratorio.*
- *Dr. Jaime Álvarez Quintana, laboratorio de Transferencia de Calor y Carga a Nanoescala en CIMAV-Unidad Monterrey y a mis compañeros de laboratorio.*
- *Dra. Harumi Moreno, Coordinación para la Innovación y Aplicación de la Ciencia y la Tecnología (CIACYT)*
- *Dr. Eduardo Pérez Tijerina, Dr. Claudio Gutiérrez Lazos, Dr. Abel Fundora, D. Francisco Solis, Dr. Mitchel Ruiz, Paulina, Laboratorio de nanociencias y nanotecnología, Facultad de Físico-matemático de la UANL*
- *Ph. D. Ethan Ahn, Nanoelectronics Lab in the Electrical and Computer Engineering (ECE) Department, The University of Texas at San Antonio y a mis compañeros de laboratorio.*

A todos ustedes, por darme la oportunidad de formar parte de su equipo, por su orientación y apoyo en cada paso, por sus enseñanzas tanto en cuestiones técnicas como en el plano humano y por su ejemplo de responsabilidad y dedicación al trabajo.

De manera personal a todos esos amigos especiales que me han apoyado en los momentos difíciles y han celebrado conmigo los éxitos, les amo y les llevo en el corazón. Jhonathan, Victor quienes me han mostrado que aún hay amigos sinceros.

Finalmente al Consejo Nacional de Ciencia y Tecnología por el apoyo económico que me brindaron para la manutención de mis familia durante estos años de formación doctoral y la oportunidad de realizar estudios en el extranjero.

Content

Figure index

Table Index

Abstract

It has been demonstrated that the integration of nanostructured materials in photovoltaic devices opens up the possibility of developing low-cost solar cells. In recent years there has been increasing interest in the nanostructured semiconductors thin films. They are in an outstanding situation in the basic research and solid-state technology due to their future applications in quantum and photonic devices [1, 2].

In the present work, low dimensional II-VI group semiconductor heterostructured devices have been designed, fabricated, and characterized by different deposition techniques as Chemical bath Deposition, Thermal Evaporation, and RF Sputtering Deposition techniques.

The most novel structure developed and proposed in the present study TCO/CdS/CdSe/ $CdSe_{0.6}Te_{0.4}$/CdSe/Ag showed an increment in Voc, compare to a well-studied structure as TCO/CdS/CdSe/Ag, from 0.58 V to 1.54 V, as well as an increment in Jsc from 14.68 mA/cm^2 to 21.11 mA/cm^2. Such increments represent power conversion efficiency (PCE) in the systems of 3.1% to 11.6% respectively. Such increment in the PCE of the novel structure proposed can be attributed to the insertion of the 18 nm $CdSe_{0.6}Te_{0.4}$ thin film within the depletion region of the p-type CdS and n-type CdSe interface.

This study has demonstrated the feasibility of combining techniques in order to achieve better properties in photosensitive materials applications such as Low-dimensional II-VI group semiconductor heterostructures devices. Further work needs to be done in order to find all the experimental details that could lead us to have higher efficiencies, better properties, and stability as lower fabrications costs.

Resumen

Se ha demostrado que la integración de materiales nanoestructurados en dispositivos fotovoltaicos abre la posibilidad de desarrollar celdas solares de bajo costo. En los últimos años, el interés en los semiconductores nanoestructurados con películas delgadas ha crecido. Se encuentran en una situación destacada en las investigaciónes actuales en la tecnología de estado sólido debido a sus aplicaciones en dispositivos cuánticos y fotónicos [1, 2].

En el presente trabajo, se han diseñado, fabricado y caracterizado dispositivos heteroestructurados semiconductores de baja dimensión del grupo II-VI mediante diferentes técnicas de depósito, como lo son: Baño químico, Evaporación térmica y Erosión iónica de RF.

La estructura más novedosa desarrollada y propuesta en el presente estudio TCO / CdS / CdSe / $CdSe_{0.6}Te_{0.4}$ / CdSe / Ag en comparación con una estructura bien estudiada como TCO / CdS / CdSe / Ag, mostró un incremento en Voc de 0.58 V a 1,54 V, así como un incremento en Jsc de 14,68 mA / cm^2 a 21,11 mA / cm^2. Dichos incrementos representan la eficiencia de conversión de energía (PCE) en los sistemas de 3,1% a 11,6% respectivamente. Tal incremento en el PCE de la nueva estructura propuesta puede atribuirse a la inserción de la película delgada de 18 nm $CdSe_{0.6}Te_{0.4}$ dentro de la región de agotamiento de la interfaz de CdS de tipo p y CdSe de tipo n.

Este estudio ha demostrado la viabilidad de combinar técnicas para lograr mejores propiedades en aplicaciones de materiales fotosensibles tales como dispositivos de heteroestructuras semiconductoras de baja dimensión de grupo II-VI. Es necesario realizar más estudios más para encontrar todos los detalles experimentales que podrían llevarnos a tener mayores eficiencias, mejores propiedades y estabilidad como menores costos de fabricación.

Chapter 1

Introduction

"I want to know how God created this world. I am not interested in this or that phenomenon. I want to know His thoughts, the rest are details."

Albert Einstein

1.1 II-VI group semiconductors Overview

1.1.1 Cadmium and lead chalcogenides and their technological relevance and properties

In the last decade, biomedical, clean energy, electronics, and optoelectronics industry have increased their attention in techniques used to synthesize and deposit semiconducting nanoparticles because of their feasibility to produce more efficient and cheaper thin-film devices [3-5]. The interest in nanoparticles is because of their magnetic, electrical, optical, chemical, and physical properties that are unique. In addition, the high demand for clean energy has promoted the increase of interest in versatile materials and cost-effective synthesis techniques for thin-film photovoltaic applications [6 – 9]. The functionality and efficiency of optoelectronics, photovoltaic, and electronic devices based on thin-film technologies depend strongly on the properties of the semiconductor materials. Especially, semiconducting materials comprising compounds of elements II and VI groups of the periodic table such as CdSe, CdS, ZnS, and PbS have demonstrated excellent properties for the fabrication of low dimensional multilayer devices [10 – 14].

Heterostructures of cadmium sulfide (CdS), cadmium telluride (CdTe), cadmium selenide (CdSe) and their ternary mixed crystals with direct bandgap are fabricated by low-temperature deposition techniques where the internal and external surfaces are intrinsically well passivated and are characterized by a low recombination velocity for the excess carriers [8, 9].

This property allows the use of these compound materials to build a multi-junction structure with a band-gap gradient aiding the collection of excess carriers and hence facilitating the development of optoelectronics and photovoltaic devices [13 – 15].

In particular, CdS is a binary compound used as window material in thin-film optoelectronics and photovoltaic devices [16]. It has excellent properties as heterojunction material with CdSe and CdTe [16- 19]. CdS is widely used as an n-type semiconductor with a direct bandgap of 2.42 eV and an appropriate optical absorption in the short wavelength range of the visible spectrum [20]. Heterojunctions of CdS, CdSe and CdTe have been obtained by deposition and synthesis techniques such as chemical bath deposition [11, 12], electrochemical deposition [13], solvothermal deposition [14, 15], sol-gel deposition [16, 17], and spin coating, among others [18]. Although these heterojunctions are being obtained by different techniques, the non-uniform morphology of nanospheres reduces the quality of the deposited thin films affecting the desired performance of devices.

Along with the different compound materials synthesis (binary, ternary, quaternary, etc.), as well as deposition techniques; the device structures have been studied to improve the performance of photonic detectors (photodetectors, solar cells, etc.). Especially, wide bandgap II-VI semiconductors are in the forefront of materials that are being studied for photonic devices where applications such as light-emitting and light-absorption are being explored [19]. Cadmium selenium-telluride ($CdSe_xTe_{1-x}$) has received much attention due its chemical stability [20], high optical absorption [21], less toxicity [22], and the possibility of tuning the crystal structure and band-gap (from 0.9 to 1.74 eV) [23, 24] by changing the concentration of Se and Te. $CdSe_xTe_{1-x}$ thin films have been deposited by different methods such as electrodeposition [25, 26], thermal vapor deposition [27], painting and slurry [28], sintering process [29], hot wall deposition technique [30], metal-organic chemical vapor deposition [31], among others.

1.1.2 Cadmium sulfide (CdS)

Cadmium sulfide is an inorganic compound with the chemical formula CdS. It is a yellow solid and a semiconductor of electricity. It occurs in nature with two different polymorphs, cubic hawleyite, and hexagonal greenockite.

Greenockite is a hexagonal, yellowish crystal. It is a rare mineral and is the only real ore of cadmium. It is a much sought after mineral because of its beautiful color and crystal habit. It has the same structure as that of zinc-iron sulfide wurtzite.

Other applications of cadmium sulfide are listed below:

- Photoresistors,
- Thin film transistors,
- Transducers,
- Solar cells,
- Electrochemical deposition,
- Sol-gel techniques,
- Screen printing.
- Others.

The chemical, electrical, thermal, mechanical, and optical properties of cadmium sulfide are provided in the tables below [32]:

Table 1-1: Chemical properties of cadmium sulfide.

Chemical Properties	
Chemical Formula	CdS
Molecular Weight	144.48
CAS No.	1306236
Group	Cadmium 12 Sulfur 16
Crystal Structure	Hexagonal, Cubic
Lattice Constants	a=4.160 Å c=6.756 Å

Table 1-2: Electrical properties of cadmium sulfide.

Electrical Properties	
Dielectric Constant	8.9
Band Gap	2.42 eV
Electron Mobility	350 cm^2/Vs
Hole Mobility	40 cm^2/Vs

Table 1-3: Thermal properties of cadmium sulfide.

Thermal Properties	
Thermal Expansion Coefficient	a_1 =6.26 x10^{-6} /K a_3 =3.5x10^{-6} /K
Specific Heat Capacity	0.47 J/gK
Thermal Conductivity	40.1 W/mK

Table 1-4: Mechanical properties of cadmium sulfide.

Mechanical Properties	
Young's Modulus	45 Gpa
Melting Point	1750°C
Boiling Point	980°C
Density	4.826 g/cm^3

Table 1-5: Optical properties of cadmium sulfide.

Optical Properties	
Refractive Index	2.529

1.1.3 Cadmium Selenide (CdSe)

Cadmium selenide is a solid, binary compound of cadmium and selenium. It is an n-type semiconducting material that is transparent to infrared light. However, p-

type doping of cadmium selenide occurs using nitrogen. Wurtzite, sphalerite, and rocksalt are the three known crystalline forms of cadmium selenide.

Cadmium is a toxic heavy metal, and selenium is toxic in large amounts. Hence cadmium selenide is a known carcinogen to humans, and medical attention is required if swallowed or when eyes and skin come in contact with it. Most of the current research works are focused on developing controlled synthesis of cadmium selenide nanoparticles.

Cadmium selenide finds applications in:

- Optoelectronic devices
- Laser diodes
- Biomedical imaging
- Nanosensing
- High-efficiency solar cells
- Thin-film transistors

The chemical, electrical, thermal, mechanical, and optical properties of cadmium selenide are provided in the tables below [33]:

Table 1-6: Chemical properties of cadmium selenide.

Chemical Properties	
Chemical Formula	CdSe
Molecular Weight	191.37
CAS No.	1306247
Group	Cadmium 12 Selenium 16
Crystal Structure	Wurtzite

Table 1-7: Electrical properties of cadmium selenide.

Electrical Properties

Dielectric Constant	10.2
Band Gap	1.74 eV
Electrical Resistivity	a) low: < 1 Ω cm b) high: > 10^{12} Ω cm

Table 1-8: Thermal properties of cadmium selenide.

Thermal Properties	
Thermal Expansion Coefficient	a_1 =6.26 x10^{-6} /K
Specific Heat Capacity	0.49 J/gK
Thermal Conductivity	40.1 W/mK

Table 1-9: Mechanical properties of cadmium selenide.

Mechanical Properties	
Young's Modulus	5x10^{11} dyne/cm^2
Melting Point	1268°C

Table 1-10: Optical properties of cadmium selenide.

Optical Properties	
Refractive Index	2.5

1.1.4 Cadmium Telluride (CdTe)

Cadmium telluride is a crystalline compound formed from cadmium and tellurium. It is sandwiched with calcium sulfide to form a PN junction photovoltaic solar cell. It has very low solubility in water and is etched by many acids such as hydrobromic and hydrochloric acids. It is commercially available as powder or crystals. It can also be made into nanocrystals.

Cadmium telluride finds applications in:

- Thin-film solar cells
- Infrared optics
- Detectors

- Electro-optic modulators
- Crystal pieces for vacuum deposition

The chemical, electrical, thermal, mechanical, and optical properties of cadmium telluride are provided in the tables below [34]:

Table 1-11: Chemical properties of cadmium Telluride

Chemical Properties	
Chemical Formula	CdTe
Molecular Weight	240.01
CAS No.	1306258
Group	Cadmium 12 Tellurium 16
Crystal Structure	cubic
Lattice Constants	6.48 Å

Table 1-12: Electrical properties of cadmium Telluride

Electrical Properties	
Dielectric Constant	10.2
Band Gap	1.44 eV
Electron Mobility	65 cm^2/Vs
Hole Mobility	700 cm^2/Vs

Table 1-13: Thermal properties of cadmium Telluride

Thermal Properties	
Thermal Expansion Coefficient	5.9×10^{-6} /K
Specific Heat Capacity	0.21 J/gK
Thermal Conductivity	0.06 W/mK

Table 1-14: Mechanical properties of cadmium Telluride

Mechanical Properties	
Young's	3.7×10^{11}

Modulus	dyne/cm^2
Melting Point	1092°C
Boiling Point	1130°C
Density	5.85 g/cm^3

Table 1-15: Optical properties of cadmium Telluride

Optical Properties	
Refractive Index	2.67

1.1.5 Lead sulfide (PbS)

Lead sulfide is an inorganic compound with the chemical formula PbS. It is also known as galena, which is the principal ore and important compound of lead. It is one of the earliest materials to be used as a semiconductor as it tends to crystallize in sodium chloride. Lead sulfide is toxic if it is heated to decomposition, which forms lead and sulphur oxides.

- Lead sulfide finds applications in the following:
- Infrared detectors
- Photo-optic applications
- Slip property modifier used in the friction industry for enhancing heat conduction and regulating friction coefficient.

The chemical, electrical, thermal, mechanical, and optical properties of Lead Sulfide are provided in the tables below [35]:

Table 1-16: Chemical properties of Lead Sulfide

Chemical Properties	
Chemical Formula	PbS
Molecular Weight	239.30
CAS No.	1314870
Group	Lead 14 Sulphur 16
Crystal Structure	cubic
Lattice Constants	5.936 Å

Table 1-17: Electrical properties of Lead Sulfide

Electrical Properties	
Band Gap	0.37 eV
Electron Mobility	600 cm2/Vs
Hole Mobility	600 cm2/Vs

Table 1-18: Thermal properties of Lead Sulfide

Thermal Properties	
Heat of Fusion	72 J/g
Heat of Formation	435 kJ/mol
Thermal Conductivity	2.30 W/mK

Table 1-19: Mechanical properties of Lead Sulfide

Mechanical Properties	
Density	7.61 g/cm^3
Melting Point	1117°C

Table 1-20: Optical properties of Lead Sulfide

Optical Properties	
Refractive Index	3.91

1.1.6 Cadmium selenium-telluride ($CdSe_xTe_{1-x}$)

It is well known that constructing ternary semiconductor alloys (ABxC1−x) is another efficient way to increase the absorption in the visible light region. During the alloying process, the compositional effect mainly originates from the strong dependence of the energy level on the effective mass of excitons, which will then affect the absorption and band-edge photoluminescence properties of the excitons [36].

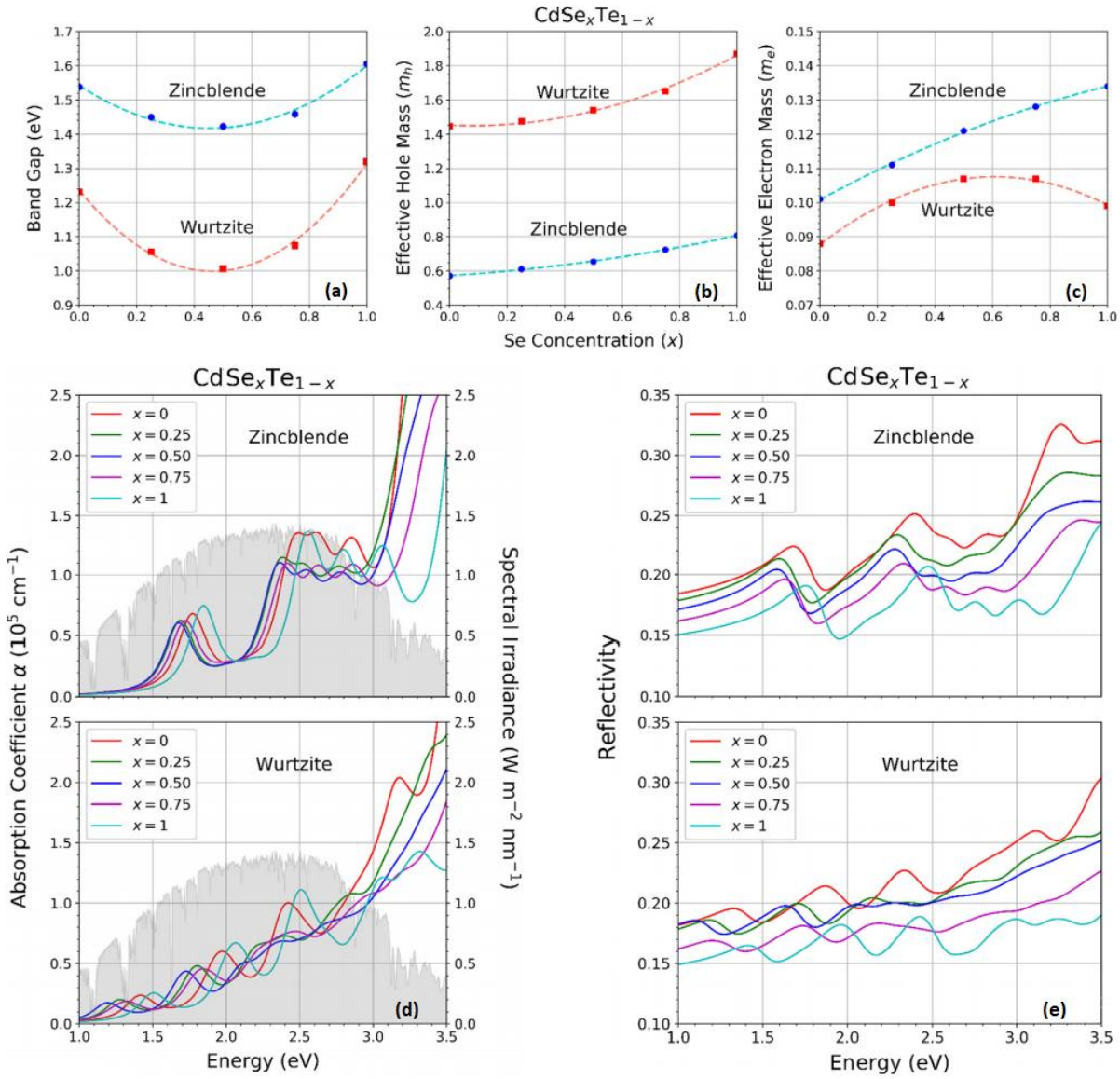

Fig. 1-1 (a) Electronic band gaps, (b) effective hole masses, and (c) effective electron masses of zincblende and wurtzite $CdTe_{1-x}Se_x$. (d) Absorption coefficients (α) of zincblende (top panel) and wurtzite (bottom panel) $CdTe_{1-x}Se_x$. Each absorption curve, with values given on the left y-axis, corresponds to a given concentration (x). For comparison, the standard AM 1.5 solar spectrum is represented by the shaded area with values given on the right y-axis. (e) Reflectivity of zincblende (top panel) and wurtzite (bottom panel) $CdTe_{1-x}Se_x$. Each reflectivity curve, with values given on the left y-axis, corresponds to a given concentration (x).

The II-VI ternary semiconductor alloys are used in optoelectronic devices ranging from blue to near-ultraviolet spectral region [37]. Cadmium chalcogenides CdTe, CdSe and their mixed ternary crystals $CdSe_xTe_{1-x}$ have semiconducting properties, which are especially suitable for the conversion of solar energy to electrical energy in photovoltaic or photoelectrochemical devices.

Theoretical research showed that according to the optical bowing effect, the bandgap of $CdSe_XTe_{1-X}$ varies nonlinearly and may be tuned to a value smaller than those of both CdSe (Eg: 1.7 eV) and CdTe (Eg: 1.5 eV), i.e. the absorption edge of the CdSeTe alloy can be tuned to UV or IR region [38].

Although some experimental and theoretical studies have been performed on $CdSe_xTe_{1-x}$ mixed crystals, many fundamental properties of these materials remain to be determined precisely. Fig 1-1 is showing Electronic band gaps, effective hole masses, effective electron masses, Absorption coefficients (α), and Reflectivity. Each curve [39], with values given on the left y-axis, corresponds to a given concentration (x).

1.2 Justification of the Project

Although amorphous silicon is the leading thin-film photovoltaic (PV) material, research is underway with other promising materials such as II-VI group semiconductors ones.

The functionality and efficiency of optoelectronics, photovoltaic, and electronic devices based on thin-film technologies depend strongly on the properties of the semiconductor materials.

According to the latest best research-cell efficiencies in fig. 1-2 driven by the National Renewable Energy Laboratory, the devices included in the chart of the current state of the art have efficiencies that are confirmed by independent,

recognized test labs—e.g., NREL, AIST, and Fraunhofer—and are reported on a standardized basis. Providing Cell efficiency results within families of semiconductors as Multijunction cells, single-junction gallium arsenide cells, Crystalline silicon cells, Thin-film technologies, Emerging photovoltaic.

A Closer Look Leading Thin-film technologies with II-VI group semiconductor materials research focuses on addressing critical portions of binary or ternary compounds device heterostructure, including the transparent conducting oxide (TCO) layer, the cadmium sulfide (CdS) window layer, the CdTe, CdSe or CdS_xTe_{1-x} as absorber layer, and the back contact.

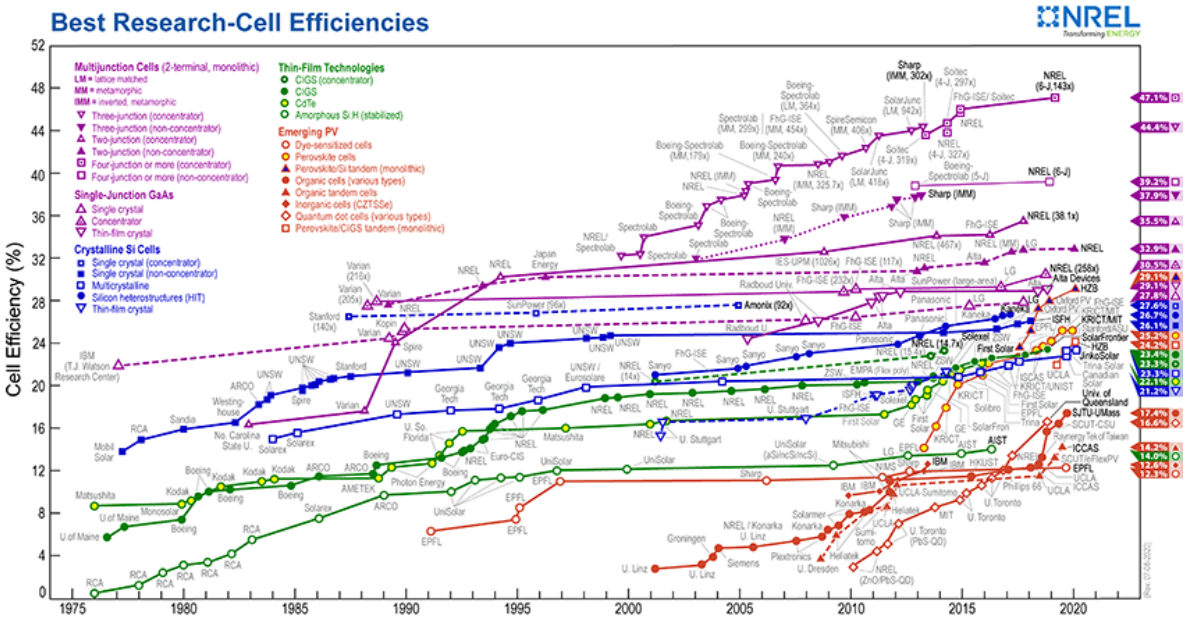

Fig. 1-2 Best research-cell efficiencies by NREL.

Heterostructures with this design are fabricated by deposition techniques where the internal and external surfaces are intrinsically well passivated and are characterized by a low recombination velocity for the excess carriers [8, 9].

This property allows the use of these compound materials to build a multi-junction structure with a band-gap gradient aiding the collection of excess carriers and hence facilitating the development of optoelectronics and photovoltaic devices [13 - 15].

Along with the different compound materials synthesis (binary, ternary, quaternary, etc.), as well as deposition techniques; the device structures have been studied to improve the performance of photonic detectors (photodetectors, solar cells, etc.). Especially, wide bandgap II-VI semiconductors are at the forefront of materials that are being studied for photonic devices where applications such as light-emitting and light-absorption are being explored [23].

1.3 Overall objective

This research is directed at developing reproducible processes for the fabrication of low dimensional II-VI group semiconductor heterostructured devices, as well as developing alternative processes that can improve device performance, reproducibility, and manufacturability.

1.3.1 Specific objectives

1. Design, fabricate and characterize low dimensional II-VI group semiconductor heterostructured devices by different deposition techniques as Chemical bath Deposition, Thermal Evaporation, and RF Sputtering Deposition techniques.
2. Comparison of the electrical properties in the devices developed by design and fabrication technique, analyzing:
    a. Transparent conducting oxide layers. Compare different TCO coated glass substrates establishing the best electrical response. Working to develop and integrate high performance, next-generation TCO materials into baseline device structures for superior performance or manufacturability.
    b. CdS/window layers. Develop a better understanding of how window layers lose current, as well as improved processes for depositing and pre-treating cadmium sulfide.

c. Absorbers and junctions. work to improve device performance by compositionally engineering CdS, CdTe, CdSe, PbS, $CdSe_xTe_{1-x}$ interfaces, and developing high-performance deposition and post-deposition processes that are fast, reproducible, and manufacturable.
d. Back contacts. Work is underway to develop high performance back contacts that are reproducible, manufacturable, and stable.

1.4 Hypothesis

In conventional PV cells, an nm-thick P-type semiconducting film is placed in between the P-type and N-type semiconductor materials so as to increases the short - circuit current density (Jsc) by increasing light absorbance, this a spite of decreasing the open-circuit voltage (Voc).

Unlike the former PV cells, a novel architecture proposed presents the P-type semiconducting film buried away from the P-N interface, which increases significant light absorbance.

The device presents a fourfold increment in power conversion efficiency regards to conventional ones. Such increment is mainly awarded to the increment in Jsc and Voc rather than significant differences in the fill factor. The present strategy shed a light in order to increase the PCE in PV cells and can provide avenues to achieve high-performance PV cells via a buried P-type layer away from the P-N interface as a light absorber.

1.5 References

[1] M.M.Abbas, A. Ab-M.Shehab, N-A.Hassan and A-K.Al-Samurae 2011 Effect of temperature and deposition time on the optical properties of chemically deposited nanostructure PbS thin films Thin Solid Films 519 4917-4922.

[2] Solis-Pomar, F., Fundora, A., Menchaca, J. L., Melendrez, M., & Perez, E. (2018). Study of the structural properties of nanostructured PbS thin films deposited by RF sputtering at room temperature. Materials Research Express. doi:10.1088/2053-1591/aadac0

[3] Hanemann, T., & Szabó, D. V. "Polymer-Nanoparticle Composites: From Synthesis to Modern Applications. Materials, 3(6), 3468–3517. (2010). doi:10.3390/ma3063468

[4] Lee, Y.-C., Kuo, T.-J., Hsu, C.-J., Su, Y.-W., & Chen, C.-C. "Fabrication of 3D Macroporous Structures of II−VI and III−V Semiconductors Using Electrochemical Deposition. Langmuir, 18(25), 9942–9946. (2002). doi:10.1021/la020296h

[5] Prakash, G. V., Singh, R., Kumar, A., & Mishra, R. K. "Fabrication and characterisation of CdSe photonicstructures from self-assembled templates. Materials Letters, 60(13-14), 1744–1747. (2006). doi:10.1016/j.matlet.2005.12.067

[6] B. X. Hop, et al. Growth of CdS thin films by chemical bath deposition technique". VNU Journal of Science, Mathematics - Physics 24 119-123. (2008)

[7] Ristić, M., Popović, S., Ivanda, M., & Musić, S. "A simple route in the synthesis of CdS nanoparticles. Materials Letters, 109, 179–181. (2013). doi:10.1016/j.matlet.2013.07.081

[8] Breen, M. L., Woodward, Schwartz, D. K., & Apblett, A. W. "Direct Evidence for an Ion-by-Ion Deposition Mechanism in Solution Growth of CdS Thin Films. Chemistry of Materials, 10(3), 710–717. (1998). doi:10.1021/cm970351l

[9] Gaeeni, M. R., Tohidian, M., & Majles-Ara, M. "Green Synthesis of CdSe Colloidal Nanocrystals with Strong Green Emission by the Sol–Gel Method.

Industrial & Engineering Chemistry Research, 53(18), 7598–7603. (2014). doi:10.1021/ie5004398

[10] Li, H., & Liu, X. " Improved performance of CdTe solar cells with CdS treatment. Solar Energy, 115, 603– 612. (2015). doi:10.1016/j.solener.2015.02.044

[11] Niitsoo, O., Sarkar, S. K., Pejoux, C., Rühle, S., Cahen, D., & Hodes, G. "Chemical bath deposited CdS/ CdSe-sensitized porous TiO2 solar cells. Journal of Photochemistry and Photobiology A: Chemistry, 181 (2-3), 306–313. (2006). doi:10.1016/j.jphotochem.2005.12.012

[12] Al-Hussam, A. M. A., & Jassim, S. A.-J. "Synthesis, structure, and optical properties of CdS thin films nanoparticles prepared by chemical bath technique. Journal of the Association of Arab Universities for Basic and Applied Sciences, 11(1), 27–31. (2012). doi:10.1016/j.jaubas.2011.10.001

[13] MacDonald, B. I., Martucci, A., Rubanov, S., Watkins, S. E., Mulvaney, P., & Jasieniak, J. J. (2012). "Layer-by-Layer Assembly of Sintered CdSexTe1–x Nanocrystal Solar Cells. ACS Nano, 6(7), 5995–6004. (2012). doi:10.1021/nn3009189

[14] Lee, S., Flanagan, J. C., Kang, J., Kim, J., Shim, M., & Park, B. "Integration of CdSe/CdSe x Te1−x Type-II Heterojunction Nanorods into Hierarchically Porous TiO2 Electrode for Efficient Solar Energy Conversion. Scientific Reports, 5(1). (2015). doi:10.1038/srep17472

[15] Obaid, A. S., Hassan, Z., Mahdi, M. A., & Bououdina, M. "Fabrication and characterisations of n-CdS/p-PbS heterojunction solar cells using microwave-assisted chemical bath deposition. Solar Energy, 89, 143–151. (2013). doi:10.1016/j.solener.2012.12.010

[16] Mohamed, H. A. "Optimized conditions for the improvement of thin film CdS/CdTe solar cells. Thin Solid Films, 589, 72–78. (2015). doi:10.1016/j.tsf.2015.04.081

[17] P.A Salaoru, et al. “Preparation and structural characterization of thin-film CdTe/CdS heterojunctions” Journal of optoelectronics and advance materials 2006, Vol. 8, No. 3, p. 936 – 940.

[18] Quiñonez-Urias, D., Vera-Marquina, A., Berman-Mendoza, D., Leal-Cruz, A. L., García-Delgado, L. A., Zaldívar-Huerta, I. E., Gómez-Fuentes, R. “Annealing effect on structural, morphological, and optical behaviors of CBD-CdS nanostructured films for solar cells. Optical Materials Express, 4(11), 2280. (2014). doi:10.1364/ome.4.002280

[19] R. P. Dutta and P. K. Saikia, “An electrical and Structural Studies of multilayer of CdS, CdTe and ZnSe thin films deposited by thermal evaporation method” International Journal of Innovative Research & Development 1, 73–82, 2012. DOI: 10.1007/s13204-012-0150-4

[20] Shinde, S. K., Thombare, J. V., Dubal, D. P., & Fulari, V. J.., “Electrochemical synthesis of photosensitive nano-nest like CdSe0.6Te0.4 thin films” Applied Surface Science 282, 561–565, 2013. DOI:10.1016/j.apsusc.2013.06.010

[21] S.K. Shinde, G.S. Ghodake, Dk.P. Dubal, H.D. Dhaygude, D.-Y. Kim, V.J. Fulari, “Enhanced photoelectrochemical properties of nanoflower-like hexagonal CdSe0.6Te0.4: Effect of electron beam irradiation” Journal of industrial and Engineering Chemistry 45, 92–98, 2017. DOI: 10.1016/j.jiec.2016.09.007

[22] S. K. Shinde, G. S. Ghodake, N. C. Maile, H. D. Dhaygude, Sungyeol Kim, A. D. Phule, Rahul V. Patel, D. Y. Kim, V. J. Fulari “Porous CdSe0.6Te0.4 nanoflowers-nanosphere: facile electrochemical synthesis and excellent for photoelectrochemical cell performance” Ionic 23(9), 2489–2496, 2017. DOI:10.1007/s11581-017-2077-y

[23] L. D. Budyonnaya, A. M. Pavelets, L. N. Khanat, V. E. Badan, “A study of photosensitive sintered films of CdSexTe1-x solid solutions” Thin Solid Films 138(2), 163–169, 1986. DOI:10.1016/0040-6090(86)90390-1

[24] B. Ermolovich, A. M. Pavelets and L. N. Khanat, “Mechanisms of the temperature quenching of luminescence due to deep centers in CdSexTe1-x (0 x < 1) alloys” Thin Solid Films 146(3), 233–239, 1987. DOI:10.1016/0040-6090(87)90430-5

[25] K. Adaikalam, M.R. Kim, Y.S. Chae, J.K. Rhee, S.Thanikaikarasan, T. Mahalingam, “Study on electrodeposited CdSexTe1-x semiconducting thin films” Journal of Electroanalytical Chemistry and Interfacial Electrochemistry 269(2), 399–410, 1989. DOI:10.1016/0022-0728(89)85147-2

[26] Z. Loizos, N. Spyrellis, G. Maurin, D. Pottier, “Semiconducting CdSexTe1-x thin films prepared by electrodeposition” Journal of Alloys and Compounds 505(2), 578, 1989. DOI:10.1016/j.jallcom.2010.06.136

[27] S. A. Fayek and S. M. El Sayed, “Effect of composition and forming parameter on evaporated CdSeTe films deposited at room temperature” Journal of Physics and Chemistry of Solids 63(1), 1-8, 2002. DOI: 10.1016/S0022-3697(00)00029-9

[28] G. Hodes, “A thin-film polycrystalline photoelectrochemical cell with 8% solar conversion efficiency” Nauture 285, 29–30, 1980. DOI: 10.1038/285029a0

[29] L. Kumar, B. P. Singh, A. Misra, S.C.K. Misra, T.P. Sharma, “Characterization of CdSexTe1-x sintered films for photovoltaic applications” Physica B 363, 102–199 (205), 2005. DOI:10.1016/j.physb2005.03.008

[30] S. Velumani, M. Xavier and P. J. Sebastian, “Structural and optical characterization of hot wall deposited CdSe x Te 1− x films” Solar Energy Materials and Solar Cells 76(3), 359-368, 2003. DOI:10.1016/S0927-0248(02)00288-X

[31] Danielson, A. Munshi, D. Swanson, J. Drayton, G. Kartopu, K. Barth, S. Irvine, W. Sampath., “MOCVD deposition of group V doped CdTe sublimated and CdSeTe devices” IEEE 7th World Conference on Photovoltaic Energy Conversion (WCPEC) 978-1-5386-8529-7/18/2018. DOI:10.1109/PVSC.2018.8547722

[32] AzoM (2013, April 19). Cadmium Sulfide (CdS) Semiconductors. https://www.azom.com/article.aspx?ArticleID=8407

[33] AzoM (2013, April 11). Cadmium Sulfide (CdSe) Semiconductors. https://www.azom.com/article.aspx?ArticleID=8406

[34] AzoM (2013, April 11). Cadmium Sulfide (CdTe) Semiconductors https://www.azom.com/article.aspx?ArticleID=8408

[35]AzoM (2013, August 23). Lead (II) Sulfide (PbS) Semiconductors https://www.azom.com/article.aspx?ArticleID=8440

[36] Wang, X., Xu, Y., Tong, R., Zhou, X., Li, Q., & Wang, H. (2015). Compositional effects and optical properties of CdSexTe1−x alloyed nanotube arrays. CrystEngComm, 17(4), 960–966. doi:10.1039/c4ce01982b

[37] C.G. Van der Walle, Wide Band-gap Semiconductors, North Holland, Amsterdam, 1993.

[38] Hannachi, L., & Bouarissa, N. (2008). Electronic structure and optical properties of CdSexTe1−x mixed crystals. Superlattices and Microstructures, 44(6), 794–801. doi:10.1016/j.spmi.2008.09.013

[39] Dumre, B. B., Szymanski, N. J., Adhikari, V., Khatri, I., Gall, D., & Khare, S. V. (2019). Improved optoelectronic properties in $CdSe_xTe_{1-x}$ through controlled composition and short-range order. Solar Energy, 194, 742–750. doi:10.1016/j.solener.2019.10.091

Chapter 2

Theoretical Framework

"Religion and science demand for their foundation of faith in God. For the former (religion), God stands foremost; for the latter (science), at the end of all thought, for religion, He represents a basis; for science, a crowning solution towards a world view."

Max Planck (d. 1947), the founder of quantum physics and one of the most important physicists of the twentieth century.

2.1 Introduction

Materials with a nanoscale structure comparable with the de Broglie wavelength of electrons or the optical wavelengths of high energy photons are subjected to principles of the quantum mechanical motion rather than classical mechanics. The effects in the optical, electronic, or mechanical properties are unique and have been widely studied in the last decade for many applications.

The dimension of materials at the nanoscale can be tuned to create a space confinement effect called quantum confinement. In semiconductor heterostructures, quantum confinement significantly modifies the properties of excitons, since is related to its degrees of freedom. The Impact of quantization effects in confinement becomes really important when one of the particle dimensions of a semiconductor is below the bulk semiconductor Bohr exciton radius which makes materials properties size-dependent. In general, the Bohr radius of a particle is defined as:

$$a_B = \mathcal{E}\frac{m}{m^*}a_0 \qquad (2\text{-}1)$$

Where $\mathcal{E}$ is the dielectric constant of the material is, m^* is the effective mass of the particle m is the rest mass of the electron, and a_0 is the Bohr radius of the hydrogen atom. When the particle size approaches Bohr exciton radius, the quantum confinement effect causes increasing of the excitonic transition energy and blue shift in the absorption and luminescence bandgap energy [1].

The consequence of this confinement in space is the quantization of the carries energy and linear momentum. The motion of electrons in the confined space can be modeled by the motion of a particle in a potential well with finite walls. In addition, this phenomenon leads the continuous energy bands of bulk material into discrete energy bands, like energy levels, as shown in Fig. 2-1. The same behaviour is observed in the absorption spectrum for bulk and confinement.

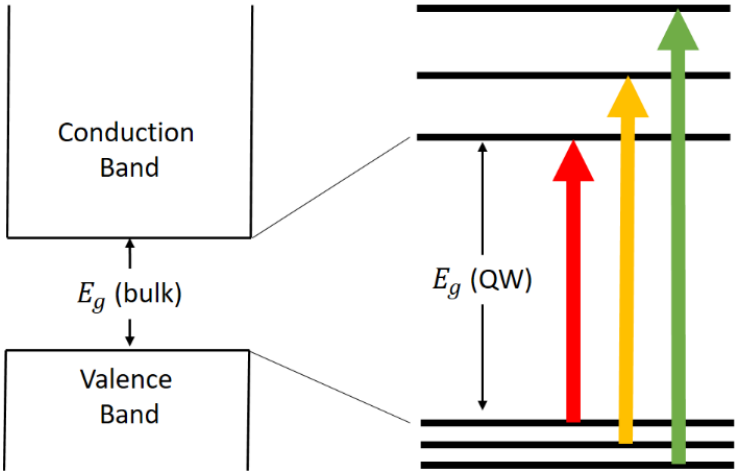

Fig.2-1. A schematic of the discrete energy level of a semiconductor

2.2 Low dimensional heterostructure

Low-dimensional heterostructured functional materials have been widely applied in new energy devices. These materials have, at least an ultra-small dimension. As a result of these changes in the atomic structure, the behaviour of its physical properties changes as well, laying between of an individual atom and a bulk material [2].

For typical semiconductor groups of IV, III-V, and II-VI, the length scale from 1 to 25 nm corresponding to the regimen of quantum confinement ranges. In which the spatial extent of the electronic wave function is comparable with the particle size. Further, electrons are under the effect of the particle boundaries and respond to changes in particle size by adjusting their energy. This phenomenon is known as the quantum size effect.

In low-dimensional structures (quantum-confined structure) the motion of the carriers is confined in one or more directions by potential barriers [3]. Based on the confinement direction, a quantum-confined structure will be classified into three categories so-called two-dimensional (2D) systems which include thin films, layer structures, and quantum wells and superlattices; the one-dimensional (1D) systems such as those solids in which linear chain-like structures can be identified,

and semiconductor wires (quantum wire) and zero-dimensional (0D) systems such as clusters, quantum dots, nanocrystals, and colloids. Cluster systems can be thought of as having properties intermediate between molecular and bulk systems [1]. The basic type of quantum confined structure is shown in Table 2-1.

Table 2-1: Classification of quantum confined structures.

Structure	Quantum Confinement	Free Dimension
Bulk	0	3D
Quantum well	1	2D
Quantum wire	2	1D
Quantum dot	3	0D

In quantum well, a higher concentration of charge carriers (pair electrons-holes) can contribute to the band-edge emission, as the density of electronic states near the edges of the conduction and valence bands is higher [4]. Therefore the energy level of one of the quantum numbers changes from continuous to discrete. The carriers are confined to move in a plane and are free to move in a two-dimensional.

As more number of the dimension is confined, more discrete energy levels can be found. The density of electron states in bulk, quantum well, wires and dot semiconductor structures are shown in Fig. 2-2.

The quantum confinement effect corresponding to the size of the nanostructure can be estimated through the simple "particle in a box" model (effective-mass approximation) [5, 6] in one dimension for the particle of interest (e.g., electron or hole).

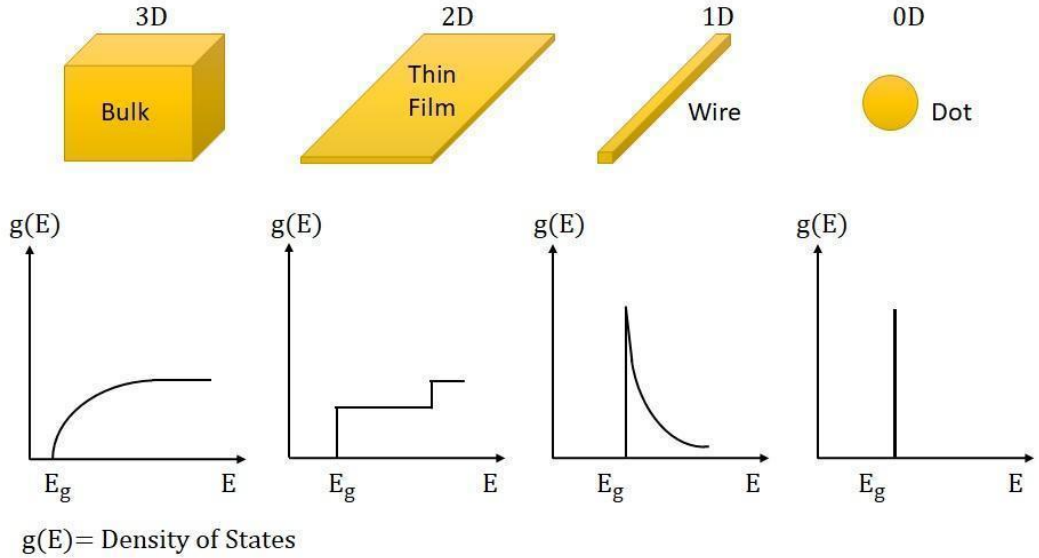

Fig. 2-2: Density of electron states of a semiconductor as a function of the dimension. The optical absorption spectrum is roughly proportional to the density of states.

2.2.1 Quantum wells (QW's)

A quantum well is a particular kind of heterostructure formed with alternating layers of semiconductor materials with different bandgaps, in which one thin "well" layer (smaller bandgap) is surrounded by two "barrier" layers named as "potential well". In this layer, both electrons and holes are confined in typically about 100 Å or about 40 atomic layers wall width (d).

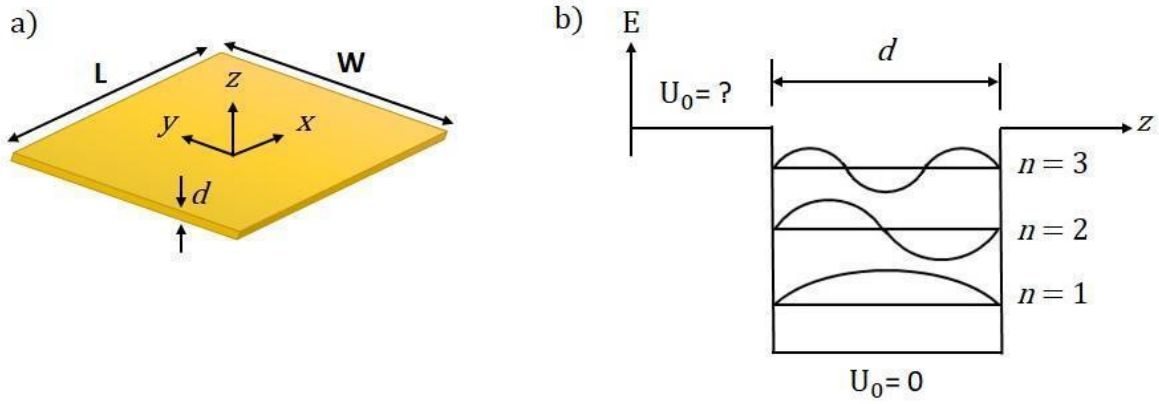

Fig. 2-3 (a) Schematic presentation of a quantum well (2D), and (b) the quantum numbers of an electron in the quantum well.

In Quantum well, the allowed states, correspond to standing waves in the direction perpendicular to the layers [7]. When such confinement occurs in one dimension, with free motion in the x- and y-directions, a two-dimensional system is created, which is shown in Fig. 2-3 (a).

In a quantum well width d, the density of states (DOS) per unit area is

$$g_0(E) = \frac{m_d^*}{\pi\hbar^2} \qquad (2\text{-}2)$$

Where $m_d^* = \sqrt{m_x m_y}$, which is called the 2D DOS effective mass. The confined energy E_0 for n = 1 is defined by

$$E_0 = \frac{\pi^2\hbar^2}{2m_z d^2} \qquad (2\text{-}3)$$

The simplest case is shown in Fig. 2-3 (b). In this "infinite well" case, we presume for simplicity that the barriers on either side of the quantum well are infinitely high. Then the wave function must be zero at the walls of the quantum well. The solution is then particularly simple.

The energy levels (or "confinement energies") are quadratically spaced, and the wave functions are sine waves. In eq 2-3, the energy is referred to the energy of the bottom of the well. Note that the first allowed energy (corresponding to n=1) is above the bottom of the well. We see that the energy level spacing becomes large for narrow wells (small Lz) and small effective mass m [8].

For energy $E<E_0$, there are no states. For energy $E<E_0<4E_0$, the density of states per unit area is just for a perfect two-dimensional electron. For energy $4E_0<E<9E_0$, the density of states per unit area is $2g_0$. For energy $9E_0<E<16E_0$, the density of states per unit area is $3g_0$ (Fig. 2-4).

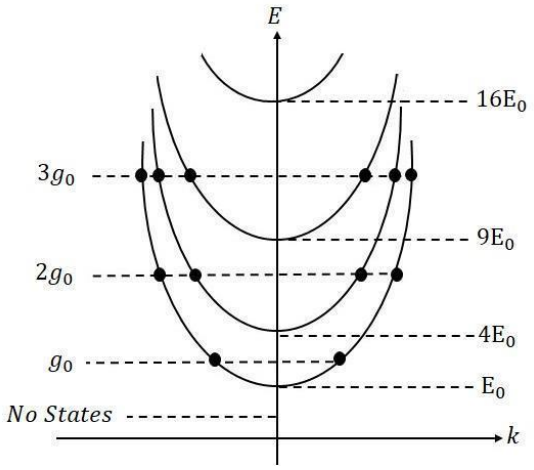

Fig. 2-4 Energy versus wavenumber k for a quasi-quantum well

To convert the density of states per unit area to a density of states per unit volume (Fig. 2-5), we must divide by an appropriate length in the z-direction (width d), therefore, the 2D density of states per unit volume is finally defined by

$$g_{2D}(E) = \frac{m_d^*}{\pi\hbar^2 d} \qquad (2\text{-}4)$$

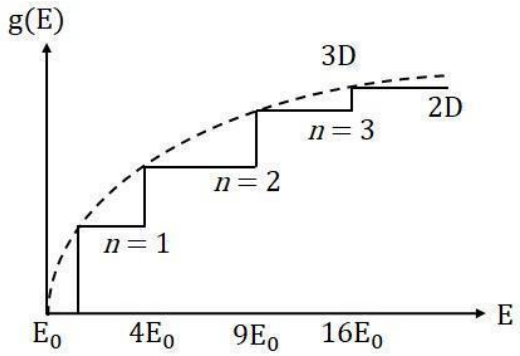

Fig. 2-5 Density of states for a quasi-quantum well in comparison with an unconfined 3D system (dash line)

In a single quantum well the center layer with the smaller bandgap semiconductor forms the QW, while the two layers sandwiching the center layer create the potential barriers as shown in Fig. 2-6. Two potential wells are actually formed in the QW structure. The well depth for electrons is the difference between the conduction band edges of the well and barrier semiconductors, while the well depth for holes is the corresponding valence-band offset.

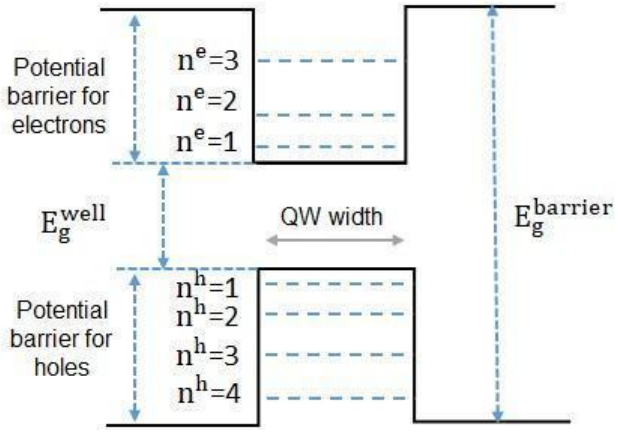

Fig. 2-6 One-dimensionally confined quantum well.

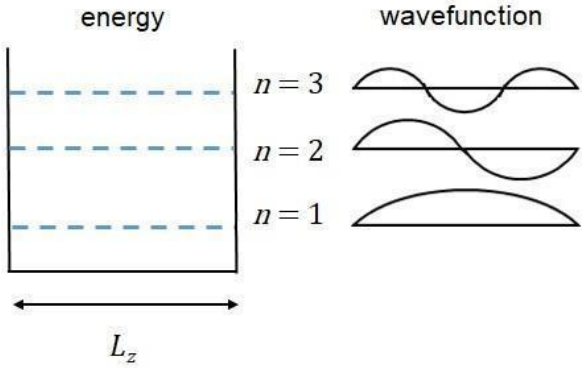

Fig. 2-7 Infinite quantum well and associated wave functions.

In contrast to bulk semiconductors, excitonic effects are very clear in quantum wells at room temperature and have a significant influence on device performance. The simplest model for absorption between the valence and conduction bands in a bulk semiconductor is to say that we can raise an electron from the valence band to a state of essentially the same momentum in the conduction band (a "vertical" transition) by absorbing a photon. The state in the conduction band has to have essentially the same momentum because the photon has essentially no momentum on the scale usually of interest in semiconductors.

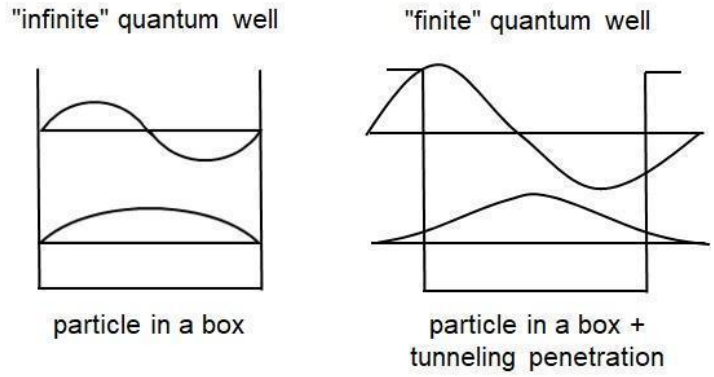

Fig. 2-8 Comparison of "infinite" quantum well and "finite" quantum well behaviour.

The optical absorption spectrum, therefore, has a form that follows directly from the density of states in energy, and in bulk semiconductors, the result is an absorption edge that rises as the square root of energy, as shown in Fig. 2-9.

In a quantum well, the electrons and holes are still free to move in the directions parallel to the layers; hence, we do not really have discrete energy states for electrons and holes in quantum wells; we have instead "sub-bands" that start at the energies calculated for the confined states. The electron in a given confined state can in addition have any amount of kinetic energy for its in-plane motion in the quantum well, and so can have any energy greater than or equal to the simple confined-state energy for that sub-band.

The density of states for motion in the plane of the quantum well layers turns out to be constant with energy, so the density of states for a given sub-band really is a "step" that starts at the appropriate confinement energy.

Optical transitions must still conserve momentum in this direction and just as for bulk semiconductors; the optical absorption must still, therefore, follow the density of states. Hence, in this simple model, the optical absorption in a quantum well is a series of steps, with one step for each quantum number, n.

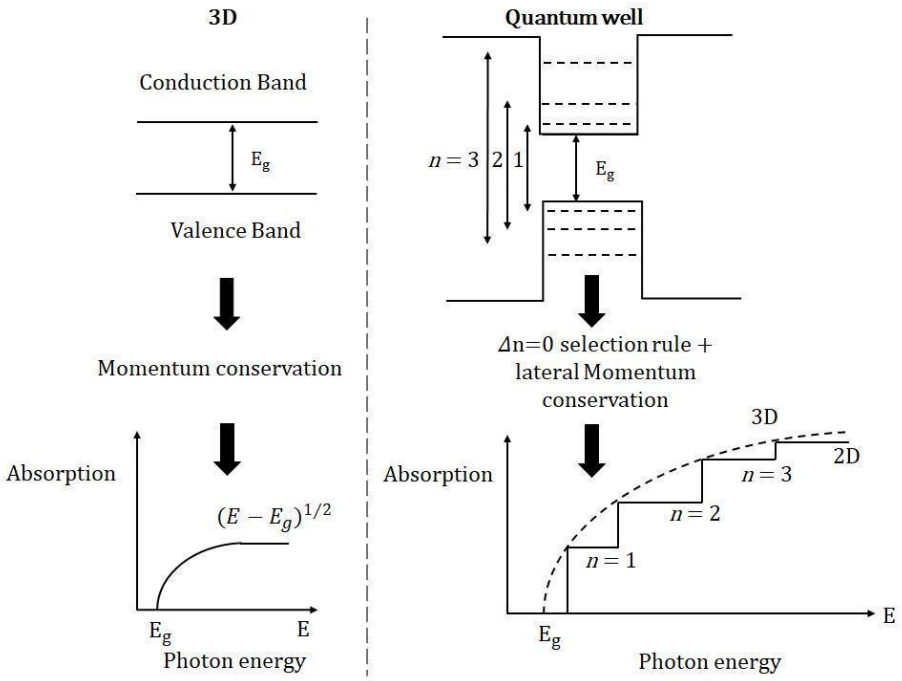

Fig. 2-9 Optical absorption in bulk semiconductors (3D) and in quantum wells.

2.3 Quantum well in optoelectronic devices

Optoelectronic devices with QW ultimately attain the best of both electronic and optical worlds. A new physical mechanism in such thin layered QW structures makes real devices with very attractive performance characteristics and impressive yields. Since semiconductor quantum wells are excellent examples of quantum mechanics in action, the reduced dimensionality has led to major advances in both the understanding of 2-D physics and the applied science of optoelectronics. The special properties of very thin layers come from the relatively simple quantum mechanical problem of confining particles in a box or well.

2.3.1 Quantum well Photodetectors

A quantum well Photodetectors is a kind of optoelectronic device incorporated with QW structure. Photodetectors for the visible and near-infrared spectral regions are generally made from bulk silicon, III-V, or II-VI.

In conventional photodetectors, as solar cells, the photocurrent and the voltage across the diode are determined by the bandgap of the semiconductors used. The power generated by a solar cell is determined by the product of both parameters. Large photocurrents are favored by narrow gap materials because semiconductors only absorb photons with energies greater than the bandgap, and narrow gap materials, therefore, absorb a larger fraction of the solar spectrum. However, the largest open-circuit voltage that can be generated in a p-n device is the built-in voltage which increases with the bandgap of the semiconductor [9].

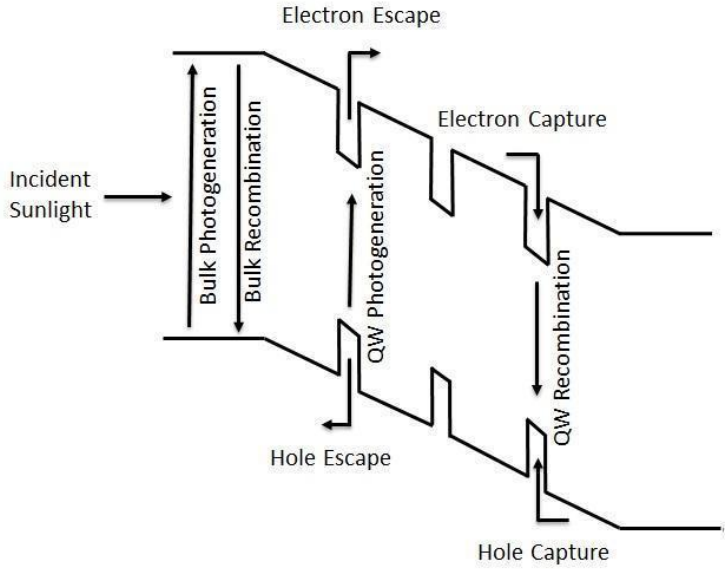

Fig. 2-10 Band diagram for the quantum well p-i-n photodetector.

Since the built-in voltage is primarily determined by the bandgap of the barrier regions, whereas the absorption edge is determined by the bandgap of the quantum wells, quantum well devices can give better performance than the bulk ones [10].

The associated band diagram together with the main carrier photogeneration and recombination paths in the barrier and QW layers is shown in Fig. 2-10.

The quantum well photodetector is composed of a p-i-n diode with quantum wells located in the intrinsic region of the device. A schematic representation of the cell is shown in Fig. 2-11.

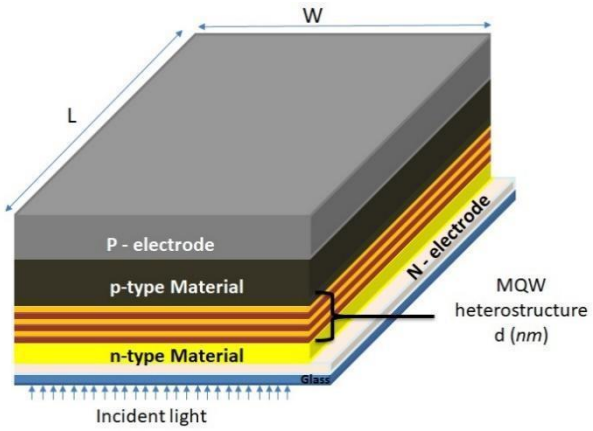

Fig. 2-11 Quantum well p-i-n layer structure

The light absorbed in the quantum wells results in the generation of electron-hole pairs in the confined well. Before these electrons and holes can contribute to the photocurrent, the carriers must escape from the quantum well through a combination of thermal and tunneling processes shown schematically in Fig. 2-10 together with the corresponding carrier capture process. The carrier escape is efficient providing that there is sufficient thermal energy and the transverse electric field is sufficiently strong [11]. In many quantum well photodetectors, as solar cells at room temperature, both the carrier capture and escape processes proceed faster than competing recombination processes, resulting in an equilibration within the conduction and valence bands between carriers in the barrier and QW layers. From a practical standpoint, this means that all photogenerated carriers in shallow quantum well can be assumed to escape and contribute towards the photocurrent [12].

2.4 Basic Absorption concepts

When the light interacts with a solid, photon absorption is presented with the intervention of different optical excitation processes.

The absorption is expressed in terms of the absorption coefficient α (hv) in eq 2-5 is defined as the ratio in which the intensity of the light (hv) decreases along its propagation path into the solid:

$$\alpha = \frac{1}{\emptyset(hv)} \frac{d[_{\emptyset(hv)}]}{dx} \qquad (2\text{-}5)$$

2.4.1 Exciton

An exciton is a quasiparticle (or elementary excitation) of the solids formed by an electron and a hole linked through the Coulomb interaction. It only occurs in semiconductors and insulators.

2.4.2 Excitonic absorption

An electron-hole pair generated by the absorption of light can remain linked by the existence of electrostatic interaction between them, the electron can orbit around the hole behaving like a hydrogen atom. The formation of excitons usually occurs in small gap materials, with a certain degree of crystallographic perfection and at low temperatures. The ionization energy of the system is represented in eq 2-6:

$$E_x = \frac{-m^*_r q^4}{2h^2 E^2 n^2} \qquad (2\text{-}6)$$

Where n is an integer greater than or equal to 1, which indicates the corresponding state of excitation and m^*_r is the reduced mass of the system, E is the dielectric constant and q the charge of the electron. The exciton can move along the glass with some kinetic energy (eq 2-7) given by:

$$K = \frac{h^2 k^2}{2(m^*_h + m^*_e)} \qquad (2\text{-}7)$$

Where K is the moment vector associated with the center of gravity of the exciton.

The formation of excitons manifests as narrow peaks at the absorption edge in direct gap semiconductors, or as soft peaks in the absorption boundary for

indirect gap semiconductors. In direct semiconductors the exciton appears when the photon's energy is:

$$E_g + E_x = hv \qquad (2\text{-}8)$$

Where E_x is the exciton binding energy.

In indirect materials, the intervention of photons is required to preserve the momentum. In the case of photon absorption, the photon must have minimum energy given by:

$$E_g - E_p - E_x = hv \qquad (2\text{-}9)$$

2.4.3 Refractive index

The refractive index “n” is a parameter of each material that indicates the behavior of light when passing through it and is defined as the ratio of the speed of light in a vacuum c and its speed in the media v. The refractive index is defined as:

$$n = \frac{c}{v} \qquad (2\text{-}10)$$

The refractive index “n” depends on wavelength, so this dependence is called dispersion. In optical materials, the refractive index is given by a complex function of the frequency of the light wave. The complex refractive index, usually denoted by n_j, with n as its real part and k_i is the imaginary part called extinction coefficient:

$$n_j = n + k_i \qquad (2\text{-}11)$$

2.4.4 Extinction coefficient (attenuation coefficient)

It indicates how easily a wave of light, sound, particle, matter, or energy can penetrate a media.

A high extinction coefficient indicates that the wave is rapidly attenuated while passing from one medium to another, while a small extinction coefficient indicates that it is medium is relatively transparent to the wave.

2.4.5 Transmission

Property of a substance to allow the passage of light, with little or no absorption of it during the process.

If the light is absorbed by the substance, the transmitted light will be a combination of the wavelength of the light that was transmitted and not absorbed. For example, a blue light filter appears blue, because it absorbs the lengths of red and green.

2.4.6 Transmission Coefficient

It is a measure of which wavelengths pass through media or an optical element. Describe the amplitude, intensity or total power of a transmitted wave in relation to an incident wave.

2.4.7 Reflection coefficient

It is a measure of reflection of wavelengths when they pass through media or an optical element. Calculate the amount of light that is reflected from a surface with a different refractive index.

2.4.8 Scattering Matrix

In quantum mechanics, the S matrix or scattering matrix is a type of formalism used to calculate the result of a scattering problem of interacting quantum particles.

2.4.9 Scattering

It is a general physical process, where some forms of radiation such as light, sound, particles, are forced to deviate from their trajectory as they pass from one medium to another.

2.5 References

[1] A.D. Yoffe (1993): Low-dimensional systems: quantum size effects and electronic properties of semiconductor microcrystallites (zero-dimensional systems) and some quasi-two-dimensional systems, Advances in Physics, 42:2, 173-262 doi: 10.1080/00018739300101484

[2] Bruker Alloy Tester, “Low Dimensional Materials”. 2019. https://www.bruker.com/es/products/surface-and-dimensional-analysis/nanomechanical-test-instruments/nanomechanical-nanotribological-applications/low-dimensional-materials.html

[3] Miller, D. A. B. et al. (1984). Band-edge electroabsorption in quantum well structures: the quantum-confined Stark effect. Physical Review Letters, 53(22), 2173–2176. doi:10.1103/physrevlett.53.2173

[4] Ye, N. & Chen, C.C. 2012. Investigation of ZnO nanorods synthesized by a solvothermal method, using Al-doped ZnO seed films. Optical Materials 34(4): 753-756.

[5] Boschloo, G., Edvinsson, T., & Hagfeldt, A. (2006). Dye-Sensitized Nanostructured ZnO Electrodes for Solar Cell Applications. Nanostructured Materials for Solar Energy Conversion, 227–254. doi:10.1016/b978-044452844-5/50009-3

[6] Orlinskii, S. B., Schmidt, J., Groenen, E. J. J., Baranov, P. G., de Mello Donegá, C., & Meijerink, A. (2005). Shallow Donors in Semiconductor Nanoparticles: Limit of the Effective Mass Approximation. Physical Review Letters, 94(9). doi:10.1103/physrevlett.94.097602

[7] Scully M.O. et al. (1999) Lasing Without Inversion Via Interference of Double-Dark Resonances in Atomic and Quantum Well Systems. In: Pötz W., Schroeder W.A. (eds) Coherent Control in Atoms, Molecules, and Semiconductors. Springer, Dordrecht doi:10.1007/978-94-011-4552-7_6

[8] Orlinskii, S. B., Schmidt, J., Baranov, P. G., Hofmann, D. M., de Mello Donegá, C., & Meijerink, A. (2004). Probing the Wave Function of Shallow Li and Na Donors in ZnO Nanoparticles. Physical Review Letters, 92(4). doi:10.1103/physrevlett.92.047603

[9] Connolly, J. P., Nelson, J., Barnham, K. W. J., Ballard, I., Roberts, C., Roberts, J. S., & Foxon, C. T. (n.d.). Simulating multiple quantum well solar cells. Conference Record of the Twenty-Eighth IEEE Photovoltaic Specialists Conference - 2000 (Cat. No.00CH37036). doi:10.1109/pvsc.2000.916130

[10] Ragay, F. W., Martí, A., Araújo, G. L., & Wolter, J. H. (1996). Experimental analysis of the efficiency of heterostructure GaAsAlGaAs solar cells. Solar Energy Materials and Solar Cells, 40(1), 5–21. doi:10.1016/0927-0248(95)00060-7

[11] Ragay, F. W., Martí, A., Araújo, G. L., & Wolter, J. H. (1996). Experimental analysis of the efficiency of heterostructure GaAs□AlGaAs solar cells. Solar Energy Materials and Solar Cells, 40(1), 5–21. doi:10.1016/0927-0248(95)00060-7 (https://doi.org/10.1016/0927-0248(95)00060-7)

[12] Toprasertpong, K., Inoue, T., Nakano, Y., & Sugiyama, M. (2018). Investigation and modeling of photocurrent collection process in multiple quantum well solar cells. Solar Energy Materials and Solar Cells, 174, 146–156. doi:10.1016/j.solmat.2017.08.036 (https://doi.org/10.1016/j.solmat.2017.08.036)

Chapter 3

Synthesis and characterization techniques

"The laws of physics…seem themselves to be the product of exceedingly ingenious design...there is for me powerful evidence that there is something going on behind it all…It seems as though somebody has fine-tuned nature's numbers to make the Universe…The impression of design is overwhelming."

Paul Davies (b. 1946), contributed to the black hole and Big Bang theories.

3.1 Thin films Deposition techniques

The ever-increasing demand from industries for versatile and multi-dynamics materials especially in the fields of optoelectronics, photonics, and magnetic devices, had taken Thin film materials and their deposition techniques, to become the integral key for the creation of thin-film new materials and continued technological advances by the processing of materials into thin films, allowing easily the integration into various types of devices. Most of these functional materials are rather applied in thin-film form due to their specific electrical, magnetic, optical properties, or wear resistance. Thin films are especially appropriate for applications in microelectronics and integrated optics [1].

The deposition techniques determine virtually all the properties of the thin film and can also be used to modify the existing properties. A single material can be used for different applications and tailored to the properties to meet the optimum requirements by using different deposition techniques [2, 3]. The properties of the material significantly differ when analyzed in the form of thin films, these properties can particularly be controlled by the thickness parameter. For a thin film, the limit of thickness is considered between tenths of nanometer and several micrometers.

Thin Film Deposition is usually divided into two broad categories – Chemical Deposition and Physical Deposition Coating Systems.

3.1.1 Physical Deposition Techniques

In physical deposition technique, mechanical or electromechanical methods are used to deposit the thin films on the substrate. Materials to be deposited on the substrate depending upon the temperature, pressure, and other physical conditions. In these physical methods, the thin films formed are directional on nature because particles will follow a straight path form the target to the substrate.

Commonly referred to as Physical Vapor Deposition (PVD) refers to a wide range of technologies where the material is released from a source and deposited

on a substrate using mechanical, electromechanical, or thermodynamic processes. The two most widely used techniques of PVD are Thermal Evaporation and Sputtering [4-6].

3.1.1.1 Thermal Evaporation

Thermal Evaporation involves heating a solid material that will be used to coat a substrate inside a high vacuum chamber until it starts to boil and evaporates producing vapour pressure. Inside the vacuum deposition chamber, even a relatively low vapour pressure is enough to raise a vapour cloud. This evaporated material now constitutes a vapour stream which the vacuum allows to travel without reacting or scattering against other atoms. It traverses the chamber and hits the substrate, sticking to it as a coating or thin film.

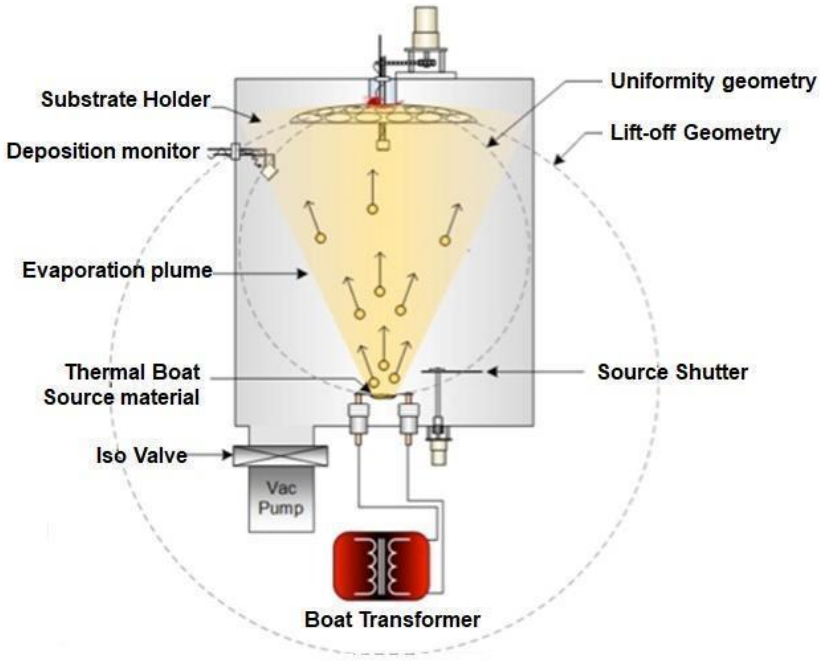

Fig. 3-1 Diagram of the thermal Evaporation process

There are two primary methods of heating the source material during Thermal Evaporation. One is known as Filament or Boat Evaporation, as it is

achieved with a simple electrical heating element or filament (Fig. 3-1). The other common heat source is an electron beam *or E-Beam Evaporation* where an electron beam is aimed at the source material to evaporate it and enter the gas phase [5, 6].

Thin Film Evaporation systems can offer the advantages of relatively high deposition rates, real-time rate and thickness control, and (with suitable physical configuration) good flow stream directional control for processes such as Lift Off to achieve directly patterned coatings.

During the thermal evaporation process, the target material vaporized from the thermal process sources gets to the substrate material with minimal interference. The process is often carried out at a high vacuum pressure (HV), and the trajectory of the movement of the target material to the substrate is a straight path trajectory termed line of sight [7]. Vapor flux is created by heating the surface of source material to a sufficiently elevated temperature in a vacuum. The flux can then condense to the surface of the substrate material to form a thin film. The vacuum environment creates a safe zone to reduce gaseous contaminants in the deposition process to an acceptable and minimal level and allows the evaporated atoms to undergo essentially collision less transport from the source onto the substrate.

The gas pressure range is usually between 0.0013 Pa to 1.3 ×10−9 Pa depending on the degree of the contamination in the deposition system, with the mean free path (MFP, the average distance between collisions occurring between species) no smaller than 5 mm. The thermal vaporization rate might be very high compared to other PVD processes [7]. Tungsten wire coils or boats are commonly used as the source of the thermal heat or by using a high energy electron beam for heating the target material to an elevated temperature.

3.1.1.1 Sputtering

Sputtering is a vital and prominent procedure among the PVD processes. It’s a non-thermal vaporization process whereby individual atom escapes from the target

surface due to atomic collision cascades by suitable high energy ion bombardment of a target material with high energy particles that are to be deposited on a substrate. The substrates to be coated are placed in a vacuum chamber containing an inert gas – usually Argon – and a negative electric charge is placed on the target material to be deposited causing the plasma in the chamber to glow.

Atoms are “Sputtered off” the target by collisions with the Argon gas atoms, carrying these particles across the vacuum chamber and are deposited as a thin film. Several different methods of plasma vapor deposition coating systems are widely used, including ion beam and ion-assisted sputtering, reactive sputtering in an Oxygen gas environment, gas flow, and magnetron sputtering [4].

Magnetron sputtering uses magnets to trap electrons over the negatively charged target material, so they are not free to bombard the substrate, preventing the object to be coated from overheating or being damaged, and allowing for a faster thin film deposition rate. They use several methods of inducing the high energy state including direct current (DC), alternating current (AC), and radiofrequency (RF) magnetron sources. Conductive materials can be deposited using a direct current (DC) power supply and insulators can be deposited by using a radio frequency (RF) power supply [5,6].

Compared to Thermal Evaporation that utilizes more conventional heating temperatures, Sputtering takes place in the plasma environment with much higher temperatures and kinetic energies allowing a much purer and more precise thin film deposition on the atomic level.

Unlike evaporation, the source is no longer created by thermal but by ion impact on the target. Also, the target to substrate distance is shorter and, in many cases, it has outperformed other PVD processes with more functionality and performance like improved adhesion and thicker film. During the sputtering process, atoms are removed from the surface of the target material by transfer of sustainable momentum from an atomic-sized energetic bombarding particle usually gaseous ion accelerated from a plasma. Sputtering deposition can be achieved in

a vacuum at low-pressure plasma under 0.67 Pa where the sputtered particles are in a straight line and can also be done at higher plasma pressure of 0.67 to 4 Pa, where energetic particles sputtered or reflected from the sputtering target are thermalized by gas-phase collision before they reach the substrate surface.

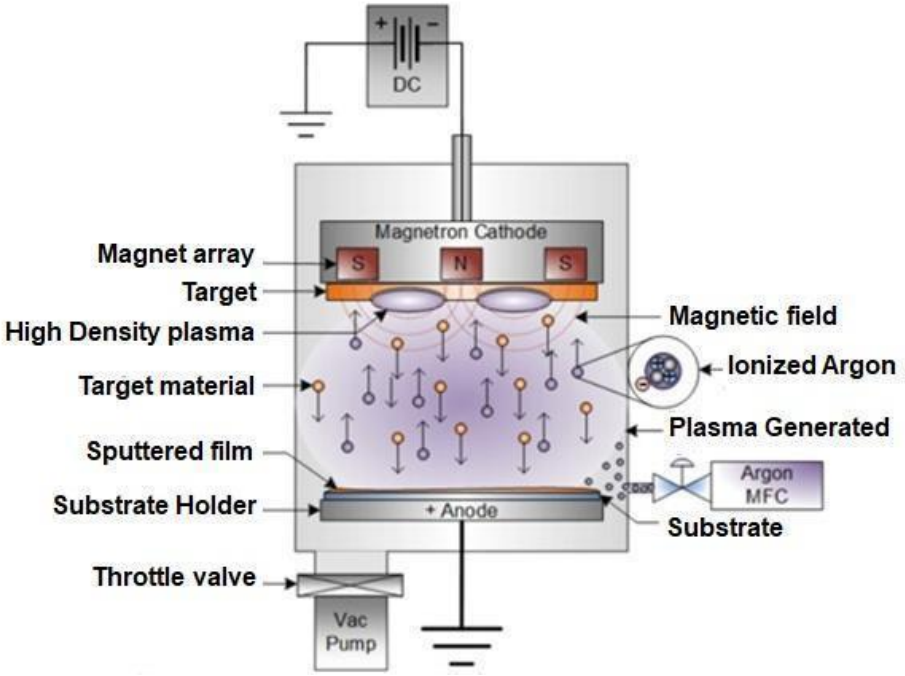

Fig. 3-2 Diagram of a sputtering process

RF sputtering offers numerous advantages like the possibility of deposition on insulating materials, ability to sustain plasma at a low pressure of 0.13 to 2 Pa, diffusion of RF plasma throughout the entire chamber, reduction of the creation of race track erosion on the surface of the target and ability to clean up the target materials after each cycle from building upcharge to reduce arcing effect [8–9]. During the sputtering process, secondary electrons are usually emitted from the target surface because of ion bombardment and magnetron sputtering makes use of the magnetic field to restrict the movement of the secondary electron to the vicinity of the target material. The configuration and strength of the magnetic field array determine the rate of the ionization efficiency current delivers to the target

material resulting in a higher deposition rate at the substrate. The increased ionization efficiency noticed during magnetron sputtering allows running of the sputtering process at a lower pressure of 100 Pa and lower voltage of −500 V compare to 10 Pa and −2 kV to 3 kV for the conventional sputtering process.

3.1.2 Wet Chemical Deposition Techniques

In chemical deposition technique, a precursor is used to chemically react with the substrate. Since the thin film material is conducted through the precursor, chemical deposition is conformally approaching the substrate without preference to a particular direction. A conformal is an uneven interface with the body and has a constant thickness on horizontal and vertical surfaces [5-6].

3.1.2.1 Chemical Bath Deposition (CBD)

Chemical bath deposition (CBD) is a simple technique that produces uniform, adherent thin films for PV and optoelectronic applications. CBD is attractive due to its low-cost, low-temperature operation. Further, it is possible to control the film thickness and composition by varying the pH of the solution, the temperature of the bath, time of deposition, and concentration of reagents.

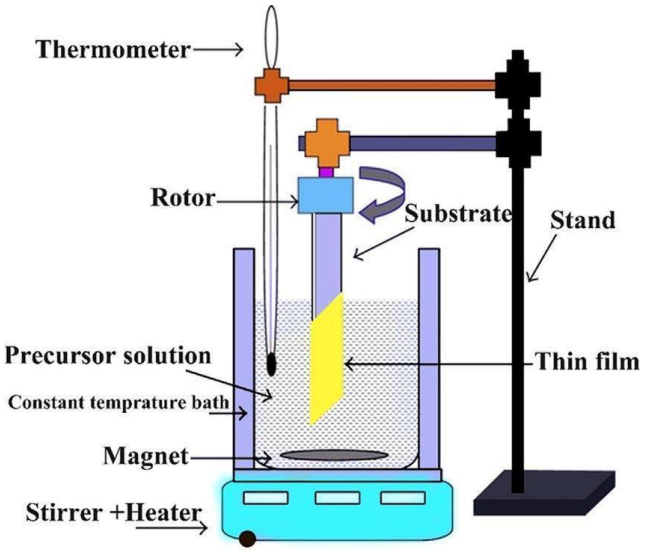

Fig. 3-3 Diagram of Chemical Bath deposition process

Deposition techniques as chemical bath deposition have proven to be efficient techniques in synthesizing good quality semiconducting chalcogenide thin films suitable for photovoltaic and optoelectronic applications [10-13].

In chemical bath deposition, a complexing agent is used to bind the metallic ions to avoid the homogeneous precipitation of the corresponding compound. The formation of complex ion is essential to control the rate of the reaction and to avoid the immediate precipitation of the compound in the solution. The metal complex hydrolyzes slowly to generate the positive ions in the solution. The solution containing the metal complex is mixed with the solution which produces the negative ion by hydrolyzes. The deposition of the compound occurs when the ionic product exceeds the solubility product of the compound to be deposited (fig. 3-3).

The main disadvantage of the chemical bath deposition is the wastage of the material due to the deposition on the walls of the container and precipitation into the solution. The preparation of the films with a definite geometric pattern on the substrate is difficult because perfect masking is not possible [14-17].

3.2 References

[1] O. Oluwatosin Abegunde , E. Titilayo Akinlabi , O. Philip Oladijo, S. Akinlabi , A. Uchenna Ude “Materials Review Overview of thin film deposition techniques “AIMS Materials Science, (2019) 6(2): 174–199. DOI: 10.3934/matersci.2019.2.174

[2] A.R. West, “Solid State Chemistry and its Applications”, 2nd Edition, Student Edition, Willey ISBN: 978-1-119-94294-8 March 2014

[3] Kasturi L. Chopra, “Thin Film Phenomena” McGraw-Hill, New York, 1969. doi:10.1126/science.169.3948.850 (https://doi.org/10.1126/science.169.3948.850)

[4] Matt Hughes, “What Is Thin Film Deposition?” 21 November 2014 http://www.semicore.com/news/81-what-is-thin-film-deposition

[5] Jilani, A., Abdel-wahab, M. S., & Hammad, A. H. (2017). Advance Deposition Techniques for Thin Film and Coating. Modern Technologies for Creating the Thin-Film Systems and Coatings. doi:10.5772/65702

[6] Henini, M. (2000). Handbook of Thin-Film Deposition Processes and Techniques. Microelectronics Journal, 31(3), 219. doi:10.1016/s0026-2692(99)00122-6 (https://doi.org/10.1016/s0026-2692(99)00122-6)

[7] DM Mattox, “Handbook of physical vapor deposition (PVD) processing”, 2nd Edition (2010), https://doi.org/10.1016/C2009-0-18800-1

[8] You, T., Niwa, O., Tomita, M., Ando, H., Suzuki, M., & Hirono, S. (2002). Characterization and electrochemical properties of highly dispersed copper oxide/hydroxide nanoparticles in graphite-like carbon films prepared by RF sputtering method. Electrochemistry Communications, 4(5), 468–471. doi:10.1016/s1388-2481(02)00340-5 (https://doi.org/10.1016/s1388-2481(02)00340-5)

[9] Torng, C. J., Sivertsen, J. M., Judy, J. H., & Chang, C. (1990). Structure and bonding studies of the C:N thin films produced by rf sputtering method. Journal of Materials Research, 5(11), 2490–2496. doi:10.1557/jmr.1990.2490 (https://doi.org/10.1557/jmr.1990.2490)

[10] Rumberg, A., Sommerhalter, C., Toplak, M., Jäger-Waldau, A., & Lux-Steiner, M. C. (2000). ZnSe thin films grown by chemical vapour deposition for application as buffer layer in CIGSS solar cells. Thin Solid Films, 361-362, 172–176. doi:10.1016/S0040-6090(99)00790-7 (https://doi.org/10.1016/S0040-6090(99)00790-7)

[11] Johnston, D. A., Carletto, M. H., Reddy, K. T. R., Forbes, I., & Miles, R. W. (2002). Chemical bath deposition of zinc sulfide based buffer layers using low toxicity materials. Thin Solid Films, 403-404, 102–106. doi:10.1016/S0040-6090(01)01536-X (https://doi.org/10.1016/S0040-6090(01)01536-X)

[12] Sankapal, B. R., Sartale, S. D., Lokhande, C. D., & Ennaoui, A. (2004). Chemical synthesis of Cd-free wide band gap materials for solar cells. Solar Energy Materials and Solar Cells, 83(4), 447–458. doi:10.1016/j.solmat.2004.01.036 (https://doi.org/10.1016/j.solmat.2004.01.036)

[13] Hankare, P. P., Chate, P. A., Chavan, P. A., & Sathe, D. J. (2008). Chemical deposition of ZnSe thin films: Photoelectrochemical applications. Journal of Alloys and Compounds, 461(1-2), 623–627. doi:10.1016/j.jallcom.2007.07.071 (https://doi.org/10.1016/j.jallcom.2007.07.071)

[14] Liu, W.-L., Chen, W.-J., Hsieh, S.-H., & Yu, J.-H. (2012). Growth Behavior of Nanocrystalline ZnS Thin Films for Solar Cell Using CBD Technique. Procedia Engineering, 36, 46–53. doi:10.1016/j.proeng.2012.03.009 (https://doi.org/10.1016/j.proeng.2012.03.009)

[15] Sinha, T., Lilhare, D., & Khare, A. (2017). Effects of Various Parameters on Structural and Optical Properties of CBD-Grown ZnS Thin Films: A Review. Journal of Electronic Materials, 47(2), 1730–1751. doi:10.1007/s11664-017-5876-z (https://doi.org/10.1007/s11664-017-5876-z)

[16] Hubert, C., Naghavi, N., Canava, B., Etcheberry, A., & Lincot, D. (2007). Thermodynamic and experimental study of chemical bath deposition of Zn(S,O,OH) buffer layers in basic aqueous ammonia solutions. Cell results with electrodeposited CuIn(S,Se)2 absorbers. Thin Solid Films, 515(15), 6032–6035. doi:10.1016/j.tsf.2006.12.139 (https://doi.org/10.1016/j.tsf.2006.12.139)

[17] Agawane, G. L., Wook Shin, S., Suryawanshi, M. P., Gurav, K. V., Moholkar, A. V., Yong Lee, J., … Hyeok Kim, J. (2013). Preparation and characterization of chemical bath deposited nanocrystalline ZnSe thin films using Na3-citrate and hydrazine hydrate: A comparative study. Materials Letters, 106, 186–189. doi:10.1016/j.matlet.2013.04.063 (https://doi.org/10.1016/j.matlet.2013.04.063)

Chapter 4

Methodology and experimental details

"The book of nature which we have to read is written by the finger of God."

Michael Faraday (d. 1867), established the existence of the magnetic field, discovered electrolysis, diamagnetism, electromagnetic induction and benzene. He invented an early version of the electric dynamo. His work laid the foundation of the modern electrical system. By showing the inter-relation between magnetism and light, he laid the groundwork for a unified field theory.

4.1 Synthesis of CdS-CdSe thin film multilayer system by CBD

4.1.1 Introduction

This experiment was made under at Coordinación para la Innovación y Aplicación de la Ciencia y la Tecnología, Av. Sierra Leona #550, Col. Lomas 2a. Sección, San Luis Potosí, S.L.P, México, under the supervision of Harumi Moreno Ph.D.

The electrical and optical property, microstructure, the surface morphology of the thin film can be modified by the deposition process. Deposition techniques as chemical bath deposition have proven to be efficient techniques in synthesizing good quality semiconducting chalcogenide thin films suitable for photovoltaic and optoelectronic applications [1-4].

Chemical bath deposition (CBD) is a simple technique that produces uniform, adherent thin films for PV and optoelectronic applications. CBD is attractive due to its low-cost, low-temperature operation. Further, it is possible to control the film thickness and composition by varying the pH of the solution, the temperature of the bath, time of deposition, and concentration of reagents.

4.1.2 Methods

4.1.2.1 CdS Solution

The CdS (hexagonal phase) Solution is prepared by mixing 25 ml of $Cd(NO_3)_2$ 0.1 M, 15 ml NH_4OH 28-30%, 2 ml of $Na_3C_6H_5O_7$ 1 M, 5ml of $(NH_2)_2CS$ 1 M with 53 ml of DI water. Sodium citrate ($Na_3C_6H_5O_7$) and ammonia hydroxide

(NH_4OH) are used as a complexing agent to bind the metallic ions to avoid the homogeneous precipitation of the corresponding compound. The formation of complex ion is essential to control the rate of the reaction and to avoid the immediate precipitation of the compound in the solution. The metal complex hydrolyzes slowly to generate the positive ions in the solution. The solution containing the metal complex is mixed with the solution which produces the negative ion by hydrolyzes. The deposition of the compound occurs when the ionic product exceeds the solubility product of the compound to be deposited.

Once the solution is mixed, the substrates are placed in the bath and heated at 80 C for 90 minutes. The growing layer is facing the baker wall.

4.1.2.2 CdSe Solution

The CdSe Solution is prepared by mixing 15 ml of $Cd(NO_3)_2$ 0.1 M, 1 ml NH_4OH 28-30%, 9 ml of $Na_3C_6H_5O_7$ 1 M, 15 ml of $Na_2Se_SO_3$ 0.2 M with 60 ml of DI water. Once the solution is mixed, the substrates with CdS (CBD and TE) are placed in the bath and heated at 80 °C for 60 minutes. The growing layer is facing the baker wall.

4.1.3 Results

Uniformed and good adherent CBD Cadmium sulfide thin film was obtained (fig. 4-1) on top of this Window layer CdSe were deposited with good appearance, adhesion, and uniformity (fig. 4-2). From left to right, thin-film with 30 and 60 minutes of CdSe deposition.

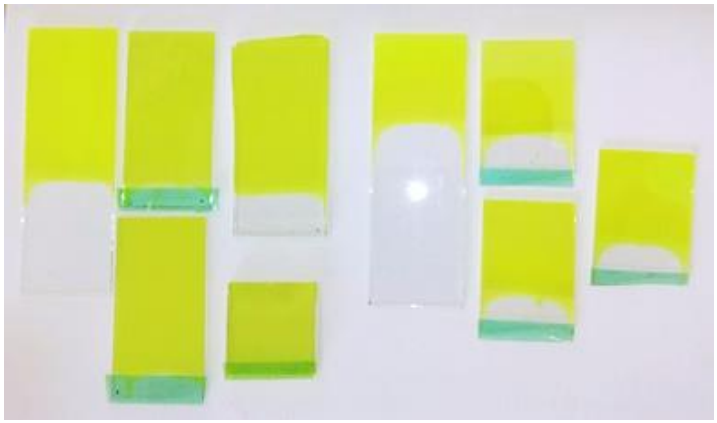

Fig. 4-1 CBD Cadmium sulfide thin film

The CdS-CdSe thin film multilayer system by CBD was made to be used in a further experiment with different thin film arrangements as shown in fig. 4-3, using CBD and TE deposition techniques.

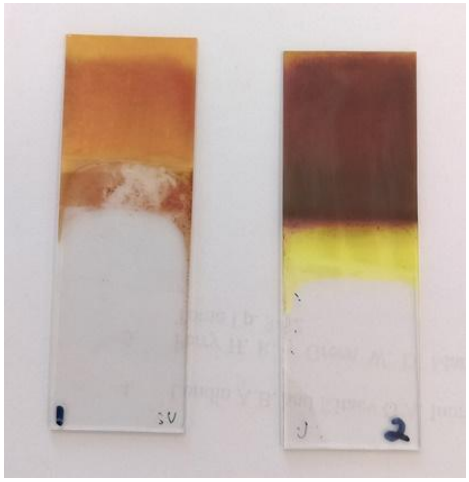

Fig. 4-2 CBD CdS-CdSe thin film

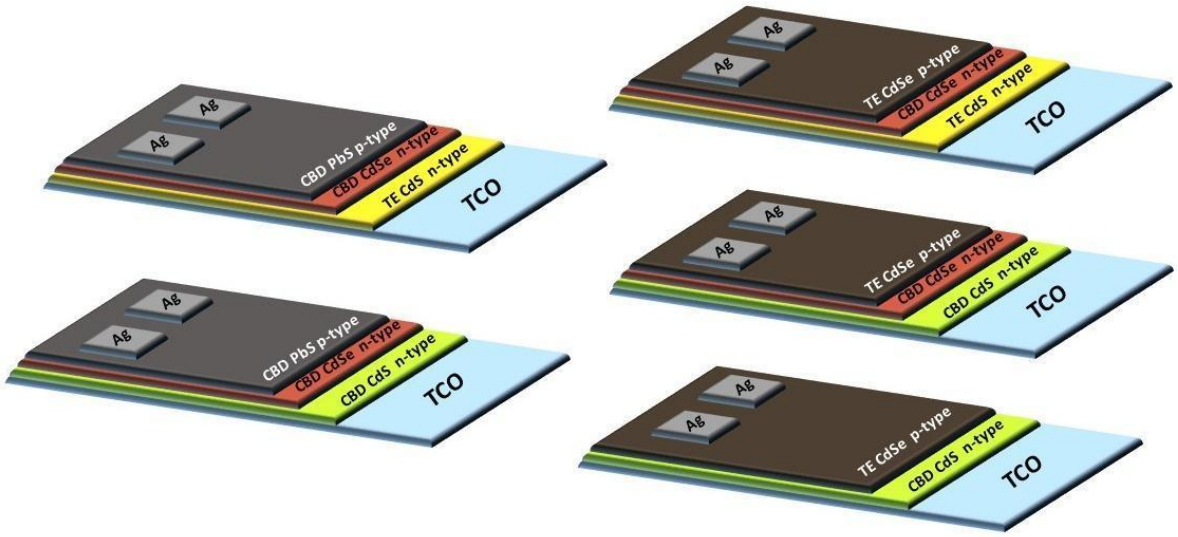

Fig. 4-3 CBD-TE PV cells arrangements

Cadmium sulfide (CdS) and Cadmium Selenide (CdSe) and Lead Sulfide (PbS) were deposited on FTO coated soda-lime glass substrates by the Chemical Bath Deposition (CBD) method and thermal evaporation technique (TE). Cadmium sulfide (CdS) is the n-type window layer with bandgap of 2.42 eV (CBD) and 2.77 eV (Thermal Evaporation). Cadmium Selenide (CdSe) is an n-type layer with a bandgap of 1.8 eV (CBD) and a p-type band gap of 1.74 eV (Thermal Evaporation), as explained in section 4.2.

4.1.4 References

[1] Rumberg, Ch. Sommerhalter, M. Toplak, A. JaÈger-Waldau, M. Ch. Lux-Steiner, Thin Solid Films 361(2000)172

[2] D.A. Johnston, M.H. Carlett, K.T.R. Reddy, I. Forbes, R.W. Miles, Thin Solid Films 403–404 (2002)102

[3] B.R. Sankapal, S.D. Sartale, C.D. Lokhande, A. Ennaoui, Sol. Energy Mater. Sol. Cells 83(2004) 447

[4] P.P. Hankare , P.A. Chate , P.A. Chavan , D.J. Sathe ,J. Alloys Compd. 461(2008)623

4.2 Electrical comparison of different CdS/CdSe/PbS heterostructures for Thin-Film Solar Cell by Chemical bath Deposition and Thermal Evaporated techniques.

4.2.1 Introduction

This Study was conducted in a collaboration with Facultad de Ingeniería Mecánica y Eléctrica, Universidad Autónoma de Nuevo León, San Nicolás de los Garza, Nuevo León, 66455, México (D. Acuña-Leal, B. Krishnan), Centro de investigación en Materiales avanzados S.C. unidad Monterrey, Autopista Monterrey-Aeropuerto. Apodaca, N.L. México (J. Alvarez-Quintana) and Coordinación para la Innovación y Aplicación de la Ciencia y la Tecnología), Av. Sierra Leona #550, Col. Lomas 2a. Sección, San Luis Potosi, S.L.P, México, (H. Moreno).

The electrical and optical property, microstructure, the surface morphology of the thin film can be modified by the deposition process. Deposition techniques as chemical bath deposition have proven to be efficient techniques in synthesizing good quality semiconducting chalcogenide thin films suitable for photovoltaic and optoelectronic applications [1-4].

Chemical bath deposition (CBD) is a simple technique that produces uniform, adherent thin films for PV and optoelectronic applications. CBD is attractive due to its low-cost, low-temperature operation. Further, it is possible to control the film thickness and composition by varying the pH of a solution, the temperature of the bath, time of deposition, and concentration of reagents [5].

The thermal evaporation is a technique which consists of heating a material at high temperature to increase its vapor pressure. The material vapor finally condenses on the substrate surface forming a thin film [6, 7]. To avoid a reaction between the vapor of the material to be deposited and the chamber atmosphere, low pressures below 10^{-4} should be used. At these low pressures, the mean free path of vapor atoms is the same order as the vacuum chamber dimensions, so these particles travel in straight lines from the evaporation source towards the substrate [6].

4.2.2 Materials and methods

4.2.2.1 Chemical Bath Deposited films

Substrates. The TCO (SnO_2):F commercial glass slides substrates were used for the elaboration of the devices. The TCO substrates were cleaned with a neutral detergent solution, rinsed in distilled water, and dried. The electric contact area on the PbS surface made Ag inks.

Chemical Bath Deposited CdS thin film. The CdS (hexagonal phase) Solution is prepared by mixing 25 ml of $Cd(NO_3)_2$ 0.1 M, 15 ml NH4OH 28-30%, 2 ml of $Na_3C_6H_5O_7$ 1 M, 5ml of $(NH_2)_2CS$ 1 M with 53 ml of DI water. Sodium citrate ($Na_3C_6H_5O_7$) and ammonia hydroxide (NH_4OH) are used as a complexing agent to bind the metallic ions to avoid the homogeneous precipitation of the corresponding compound. The formation of complex ion is essential to control the rate of the reaction and to avoid the immediate precipitation of the compound in the solution. The metal complex hydrolyzes slowly to generate the positive ions in the solution. The solution containing the metal complex is mixed with the solution which

produces the negative ion by hydrolyzes. The deposition of the compound occurs when the ionic product exceeds the solubility product of the compound to be deposited. Once the solution is mixed, the substrates are placed in the bath and heated at 80 C for 90 minutes [5].

Chemical Bath Deposited CdSe thin film. For the elaboration of CdSe thin film the solution for the chemical bath deposition was prepared using 15 ml cadmium nitrate 0.1M, 9 ml sodium citrate 1M, 2 ml ammonium hydroxide 15M, 15ml sodium selenosulfate (Na_2SeSO_3) 0.2M and 60 ml distilled water by adding in the order mentioned to a 100 ml beaker. The solution was maintained at a constant temperature of 80°C for 1 hour. The films were rinsed in hot distilled water and hot air (80°C) [8-10].

PbS powder synthesis. PbS powder was obtained following Nair procedure for chemical bath deposition by using 5 ml (1M) of lead nitrate $Pb(NO_3)_2$, 20 ml (1M) sodium hydroxide NaOH, 6 ml (1 M) thiourea (TU), 4 ml (1 M) triethanolamine (TEA) and 65 ml distilled water in a 100 ml beaker keeping the temperature at 40°C for 120 minutes [8].

CdSe Targets. The targets were prepared by compressing CdSe powder 99.99% purity from Aldrich and the synthesized PbS under 100 bar respectively.

Thermal evaporated deposited CdSe and PbS films. The films were deposited using previously prepared CdSe, PbS targets as a material source in a room temperature substrate at a vacuum higher than 10-5 Torr. PbS Layers were deposited on top of CdSe Layer. The substrate is placed on the chamber walls in front of the source, maintained at 9.5 cm from the bottom, and 4 cm aside from the

source for all the films. The deposition time was 60 minutes for the CdSe Layer, 15 minutes for the PbS.

4.2.3 Results and discussion

Three Multilayered thin films devices were developed on this work, using two different deposit techniques, Chemical Batch deposition (CBD) and Thermal evaporation (TE). The different arrangements are: i) CdS(CBD) -PbS(TE) ii) CdS(CBD) - CdSe(CBD) - PbS(TE) iii) CdS(CBD) - CdSe(CBD) - CdSe(TE)-PbS(TE).

An as a result CdS, CdSe (CBD), CdSe(TE), and PbS crystalline thin film layers were grown in a TCO coated glass with a thickness of 100 nm, 130 nm, 1 µm, and 160 nm respectively. Top metal contact area on the PbS surface made Ag inks. The devices have shown a good appearance, adhesion, and uniformity.

The devices were tested, by using a Keithley Source, first as-deposited, then after thermal treatment in vacuum conditions at 125 ºC for 10 minutes.

4.2.3.1 Analysis of PbS thin film and FTO-CdS(CBD) - CdSe(CBD) - PbS(TE)-Ag device

PbS thin film and powder XRD spectroscopy

Fig. 4-4 is showing the comparative pattern for Lead Sulfide (PbS) thin film and synthesized powder. An intense and Sharp peak is present at 30.178° correspond to (2 0 0) crystallographic plane of the PbS with a cubical crystalline structure and Fm-3m space group. Characteristics peaks at 2θ values of 26.058°, 43.203°, 51.150° corresponding to (111), (220), (311) crystallographic plane of the PbS, are present (JCPDS 01-078-1898).

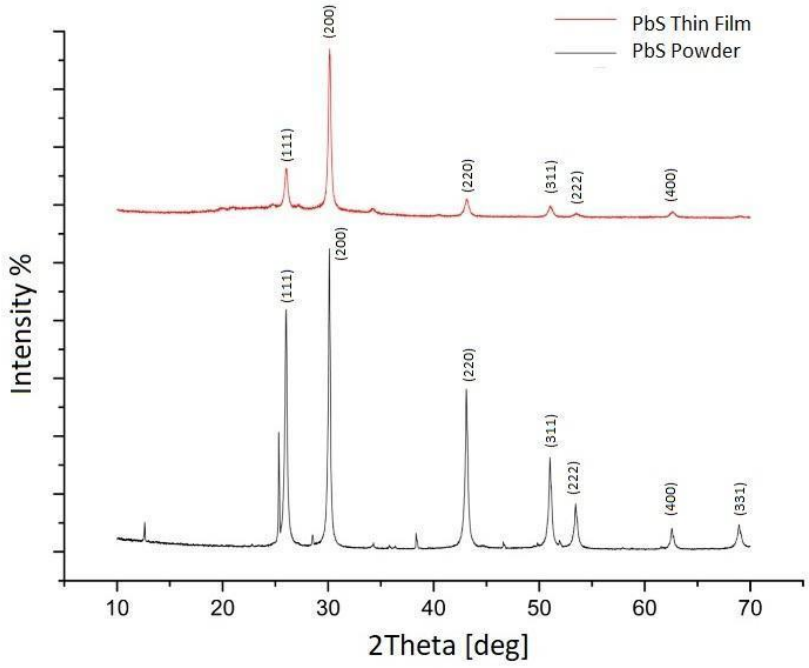

Fig. 4-3 PbS XRD Pattern

The X-ray diffraction patterns and crystallographic planes obtained from the CdS-CdSe-PbS devices shown in fig. 4-4, the presented peaks confirm the crystallinity of the materials conforming to the device. Characteristic peaks are shown, suggestive Cadmium sulfide (CdS) Greenockite, Space Group: P63mc, Crystal System: Hexagonal (JCPDS 01-079-3167). In the case of Cadmium Selenide (CdSe) peaks corresponding to Cadmoselite, Space Group: P63mc, Crystal System: Hexagonal (JCPDS 01-075-5680). For PbS peaks corresponding to cubic Crystal System, Space Group: Fm-3m (JCPDS 01-078-1898).

The average grain size of CdS, CdSe, and PbS was calculated using Scherrer Equation (1) as ~55 nm, ~22.84 nm, and ~41.7 nm respectively.

$$d = \frac{0.9\lambda}{\beta cos\theta} \qquad (4\text{-}1)$$

where β is the full width at half maximum in radians, λ is the wavelength of X-rays used and θ the angle of diffraction.

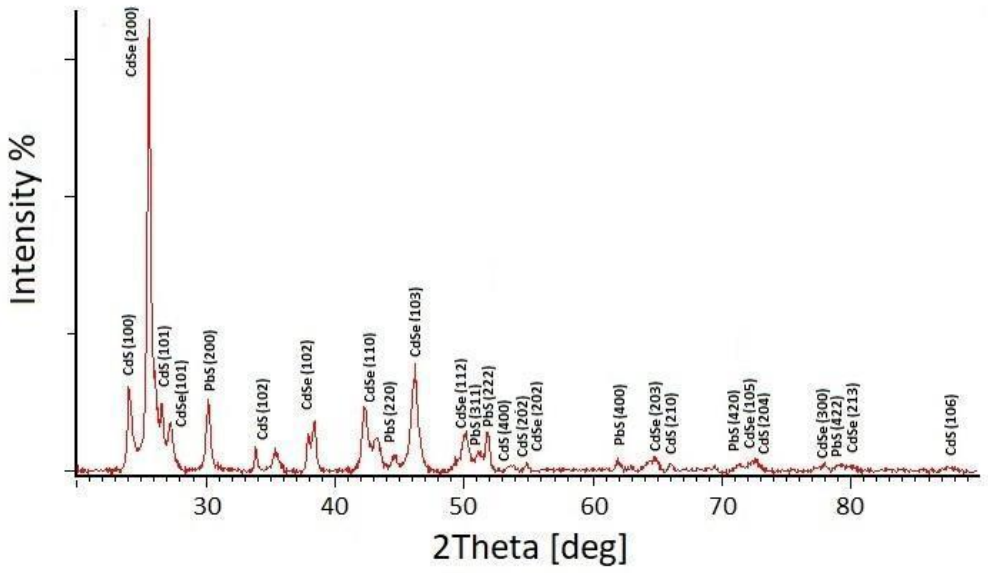

Fig. 4-4 CdS-CdSe-PbS XRD Pattern

Optical Characterization for PbS Thin film

UV-Vis measurement

The absorbance spectra of the PbS thin film (160 nm) is shown in Fig.4-5, presenting three signals that shifted to lower energy bands at ~ 350, 540, and 800 nm according to CdS characteristic peaks. Simplified Tauc method was used to calculate the absorption coefficient α [cm-1] (fig. 4-6). Bandgap was determinate as 0.79 eV. (fig. 4-7).

The refractive index n was calculated theoretically as 1.0392, determined from reflectance R using the relation $n = [(1 + \sqrt{R})/(1 - \sqrt{R})]$.

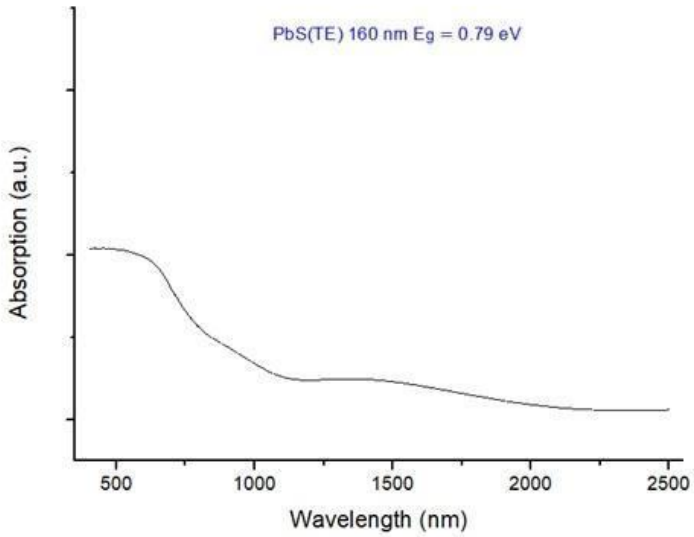

Fig. 4-5 Absorbance spectra of the PbS thin film

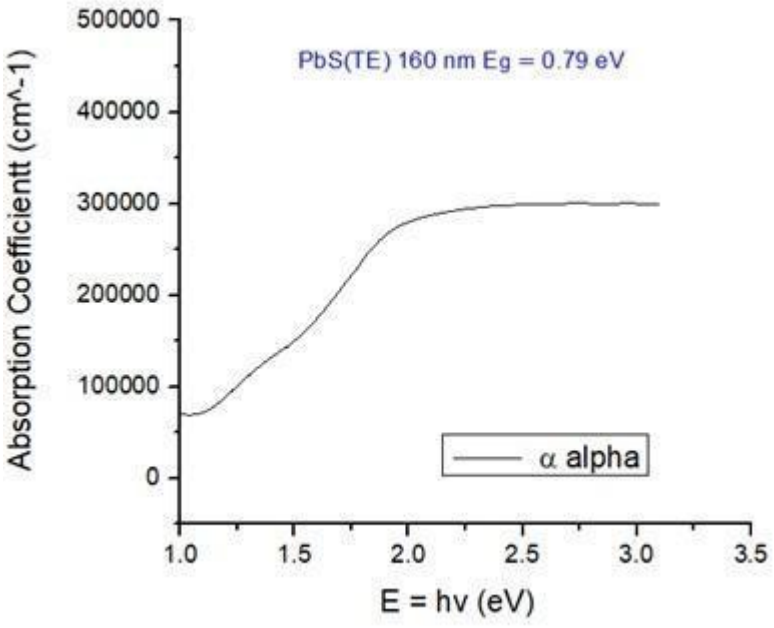

Fig. 4-6 Absorbance Coefficient of the PbS thin film

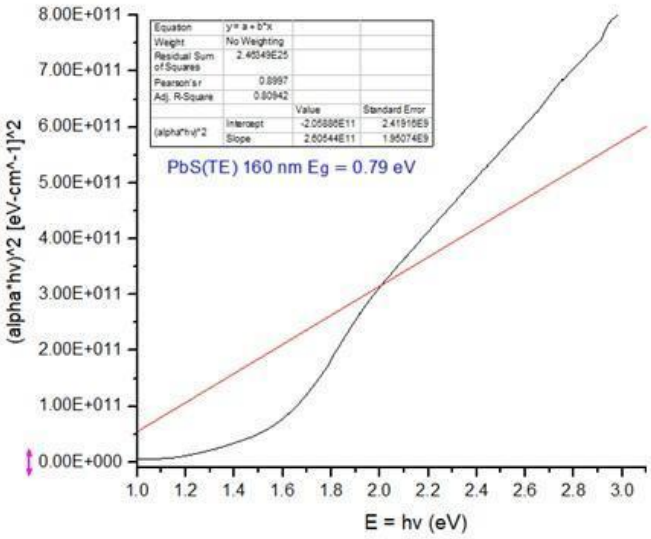

Fig. 4-7 Band Gap of the PbS thin film

Electrical Characterization

The three heterostructures were characterized by using Keithley Source meter switch system in darkness and under light with a Pin=100 mW/m^2 first as deposited, then after thermal treatment in vacuum conditions at 125 ºC during 10 minutes. Results are summarized in table 4-1, It is observed an increment in Voc from 0.111 V to 0.2165 V.

Table 4-1: Electrical characterization of the two developed devices

Heterostructure	Voc (V)	Isc (A)	Jsc (mA/cm²)	FF	Eff (%)
FTO-CdS(CBD) - PbS(TE)-Ag *	0.111	-1.52E-05	-0.0008	0.1421	0.00001
FTO-CdS(CBD) - PbS(TE)-Ag **	0.1251	-1.38E-05	-0.0008	0.0923	0.00001
FTO-CdS(CBD) - CdSe(CBD) - PbS(TE)-Ag *	0.2165	-5.55E-05	-0.003	0.0909	0.0001
FTO-CdS(CBD) - CdSe(CBD) - PbS(TE)-Ag **	0.1845	-1.36E-05	-0.0005	0.1003	0.00001
FTO-CdS(CBD) - CdSe(CBD) - CdSe(TE)-PbS(TE)-Ag *	0.05117	-7.68E-07	-0.000033	0.2575	4.37E-07
FTO-CdS(CBD) - CdSe(CBD) - CdSe(TE)-PbS(TE)-Ag **	0.1096	-2.49E-06	-0.0001	0.1073	2.00E-06

* As deposited

** With thermal treatment at 125 °C

Table 4-2: Theoretical generated excitons $m^{-3}s^{-1}$ in the proposed devices

Heterostructure	generated excitons $m^{-3}s^{-1}$
FTO-CdS(CBD) - PbS(TE)-Ag	9.86E+27
FTO-CdS(CBD) - CdSe(CBD) - PbS(TE)-Ag	7.37E+27
FTO-CdS(CBD) - CdSe(CBD) - CdSe(TE)- PbS(TE)-Ag	1.36E+27

4.2.4 Conclusion

In this work, 3 devices were fabricated with different configurations. An nm-thick P-type semiconducting film of CdSe is placed at the P-N interface of a conventional CdS/PbS PV cell architecture so as to increases the open-circuit voltage (Voc) by increasing light absorbance.

The novel approach to this PV cell architecture in the design and the deposition techniques used. Results show that in the novel proposed architecture FTO/CdS(CBD)/CdSe(CBD)/PbS(TE)/Ag not only the prevention of a decrease in Voc was achieved, but also an increase of the Voc itself from 0.111 V to 0.2165 V.

4.2.4 References

[1] Rumberg, Ch. Sommerhalter, M. Toplak, A. JaÈger-Waldau, M. Ch. Lux-Steiner, Thin Solid Films 361(2000)172

[2] D.A. Johnston, M.H. Carlett, K.T.R. Reddy, I. Forbes, R.W. Miles, Thin Solid Films 403–404 (2002)102

[3] B.R. Sankapal, S.D. Sartale, C.D. Lokhande, A. Ennaoui, Sol. Energy Mater. Sol. Cells 83(2004) 447

[4] P.P. Hankare , P.A. Chate , P.A. Chavan , D.J. Sathe ,J. Alloys Compd. 461(2008)623

[5] M. T. S. Nair, P. K. Nair, R. A. Zingaro and E. A. Meyers, Conversion of chemically deposited photosensitive CdS thin films to n – type by air annealing and ion exchange reaction, Journal Applied Physics 75 (1994) 1557 – 1564

[6] J.M. Albella (ed.), Láminas delgadas y recubrimientos: Preparación, propiedades y aplicaciones (Instituto de Ciencia de Materiales, CSIC, Madrid, 2003)

[7] K.S. Sreeharsha, Principles of Physical Vapor Deposition of Thin Films (Elsevier Science Ltd New York, 2006)

[8] P. K. Nair, M. T. S. Nair, A. Fernandez, M. Ocampo, “Prospects of chemically deposited metal chalcogenide thin films for solar control applications,” J. of Physics D: Appl. Phys. 22, 829–836 (1989).

[9] G. A. Guerrero, A. G. Rodríguez and H. Moreno-García, “Hydrazine free chemical bath deposition of WSe2 layers for photovoltaic applications”, Materials Chemistry and Physics (2018) under revision.

[10].T.S. Nair, P.K. Nair, R.A. Zingaro, E.A. Meyers, J. Appl. Phys. 75 (1994) 1557

4.3 Enhanced performance in a CdS/CdSe/$CdSe_{0.6}Te_{0.4}$ power generation device via planar structure by thermal evaporation

4.3.1 Introduction

This experiment was performed at the Centro de investigación en Materiales avanzados S.C. unidad Monterrey, Autopista Monterrey-Aeropuerto. Apodaca, N.L. México, under the supervision of J. Alvarez-Quintana Ph.D.

In the last decade, along with the different compound materials synthesis (binary, ternary, quaternary, etc.), as well as deposition techniques; the device structures have been studied to improve the performance of photonic detectors (photodetectors, solar cells, etc.). Especially, wide bandgap II-VI semiconductors are at the forefront of materials that are being studied for photonic devices where applications such as light-emitting and light-absorption are being explored [1]. Cadmium Sulfide (CdS) thin films are a matter of interest for its ideal bandgap (2.42eV), high optical absorption, and relative ease of deposition. Cadmium Selenide (CdSe) is an important compound for its direct intrinsic bandgap of 1.74eV, which makes it an interesting material for many applications. Cadmium selenium-telluride ($CdSe_xTe_{1-x}$) has received much attention due its chemical stability [2], high optical absorption [3], less toxicity [4], and the possibility of tuning the crystal structure and band-gap (from 0.9 to 1.74 eV) [5, 6] by changing the concentration of Se and Te. $CdSe_xTe_{1-x}$ thin films have been deposited by different methods such as electrodeposition [7, 8], thermal vapor deposition [9], painting and

slurry [10], sintering process [11], hot wall deposition technique [12], metal-organic chemical vapor deposition [13], among others.

Regarding device structures, Gur et al. first demonstrated an ITO/CdTe/CdSe/Cr/Au photonic detector with a power conversion efficiency (PCE) approaching 3% [14]. After, the device performance was optimized by inverting the active layers of the p-n junction, CdSe/CdTe [15-16]. Liu H et al. implemented an ITO/ZnO/CdSe/CdTe/Au device arrangement attaining a power conversion efficiency of 5.81% [17]. In addition, MacDonald et al. [18] and Zeng et al. [19] generated a layer by layer thin films sintering strategy to further optimize the quality of film with a performance of 7.1% and 6.25% in structures of ITO/CdTe/ $CdSe_xTe_{1-x}$ /ZnO/Al and ITO/ZnO/CdSe/CdSe:CdTe/CdTe/Ag respectively.

Recently, Munshi developed a similar structure with a layer of $CdSe_xTe_{1-x}$ between the CdS/CdTe or CdS/CdSe interfaces [20], as shown in Fig 4-8 (b). Unfortunately, although Jsc was improved, relative low Voc (~0.6 - 0.8 V) was obtained in the foregoing case. However, it was reported that the formed $CdSe_xTe_{1-x}$ layer was not photoactive and no photo-currents were generated by the photons absorbed by the $CdSe_xTe_{1-x}$ window layer [21]. Hence, the performance of CdTe and CdSe based photonic detectors is limited by its low Voc. In this work, in order to enhance the Voc, an alternative strategy to the former architectures is proposed. In this novel structure, a $CdSe_xTe_{1-x}$ ultrathin film is deposited away from the P-N interface but within the P-type semiconducting layer, as shown in Fig 4-8 (c). In this paper, two photonic detectors were fabricated using thermal evaporation technique. The first device, a Glass/ITO/CdS/CdSe/Ag

arrangement, was performed as a comparison device. In the second device, an ultrathin film of $CdSe_{0.6}Te_{0.4}$ was deposited some nanometers away from the depletion region of the first arrangement. I.e. buried certain distance away from CdS/CdSe interface within the CdSe layer, keeping the structure, Glass/CdS/CdSe/$CdSe_{0.6}Te_{0.4}$/CdSe/Ag.

A comprehensive analysis of the structural and electrical properties of the second arrangement confirmed the formation of a planar CdSe/ $CdSe_{0.6}Te_{0.4}$ heterostructure.

Characterization results demonstrated not only the prevention of a decrease in Voc but also an increase in Voc and Jsc that makes it competitive with previously reported photonic detectors [20].

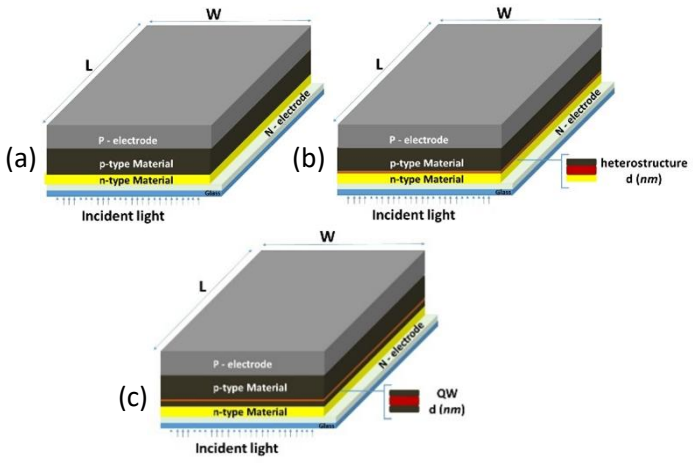

Fig. 4-8 PV device structures (a) n-p detector structure; (b) N-P MLs detector structure at the interface (c) N-P MLs detector structure inside the absorber layer.

A typical structure of a p-n PV device is shown in Fig. 48 (a). In general, the PD is composed of a highly transparent layer used as a glass substrate. A

transparent conducting oxide layer (TCO), works as the front contact (n-electrode) [22].

A high photoconductivity layer of n-type semiconductor material acts as a window layer. This layer must not be too thick to avoid short-circuiting, but of relatively high conductivity to reduce the electrical losses [23]. A layer of p-type semiconductor material acts as the principal photon absorber. This layer also acts as the back-barrier for the n-p structure [24]. Finally, a metal contact layer acts as the back contact. This layer must have a high work function to form an ohmic contact with the p-type material layer [25]. In the case of a typical multilayer detector (ML)PD, in the depletion region of the p-n junction, a section on the absorber layer is replaced by a film or multiple films of several nanometers of width to form the N-P Multilayer (N-P MLs) structure, as shown in Fig. 4-8 (b).

4.3.2 Experimental implementation

Two different designs of Photovoltaic devices were fabricated on this work, the first one is well known (Glass/ITO/CdS/CdSe/Ag) and it was used for comparison purposes, the second design (glass/CdS/CdSe/$CdSe_{0.6}Te_{0.4}$/CdSe/Ag) is the one we are presenting as a novelty on the power converting area. All the layers presented on this work were deposited by thermal evaporation method on chemically and ultrasonically cleaned 25 x 25 mm glass substrate with an ITO layer at a distance of 5 cm away from the source, no rotation or heat were applied to the substrate. The vacuum environment higher than 10-5 Torr was maintained.

The CdS, CdSe targets were prepared by using powder 99.99% purity from Sigma-Aldrich. For the CdS and CdSe targets, the powder was compressed under

100 bar. For the $CdSe_{0.6}Te_{0.4}$ target, an alloy was prepared following the stoichiometric ratio reported by L. Kumar and coauthors [11]. Both binary compounds CdS and CdSe were mixed and no sintering was applied to the target due to the used deposition method. Deposition rate were 1.94 Å/sec, 1.36 Å/sec and 0.6 Å/sec for CdS, CdSe and $CdSe_{0.6}Te_{0.4}$/CdSe respectively.

As shown in Fig. 4-8 (a), for the first arrangement, on top of an ITO coated glass a CdS-n and CdSe-p crystalline thin film layers were grown with a thickness of 350 nm and 1 µm respectively. Further, a metal contact was placed on top of the CdSe-p-type layer. In order to improve the contact between the structure layers, reduce grain boundaries, and improve electron mobility, the devices were annealed in vacuum at 100 ºC for 30 min for electrical characterization. In the second arrangement, a CdS-n layer with 350 nm followed by a CdSe layer of 123 nm of thickness was grown on the top of the ITO coated glass. Further after, to form the planar heterostructure, a thin layer of $CdSe_{0.6}Te_{0.4}$ of 18 nm followed by a CdSe layer of 0.98µm of thickness was grown. Moreover, metal contact was placed on top of the CdSe-p-type layer, as shown in Fig. 4-8 (c). No annealing treatment was performed to the ML arrangement since the number of layers deposited is higher and therefore the heat exposure is greater, working as heat treatment as well, this claim was confirmed by SEM imaging shown in Fig. 4-9.

A Scanning Empyrean X-ray Diffraction System from Malvern PANalytical was used for the identification of crystalline phases of deposited materials. Fig. 4-9 (a) shows the X-ray diffraction patterns obtained from the CdS deposited layer in

both arrangements, it is observed intense and sharp peaks suggestive Greenockite, Space Group: P63mc. The peaks at 2θ values of 25.11°, 26.82°, and 28.53°, correspond to the (1 0 0) (0 0 2) and (1 0 1) crystallographic planes with a hexagonal crystalline structure. For CdSe, Fig. 4-9 (b) shows the peaks corresponding to Cadmoselite, Space Group: P63mc. The peaks at 2θ values of 24.33°, 25.62° and 27.23°, 45.94° and 50.27° correspond to (100), (002), (101), (013) and (201) planes of hexagonal CdSe [26]. Fig. 4-9 (c), reveals for the $CdSe_{0.6}Te_{0.4}$ a sharp peak at 2θ values of 24.75° correspond to (002) and two prominent more peaks at 2θ values of 40.92° and 48.19°, correspond to (110) and (200) crystallographic planes of Cadmium Tellurium Selenide with a Hexagonal crystalline structure.

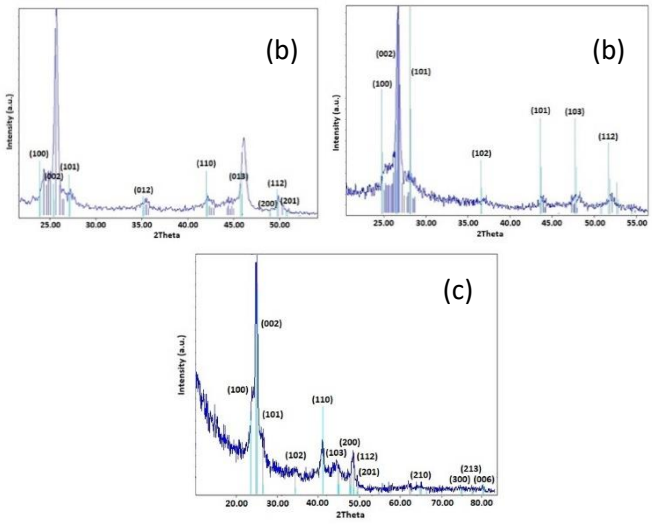

Fig. 4-9 (a) XDR pattern for the (a) CdS (b) CdSe and (c) $CdSe_{0.6}Te_{0.4}$ deposited layer

Chemical composition was verified by using Energy Dispersive Spectroscopy (EDS) and Escalab 250xi X-ray Photoelectron Spectrometer (XPS). Scanning Electron Microscope (SEM) NOVA nanoSEM200 from FEI was used for imaging analysis.

Table 4-3 Typical Values used in Calculations

Parameter	Symbol	Value	Units
CdS electric permittivity	ε_p	$8.9\varepsilon_0$	C^2/Ncm^2
CdSe electric permittivity	ε_n	$10.2\varepsilon_0$	C^2/Ncm^2
Vacuum electric permittivity	ε_0	$8.854\text{x}10^{-14}$	C^2/Ncm^2
Concentration of acceptors	N_a	$5.0\text{x}10^{15}$	cm^{-3}
Concentration of donors	N_d	$1.0\text{x}10^{15}$	cm^{-3}
Contact potential	V_0	1.6249	*Volts*

These analyses were performed to identify the morphology of the deposited CdS, CdSe, and $CdSe_{0.6}Te_{0.4}$ thin films. Fig. 4-10 shows the grain morphology and grain bounder of the CdS and CdSe deposited thin film. It is observed that the grain boundaries were reduced after the annealing process in both binary compounds [27, 28]. In addition, for both films, after the annealing process, the well energy band edges become smooth due to electric charge redistribution Fig. 4-10 (c). Hence, a heterostructure of these materials consisting of an 18 nm thin film of $CdSe_{0.6}Te_{0.4}$ (Eg=0.94 eV), was sandwiched between two layers of CdSe with a wider bandgap (1.74 eV) can confine particles which were originally free to move in one dimension, by forcing them to occupy a planar region Fig. 4-10 (c). These confined carriers can only have discrete energy values that take place when a planar heterostructure is generated.

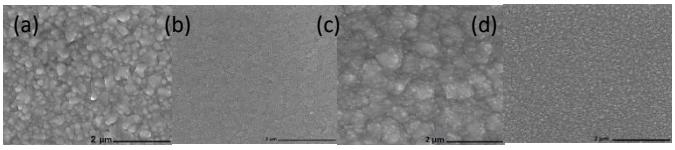

Fig. 4-10 Grain bounders of CdS and CdSe. a,b) CdS layer before and after annealing c,d) CdSe layer before and after annealing

4.3.3 Results and Discussions

In the present section, both structures, Glass/ITO/CdS/CdSe/Ag and a Glass/CdS/CdSe/$CdSe_{0.6}Te_{0.4}$/CdSe/Ag were characterized using a Keithley Source meter switch system in darkness and under light with an optical power source Pin = 100 mW/m^2.

Results are shown in the J-V transfer curves in Fig. 4-11. It is observed an increment in Voc from 0.58 V to 1.54 V, as well as an increment in Jsc from 14.68 mA/cm^2 to 21.11 mA/cm^2 between the first to the second structure. Such increments represent power conversion efficiency (PCE) in the systems of 3.1% to 11.6% respectively. For clarity, results are summarized in Table 2. Such increment in the PCE of the second structure can be attributed to the insertion of the 18 nm $CdSe_{0.6}Te_{0.4}$ thin film within the depletion region of the p-type CdS and n-type CdSe interface as explained in Fig. 4-10.

Table 4-4 Electrical Characterization of the developed devices

Device arrangement	Voc (V)	Jsc (mA/cm^2)	PCE (%)
ITO/CdS/CdSe/Ag	0.58	14.6	3.1
ITO/CdS/CdSe/ $CdSe_{0.6}Te_{0.4}$/CdSe/Ag	1.54	21.1	11.6

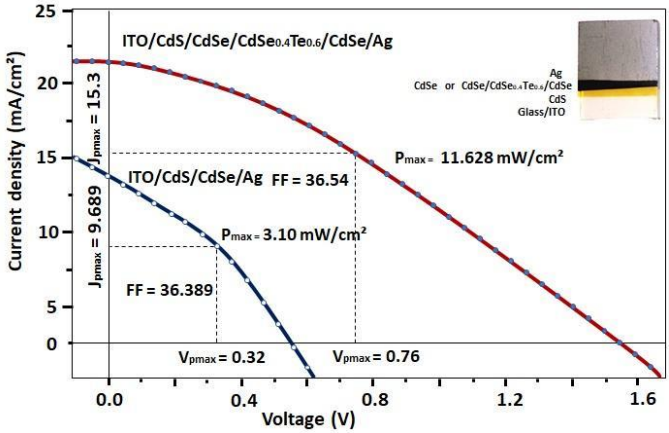

Fig. 4-11 J-V characteristics of both device arrangements; ITO/CdS/CdSe/Ag and ITO/CdS/CdSe/ CdSe0.6Te0.4/CdSe/Ag under light.

Fig. 4-12, b and c show the energy band diagrams for PV devices with structures CdS/CdSe, ITO/CdS/CdSe/Ag, and ITO/CdS/CdSe/$CdSe_{0.6}Te_{0.4}$/CdSe/Ag. The last structure corresponds to the PV decide developed in this work, where an 18 nm $CdSe_{0.6}Te_{0.4}$ thin film was buried in the P-type CdSe semiconductor layer. The average thicknesses of all the layers were obtained by a Filmetrics F20-W. The depletion regions in the n and p semiconductor, as well as the total width depletion region, were calculated using typical values given in Table (1) and Eqs. (4-2), (4-3) and (4-4) respectively.

$$x_p = \left[\frac{2\varepsilon_p V_0}{qN_dN_a\left(N_d+\frac{\varepsilon_p}{\varepsilon_n}N_a\right)}\right]^{\frac{1}{2}} N_d \qquad (4\text{-}2)$$

$$x_n = \left[\frac{2\varepsilon_n V_0}{qN_aN_d\left(N_a+\frac{\varepsilon_p}{\varepsilon_n}N_d\right)}\right]^{\frac{1}{2}} N_a \qquad (4\text{-}3)$$

$$W = x_p + x_n \qquad (4\text{-}4)$$

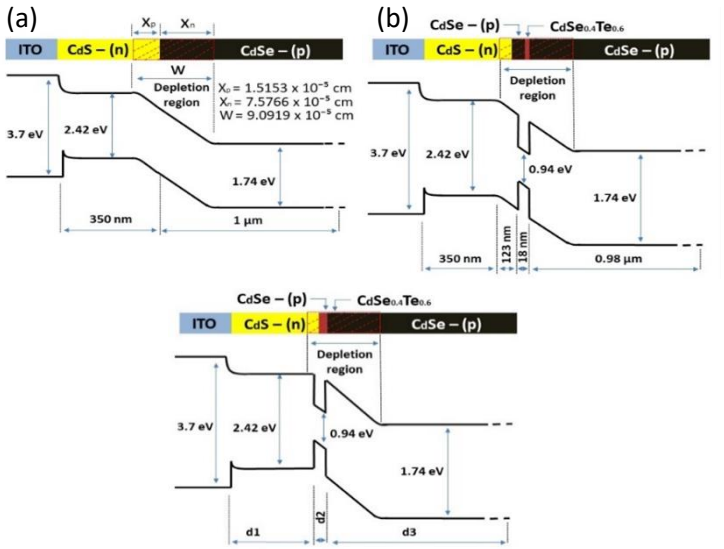

Fig. 4-12 Schematic energy diagram: a) n-p detector structure; (b) N-P MLs detector structure at the interface (c) N-P MLs detector structure inside the absorber layer.

The distribution of the total exciting optical electric field inside of the structure was estimated using the optical transfer matrix theory [29, 30]. The total optical absorption G is due to the generation of free electron-hole pairs since excitons also can dissociate and convert to a free electron-hole pair, they need to be considered as well [31]. Equation (4-5) was used to calculate the excitons generation rate; and eqn. (4-6) was used to estimate the planar structure contribution.

$$G_{(x)} = n \int_{350}^{800} \frac{\lambda}{hc} Q_{(x,\lambda)} d\lambda \qquad (4\text{-}5)$$

$$G_{jT} = G_{jT} + G_{jTQW} \qquad (4\text{-}6)$$

Where h is Planck's constant. The integration is performed from 350 nm to 800 nm, which is an appropriate photon absorbance window from the glass to the active layer of the PV device.

According to the estimations obtained using equations from 1 to 5, an ultra-thin layer between 9nm to 23 nm of $CdSe_xTe_{1-x}$ can be used in order to have an optimal electrical response. An 18 nm ultrathin film of $CdSe_xTe_{1-x}$. was obtained with a narrow bandgap (0.94 eV), confirmed by UV-VIS analysis.

4.3.4 Conclusion

In this work, an nm-thick P-type semiconducting film of $CdSe_{0.6}Te_{0.4}$ is placed far away from the P-N interface of a conventional PV cell architecture so as to increases the short - circuit current density (Jsc) and the open-circuit voltage (Voc) by increasing light absorbance.

Besides, a conventional PV detector was fabricated and characterized to compare the performance. Results show that in the novel proposed architecture not only the prevention of a decrease in Voc was achieved, but also an increase of the Voc and Jsc. The device presents a fourfold increment in power conversion efficiency regards to conventional ones. Such increment is mainly awarded to the increment in Jsc and Voc rather than significant differences in the fill factor. The present strategy shed a light in order to increase the PCE in PV cells and can provide avenues to achieve high-performance PV cells via a buried P-type layer away from the P-N interface as a light absorber

4.3.5 References

[1] R. P. Dutta and P. K. Saikia, “An electrical and Structural Studies of multilayer of CdS, CdTe and ZnSe thin films deposited by thermal evaporation method” International Journal of Innovative Research & Development 1, 73–82, 2012. DOI: 10.1007/s13204-012-0150-4

[2] Shinde, S. K., Thombare, J. V., Dubal, D. P., & Fulari, V. J.., “Electrochemical synthesis of photosensitive nano-nest like $CdSe_{0.6}Te_{0.4}$ thin films” Applied Surface Science 282, 561–565, 2013. DOI:10.1016/j.apsusc.2013.06.010

[3] S.K. Shinde, G.S. Ghodake, Dk.P. Dubal, H.D. Dhaygude, D.-Y. Kim, V.J. Fulari, “Enhanced photoelectrochemical properties of nanoflower-like hexagonal $CdSe_{0.6}Te_{0.4}$: Effect of electron beam irradiation” Journal of industrial and Engineering Chemistry 45, 92–98, 2017. DOI: 10.1016/j.jiec.2016.09.007

[4] S. K. Shinde, G. S. Ghodake, N. C. Maile, H. D. Dhaygude, Sungyeol Kim, A. D. Phule, Rahul V. Patel, D. Y. Kim, V. J. Fulari “Porous $CdSe_{0.6}Te_{0.4}$ nanoflowers-nanosphere: facile electrochemical synthesis and excellent for photoelectrochemical cell performance” Ionic 23(9), 2489–2496, 2017. DOI:10.1007/s11581-017-2077-y

[5] L. D. Budyonnaya, A. M. Pavelets, L. N. Khanat, V. E. Badan, “A study of photosensitive sintered films of CdSexTe1-x solid solutions” Thin Solid Films 138(2), 163–169, 1986. DOI:10.1016/0040-6090(86)90390-1

[6] B. Ermolovich, A. M. Pavelets and L. N. Khanat, “Mechanisms of the temperature quenching of luminescence due to deep centers in CdSexTe1-x (0 x < 1) alloys” Thin Solid Films 146(3), 233–239, 1987. DOI:10.1016/0040-6090(87)90430-5

[7] K. Adaikalam, M.R. Kim, Y.S. Chae, J.K. Rhee, S.Thanikaikarasan, T. Mahalingam, “Study on electrodeposited CdSexTe1-x semiconducting thin films” Journal of Electroanalytical Chemistry and Interfacial Electrochemistry 269(2), 399–410, 1989. DOI:10.1016/0022-0728(89)85147-2

[8] Z. Loizos, N. Spyrellis, G. Maurin, D. Pottier, “Semiconducting CdSexTe1-x thin films prepared by electrodeposition” Journal of Alloys and Compounds 505(2), 578, 1989. DOI:10.1016/j.jallcom.2010.06.136

[9] S. A. Fayek and S. M. El Sayed, “Effect of composition and forming parameter on evaporated CdSeTe films deposited at room temperature” Journal of Physics and Chemistry of Solids 63(1), 1-8, 2002. DOI: 10.1016/S0022-3697(00)00029-9

[10] G. Hodes, “A thin-film polycrystalline photoelectrochemical cell with 8% solar conversion efficiency” Nature 285, 29–30, 1980. DOI: 10.1038/285029a0

[11] L. Kumar, B. P. Singh, A. Misra, S.C.K. Misra, T.P. Sharma, “Characterization of CdSexTe1-x sintered films for photovoltaic applications” Physica B 363, 102–199 (205), 2005. DOI:10.1016/j.physb2005.03.008

[12] S. Velumani, M. Xavier and P. J. Sebastian, “Structural and optical characterization of hot wall deposited CdSe x Te 1− x films” Solar Energy Materials and Solar Cells 76(3), 359-368, 2003. DOI:10.1016/S0927-0248(02)00288-X

[13] A. Danielson, A. Munshi, D. Swanson, J. Drayton, G. Kartopu, K. Barth, S. Irvine, W. Sampath., “MOCVD deposition of group V doped CdTe sublimated and CdSeTe devices” IEEE 7th World Conference on Photovoltaic Energy Conversion (WCPEC) 978-1-5386-8529-7/18/2018. DOI:10.1109/PVSC.2018.8547722

[14] I. Gur, N. A. Fromer, M. L. Geier, A. P. Alivisatos “Air-stable all-inorganic nanocrystal solar cells processed from solution” Science 310, 462–465 2005. DOI:10.1126/science.1117908

[15] T. K. Townsend, E. E. Foos, “Fully solution processed all inorganic nanocrystal solar cells” Phys. Chem. Chem. Phys. 16, 16458–16464, 2014. DOI:10.1039/C4CP02403F

[16] W. Yoon, T. K. Townsend, M.P. Lumb, E. E. Foos, J.G. Tischler “Sintered CdTe Nanocrystal Thin Films: Determination of Optical Constants and Applications in Novel Inverted Heterojunction Solar Cells” IEEE Trans. Nanotechnol. 13, 551–556, 2014. DOI:10.1109/TNANO.2014.2310139

[17] H. Liu, Y. Tian, Y. Zhang, K. Gao, K. Lu, R. Wu, D. Qin, H. Wu, Z. Peng, L. Hou, W. Huang “Solution processed CdTe/CdSe nanocrystal solar cells with more than 5.5% efficiency by using an inverted device structure” J. Mater. Chem. C 3, 4227–4234, 2015. DOI:10.1039/C4TC02816C

[18] B. I. MacDonald, A. Martucci, S. Rubanov, S. E. Watkins, P. Mulvaney, J. J. Jasieniak,“Layer-by-Layer Assembly of Sintered CdSexTe1-x Nanocrystal Solar Cells” ACS Nano 6, 5995–6004, 2012. DOI:10.1021/nn3009189

[19] D. Qin, Y. Xie, Q. Tan, Z. Zhang, K. Lu, M. Li, Y. Zhang, W. Xu, L. Hou and H. Wu, J. Mater. Chem. C, 2016, DOI: 10.1039/C6TC01571A

[] A. H. Munshi, J. Kephart, A. Abbas, J. Raguse, J-N. Beaudry, K. Barth, J. Sites, J. Walls, W. Sampath, “Polycrystalline CdSeTe/CdTe Absorber Cells With28 mA/cm^2 Short-Circuit Current”. IEEE Journal of photovoltaics, Vol 8, no 1, 2017. DOI:10.1109/JPHOTOV.2017.2775139

[20] N. R. Paudel, Y. F. Yan, “Enhancing the photo-currents of CdTe thin-film solar cells in both short and long wavelength regions” Appl. Phys. Lett. 105, 183510, 2014. DOI:10.1063/1.4901532

[21] N. Romeo, A. Bosio, V. Canevari, A. Podestà, “Recent progress on CdS/CdTe thin film solar cells,” Sol. Energy 77(6), 795–801, 2004. DOI:10.1016/j.solener.2004.07.011

[22] H. A. Mohamed, “Dependence of efficiency of thin-film CdS/CdTe solar cell on optical and recombination losses” J. Appl. Phys. 113(1), 093105, 2013. DOI:10.1016/j.tsf.2008.11.012 9

[23] Y. Jaber, S. N. Alamri, M. S. Aida, “CdS thin films growth by ammonia free chemical bath deposition technique” Thin Solid Films 520(9), 3485–3489, 2012. DOI:10.1016/j.tsf.2011.12.061

[24] W. Xuanzhi, “High-efficiency polycrystalline CdTe thin-film solar cells,” Sol. Energy 77(6), 803–814, 2004. DOI:10.1109/PVSC.2002.1190619

[25] Albrasi, E., Thomas, P. J., & O’Brien, P. (2013). Deposition of nanostructured films of CdSe and CdS using three layered water–oil–amphiphile/salt system. J. Mater. Chem. C, 1(4), 671–676. doi:10.1039/C2TC00019A (https://doi.org/10.1039/C2TC00019A)

[26] H. Li, X. Liu, “Improved performance of CdTe solar cells with CdS treatment,” Solar Energy 115, 603-612, 2015. DOI:10.1016/j.solener.2015.02.044

[27] C-F. Chi, S-Y Liau, Y-L. Lee, "The heat annealing effect on the performance of CdS/CdSe-sensitized TiO2 photoelectrodes in photochemical hydrogen generation," Nanotechnology 21, 025202, 2010. DOI:10.1088/0957-4484/21/2/025202

[28] C. Villa-Angulo, D. Sauceda-Carvajal, J.R. Villa-Angulo, R. Villa-Angulo “Optical field dissipation in heterostructures for nanophotovoltaic devices”. Journal of Nanophotonics, 10(4), 046001, 2016. DOI:10.1117/1.jnp.10.046001

[29] J.C. Quiroz-Sánchez, V. Cabrera-Arenas, C. Villa-Angulo “Optimization of organic photovoltaic device performance via exciton generation profile adjustment”. Journal of Photonics for Energy, 5(1), 052098, 2015. DOI:10.1117/1.jpe.5.052098

[30] M. Burgelman, B. Minnaert, “Including excitons in semiconductor solar cell modelling”. Thin Solid Films, 511-512, 214–218, 2006. DOI:10.1016/j.tsf.2005.12.054

4.4 Electrical comparison of different CdS/CdTe/PbS heterostructures for Thin-Film Solar Cell by RF Sputtering Deposition.

4.4.1 Introduction

This Study was conducted in collaboration with the Department of Electrical and Computer Engineering, The University of Texas at San Antonio. UTSA Circle, San Antonio, TX 78249, under the supervision of Ethan C. Ahn P hD. and the Facultad de Ingeniería Mecánica y Eléctrica, Universidad Autónoma de Nuevo León, San Nicolás de los Garza, Nuevo León, 66455, México, under the supervision of Francisco Solis Ph.D.

In the last decade, the thin-film technology, along with the different compound materials synthesis (binary, ternary, quaternary, etc.), as well as deposition techniques; the device structures have been studied to improve the performance of photonic detectors (photodetectors, solar cells, etc.). Especially, wide bandgap II-VI semiconductors are at the forefront of materials that are being studied for photonic devices where applications such as light-emitting and light-absorption are being explored [1].

Cadmium Sulfide (CdS) thin films are a matter of interest for its ideal bandgap (2.42eV), high optical absorption, and relative ease of deposition. Cadmium Telluride (CdTe) is an important compound for its direct intrinsic bandgap of 1.48eV. Lead sulfide (PbS) is a prominent direct narrow-gap semiconductor with a room temperature band gap of 0.41 eV. Because of a relatively large Bohr exciton radius of 18nm [2], exhibit the strong confinement

regimen in a low dimensional structure, its bandgap can be engineered between 0.4 and ~1.6 eV, turning the PbS a promising candidate for a bottom absorber layer in tandem photovoltaic. These properties make the quantum confinement effects more notable in PbS compared to other lead chalcogenides, even for relatively larger particle sizes [3–4]. Polycrystalline thin-film tandem solar cells that leverage commercial II-VI semiconductor technologies, as the top cell could overcome the practical conversion-efficiency limits of single-junction solar cells.

CdTe thin-film solar cells hold the greatest market share in photovoltaic next to Si and have exceeded polycrystalline Si in performance and costs [5]. While generally underexplored, combining CdTe in a tandem configuration could retain the low-cost structure of CdTe devices and improve the amount of power generated [6].

Thin films have been deposited by different methods such as electrodeposition [7, 8], thermal vapor deposition [9], painting and slurry [10], sintering process [11], hot wall deposition technique [12], metal-organic chemical vapor deposition [13], among others. In the current study, a tandem solar cell is presented, using different configurations of sputtered CdS, CdTe, and PbS.

Regarding device structures, different configurations have been widely studied such as CdS/PbS, CdS/CdTe or CdTe/PbS. Hence, the performance of CdTe based photonic detectors is limited by its low Voc, in this work, an alternative strategy to the former configurations is proposed. In this novel structure, CdS/CdTe/PbS films are deposited, as shown in Fig 1(b). In this study, two solar cell arrangements were fabricated using RF sputtering on top of 3 different

transparent conductive oxides (ITO, FTO, and ZnO). The arrangements are shown in table 4-5.

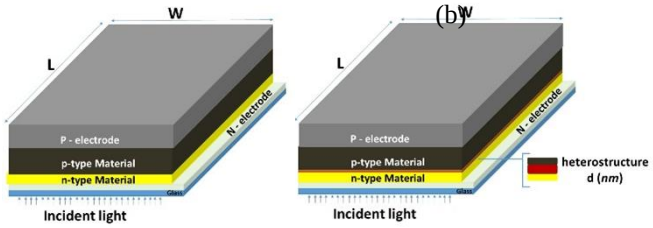

Fig. 4-13 PV decide structures. (a) n-p standard solar cell structure; (b) n-p tandem solar cell structure.

Characterization results demonstrated a variation in the Voc. The highest Voc achieved was 0.42 V with a CdTe thickness of ~1000 nm, which is also the CdTe thickness where the tandem cell was found to exhibit the best overall performance [4].

A typical structure of a p-n PV device is shown in Fig. 4-13 (a). In general, the solar cell is composed of a highly transparent layer used as a glass substrate. A transparent conducting oxide layer (TCO), works as the front contact (n-electrode) [14]. A high photoconductivity layer of n-type semiconductor material acts as a window layer. This layer must not be too thick to avoid short-circuiting, but of relatively high conductivity to reduce the electrical losses [15]. A layer of p-type semiconductor material acts as the principal photon absorber. This layer also acts as the back-barrier for the n-p structure [16]. Finally, a metal contact layer acts as the back contact. This layer must have a high work function to form an ohmic contact with the p-type material layer [17]. In the case of a typical tandem solar cell, in the depletion region of the p-n junction, a section on the absorber layer is

replaced by a film or multiple films to form the N-P Multilayer structure, as shown in Fig. 4-13 (b).

4.4.2 Thin Film Deposition - Device fabrication

Commercial glass substrates with a TCO (ITO and FTO) layers and in lab prepared ZnO layer was used as a bottom electrical contact. The zinc oxide layer was deposited on a commercial glass in a Beneq TFS 200 ALD reactor at 170 °C with 1000 cycles with a growth per cycle of 2 Å, precursor pulse: 100 ms DEZ (Diethylzinc), precursor purge: 2 s N_2, oxidant agent pulse: 150 ms H2O and Oxidant agent purge: 750 ms N_2.

Cadmium sulfide (CdS) was used as a window layer and Cadmium Telluride (CdTe) and PbS were used as the absorber material.

4.4.2.1 CdTe thin film

Phase II J from AJA International Inc. sputtering machine was used. The proposed conditions include 60 sccm of Ar, nevertheless, the equipment used does not allow more than 20 sccm. Several deposits were made to establish the operating conditions, to measure the thickness, and to study the crystalline structure and chemical composition. Table 4-5 is showing the different conditions used in this work. Different deposition rates of 60 W, 80 W, and 100 W corresponding to 0.57 Å/sec, 0.80 Å/sec, and 1.26 Å/sec, respectively, were provided by the equipment sensor. Based on these rates, power of 100 W was selected, and the deposition time was tuned in order to have the desired thicknesses.

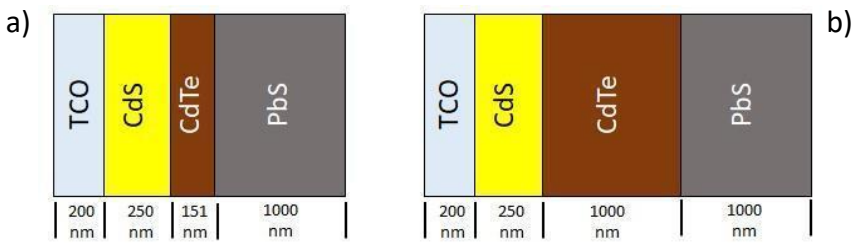

Fig. 4-14 PV device structures (a) n-p standard solar cell structure; (b) n-p tandem solar cell structure

Table 4-5. RF Sputtering operating conditions

#	Power (W)	Coat time (sec)	#	Power (W)	Coat time (sec)
1	45	30	16	80	300
2	50	30	17	100	300
3	45	30	18	60	600
4	45	10	19	80	600
5	45	20	20	100	600
6	60	60	21	100	2 x 600
7	60	60	22	100	2 x 600
8	70	60	23	100	2 x 600
9	80	60	24	100	2 x 600
10	90	60	25	100	60
11	100	60	26	100	60
12	60	180	27	100	60
13	80	180	28	100	13 x 600
14	100	180	29	100	13 x 600
15	60	300			

4.4.2.2 CdS and PbS

A Huntington sputtering machine was used. The CdS deposition was driven under a pressure of 60 sccm of Argon with a Power source settled at 100 W for 3 minutes, the thickness of the CdS film was ~250 nm. The PbS deposition conditions were: Working Power of 150 W for 5 minutes with an Argon pressure of 80 sccm, with a thickness of ~1000 nm.

4.4.3 Results and discussions

In the present section, all they were characterized using a Keithley Source meter switch system in darkness and under a light with an optical power source Pin = 100 mW/m^2. Table 4-6 is showing the different solar cell configuration as their electrical characterization results are summarized. 2 general arrangements were studied TCO/CdS 250 nm/CdTe 1000 nm/ PbS 1000 nm and TCO/ CdS 250 nm/CdTe 151 nm/ PbS 1000nm.

Table 4-6. Electrical Characterization of the developed devices

ITO	FTO	ZnO	CdS nm	CdTe nm	PbS nm	Vmax V	Voc V	Jsc mA/cm²	FF	eff %
x	-	-	250	1000	1000	-	-	-	-	-
-	x	-	250	1000	1000	**0.052**	**0.10**	**1.15**	**25.50**	**0.004**
-	-	x	250	1000	1000	0.20	0.42	41.76	27.02	4.740
						0.20	0.4	40.89	26.94	4.407
						0.18	0.34	33.79	26.15	3.004
						0.18	0.34	32.83	26.68	2.978
					average	**0.19**	**0.38**	**37.32**	**26.70**	**3.782**
x	-	-	250	151	1000	0.04	0.08	6.54	18.85	0.099
						0.08	0.18	17.64	23.96	0.761
					average	**0.06**	**0.13**	**12.09**	**21.41**	**0.430**
	x	-	250	151	1000	-	-	-	-	-
-	-	x	250	151	1000	0.08	0.16	15.73	24.82	0.625
						0.08	0.14	13.80	25.10	0.485
						0.08	0.16	15.29	23.74	0.581
					average	**0.08**	**0.15**	**14.94**	**24.55**	**0.563**

In the first arrangement, devices with the configuration of ITO/CdS 250 nm/CdTe 1000 nm/ PbS 1000 nm/Ag did not generate any power at all, instead,

those with FTO and ZnO did have a response, as shown in Fig. 4-15, where it is observed an average increment in Voc from 0.1 (FTO) V to 0.38 V (ZnO), as well as an increment in Jsc from 1.15 mA/cm2 to 37.32 mA/cm2 between the first to the second structure. Such increments represent power conversion efficiency (PCE) in the systems of 0.0468% to 4.98% respectively.

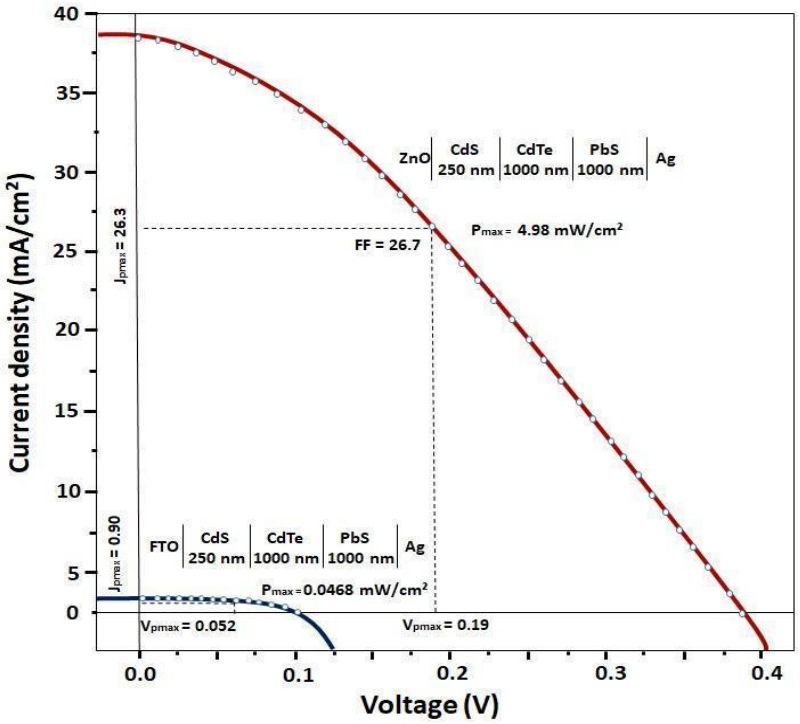

Fig. 4-15 J-V characteristics of TCO/CdS 250 nm/CdTe 1000 nm/ PbS 1000 nm/Ag under light.

In the second argument TCO/ CdS 250 nm/CdTe 151 nm/ PbS 1000nm, was not observed any electrical response with the FTO layer, instead, devices with ITO and ZnO shown a generated Voc. Fig. 4-16, is showing an average increment in Voc from 0.06 V (ITO) to 0.08 V (ZnO), as well as an increment in Jsc from 4.45 mA/cm2 to 8.75 mA/cm2 between the first to the second structure. Such

increments represent power conversion efficiency (PCE) in the systems of 0.447% to 0.7% respectively.

Such increment in the PCE of both arrangements can be attributed to the ZnO layer. The highest Voc achieved was 0.42 V with a CdTe thickness of ~1000 nm, which is also the CdTe thickness where the tandem cell was found to exhibit the best overall performance. For clarity, results are summarized in Table 4-6

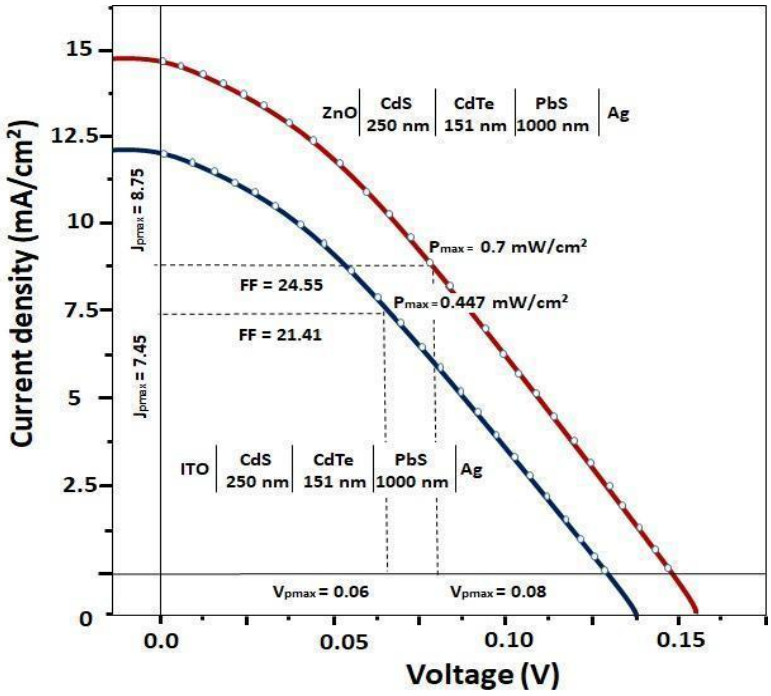

Fig. 4-16 J-V characteristics of TCO/CdS 250 nm/CdTe 151 nm/ PbS 1000 nm/Ag under light.

4.4.4 References

[1] R. P. Dutta and P. K. Saikia, “An electrical and Structural Studies of multilayer of CdS, CdTe and ZnSe thin films deposited by thermal evaporation method” International Journal of Innovative Research & Development 1, 73–82, 2012. DOI: 10.1007/s13204-012-0150-4

[2] Wang, S. F., Gu, F., & Lü, M. K. (2006). Sonochemical Synthesis of Hollow PbS Nanospheres. Langmuir, 22(1), 398–401. doi:10.1021/la0518647 (https://doi.org/10.1021/la0518647)]

[3] Thangavel, S., Ganesan, S., Chandramohan, S., Sudhagar, P., Kang, Y. S., & Hong, C.-H. (2010). Band gap engineering in PbS nanostructured thin films from near-infrared down to visible range by in situ Cd-doping. Journal of Alloys and Compounds, 495(1), 234–237. doi:10.1016/j.jallcom.2010.01.135 (https://doi.org/10.1016/j.jallcom.2010.01.135)

[4] Crisp, R. W., Pach, G. F., Kurley, J. M., France, R. M., Reese, M. O., Nanayakkara, S. U., … Luther, J. M. (2017). Tandem Solar Cells from Solution-Processed CdTe and PbS Quantum Dots Using a ZnTe–ZnO Tunnel Junction. Nano Letters, 17(2), 1020–1027. doi:10.1021/acs.nanolett.6b04423 (https://doi.org/10.1021/acs.nanolett.6b04423)]

[5] Coutts, T. J., Ward, J. S., Young, D. L., Emery, K. A., Gessert, T. A., & Noufi, R. (2003). Critical issues in the design of polycrystalline, thin-film tandem solar cells. Progress in Photovoltaics: Research and Applications, 11(6), 359–375. doi:10.1002/pip.491 (https://doi.org/10.1002/pip.491))]

[6] Mailoa, J. P., Lee, M., Peters, I. M., Buonassisi, T., Panchula, A., & Weiss, D. N. (2016). Energy-yield prediction for II–VI-based thin-film tandem solar cells. Energy & Environmental Science, 9(8), 2644–2653. doi:10.1039/c6ee01778a (https://doi.org/10.1039/c6ee01778a)K. Adaikalam, M.R. Kim, [7] Y.S. Chae, J.K. Rhee, S.Thanikaikarasan, T. Mahalingam, “Study on electrodeposited CdSexTe1-x semiconducting thin films” Journal of Electroanalytical Chemistry and Interfacial Electrochemistry 269(2), 399–410, 1989. DOI:10.1016/0022-0728(89)85147-2

[8] Z. Loizos, N. Spyrellis, G. Maurin, D. Pottier, “Semiconducting CdSexTe1-x thin films prepared by electrodeposition” Journal of Alloys and Compounds 505(2), 578, 1989. DOI:10.1016/j.jallcom.2010.06.136

[9] S. A. Fayek and S. M. El Sayed, “Effect of composition and forming parameter on evaporated CdSeTe films deposited at room temperature” Journal of Physics and Chemistry of Solids 63(1), 1-8, 2002. DOI: 10.1016/S0022-3697(00)00029-9

[10] G. Hodes, “A thin-film polycrystalline photoelectrochemical cell with 8% solar conversion efficiency” Nauture 285, 29–30, 1980. DOI: 10.1038/285029a0

[11] L. Kumar, B. P. Singh, A. Misra, S.C.K. Misra, T.P. Sharma, “Characterization of CdSexTe1-x sintered films for photovoltaic applications” Physica B 363, 102–199 (205), 2005. DOI:10.1016/j.physb2005.03.008

[12] S. Velumani, M. Xavier and P. J. Sebastian, “Structural and optical characterization of hot wall deposited CdSe x Te 1− x films” Solar Energy Materials and Solar Cells 76(3), 359-368, 2003. DOI:10.1016/S0927-0248(02)00288-X

[13] A. Danielson, A. Munshi, D. Swanson, J. Drayton, G. Kartopu, K. Barth, S. Irvine, W. Sampath., “MOCVD deposition of group V doped CdTe sublimated and CdSeTe devices” IEEE 7th World Conference on Photovoltaic Energy Conversion (WCPEC) 978-1-5386-8529-7/18/2018. DOI:10.1109/PVSC.2018.8547722.

[14] N. Romeo, A. Bosio, V. Canevari, A. Podestà, “Recent progress on CdS/CdTe thin film solar cells,” Sol. Energy 77(6), 795–801, 2004. DOI:10.1016/j.solener.2004.07.011

[15] H. A. Mohamed, “Dependence of efficiency of thin-film CdS/CdTe solar cell on optical and recombination losses” J. Appl. Phys. 113(1), 093105, 2013. DOI:10.1016/j.tsf.2008.11.012 9

[16] Y. Jaber, S. N. Alamri, M. S. Aida, “CdS thin films growth by ammonia free chemical bath deposition technique” Thin Solid Films 520(9), 3485–3489, 2012. DOI:10.1016/j.tsf.2011.12.061

[17] W. Xuanzhi, “High-efficiency polycrystalline CdTe thin-film solar cells,” Sol. Energy 77(6), 803–814, 2004. DOI:10.1109/PVSC.2002.1190619.

[18] H. Liu, Y. Tian, Y. Zhang, K. Gao, K. Lu, R. Wu, D. Qin, H. Wu, Z. Peng, L. Hou, W. Huang “Solution processed CdTe/CdSe nanocrystal solar cells with more than 5.5% efficiency by using an inverted device structure” J. Mater. Chem. C 3, 4227–4234, 2015. DOI:10.1039/C4TC02816C

Chapter 5

Gummel Algorithm: on the modeling of the quantum and electrical behavior of low dimension heterostructures

"I do not feel obliged to believe that the same God who has endowed us with senses, reason, and intellect has intended us to forego their use and by some other means to give us knowledge which we can attain by them. He would not require us to deny sense and reason in physical matters which are set before our eyes and minds by direct experience or necessary demonstrations."

Galileo Galilei (1564 - 1642)

5.1. Algorithm Development

5.1.1. Design requirements - Operational characteristics of the photovoltaic device

The spectrum and incident flow of photons to be used is that established by the global AM1.5 standard.

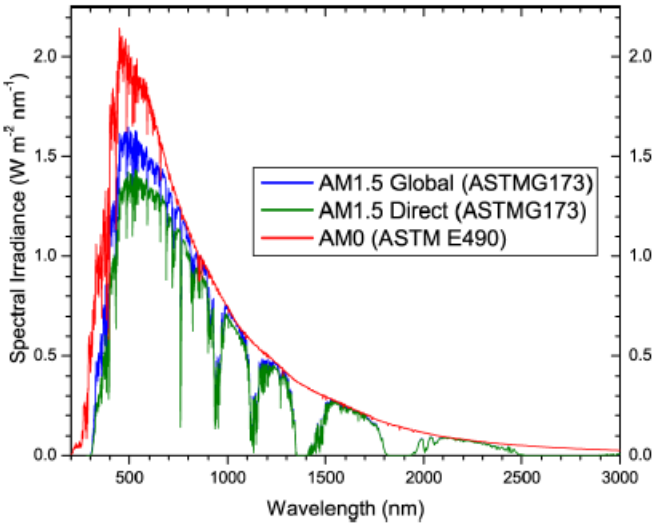

Fig. 5-1 Extraterrestrial Solar Irradiance Spectra

The average incident power set in the AM1.5 standard is 1000 W / m², 100 mW / cm².

The required absorption spectrum is 350 nm to 800 nm.

Maximum power resistance (MPR) and Voltage required (Vt).

Maximum power resistance (MPR) = 100 Ω.

Required voltage Vmp = 5 volts.

$$R_{mp} = \frac{V_{mp}}{I_{mp}} = \frac{5\ V}{I_{mp}} = 100\Omega$$

$$I_{mp} = \frac{5\ V}{100\Omega} = 0.05A = 50\ mA$$

5.1.1.1 Calculations and procedure

5.1.1.1.1 Materials selection

It is desired to build a detector in the visible spectrum, so according to the range chart for detectors due to its optical and quantum properties, the CdS is selected (*Fig. 5-2*).

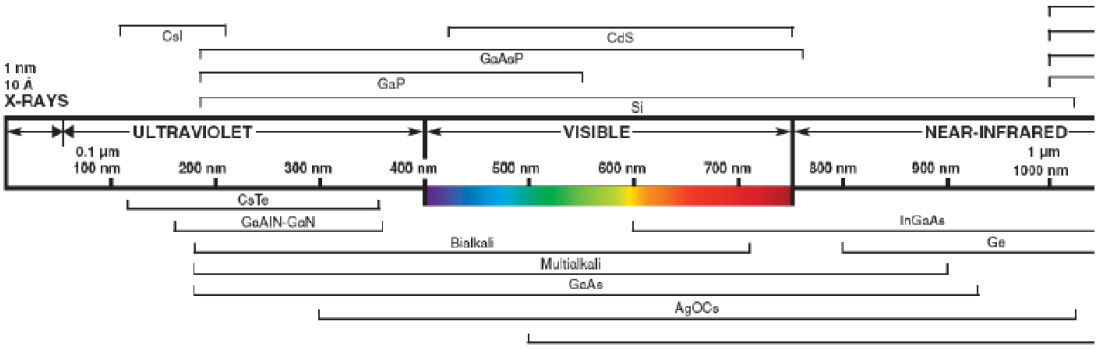

Fig. 5-2 Photonic application spectrum charts for detectors range

Due to the chemical nature of the species, there are 2 binary materials that can be used to form the heterojunction, the CdSe, and the CdTe. CdSe is selected because it has the network constant closest to the CdS, see Fig. 5-3.

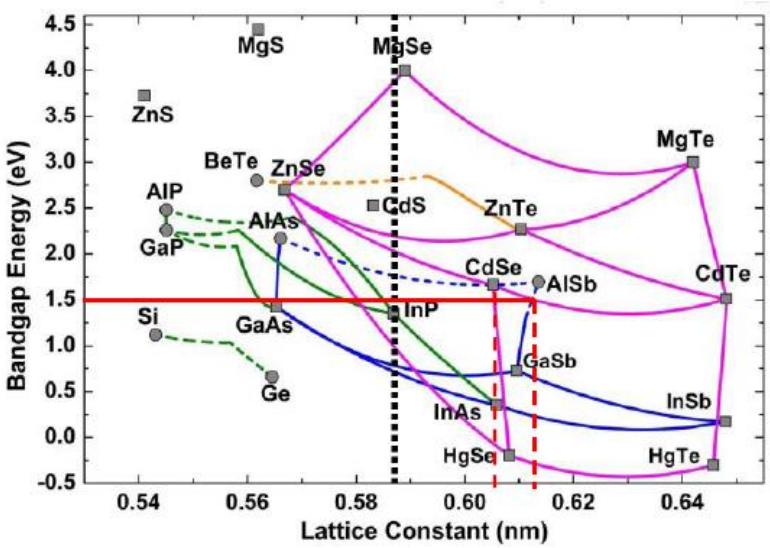

Fig. 5-3 Binary semiconductor compounds vs the network constant [33]

5.1.1.1.2 Define global cell structure P + N, N + P, etc.

In order to define the structure, it is necessary to define the window material and the active layer as well as the dopants and their concentrations.

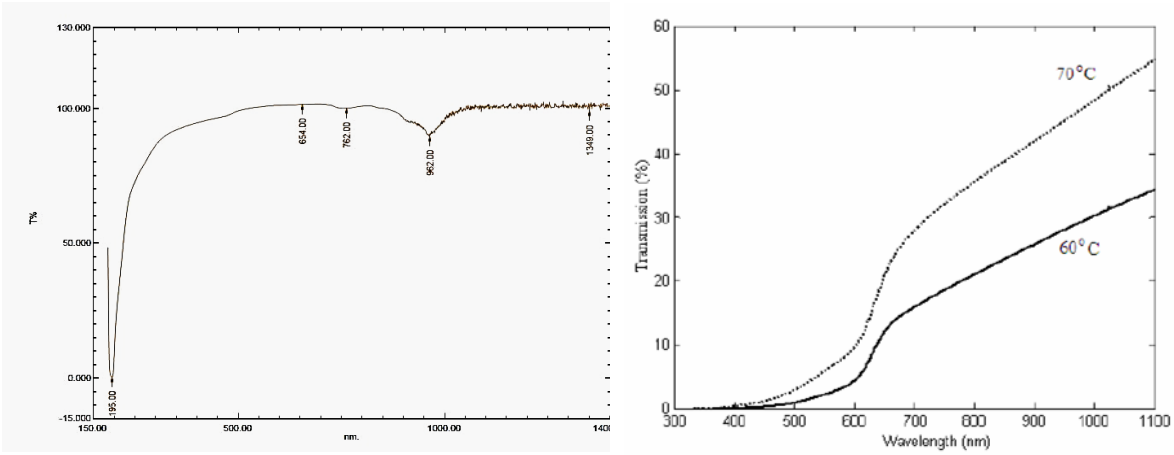

Fig. 5-4 Transmittance spectra (a) CdS, synthesized material (b) CdSe [39]

The window material is defined according to the one with the greatest transmittance, according to Fig. 5-4 the CdS has the highest transmittance that grows in the 450-700 up to 80%

5.1.1.1.3 Define material type P and N

From the synthesized material of CdS it is known that 73.61% is Cd (Table 5-1) this makes this element the majority, and having these 2 valence electrons, the S provides 4 free electrons, since it has 6 valence electrons. The presence of major free electrons converts the CdS into “n” type material. Therefore, the “p” type material will be the CdSe when providing 4 free holes.

Table 5-1 percentages of elements present in synthesized CdS

C (%)	S (%)	Cd (%)
5.9	20.4	73.7

5.1.1.1.4 Define Dopants

Doping atoms have small ionization energy with respect to the bandgap of the doped material. Therefore, we can assume that at room temperature all doping atoms are ionized.

The typical dopants

1. Dopants for cadmium sulfide (CdS)

Type n:

- gallium (replacing the Cd),
- yodine
- fluorine (replacing the S) SELECTED

Type p:

- lithium,
- sodium (replacing Cd)

2. Dopants for cadmium selenide (CdSe)

Type n:

- gallium
- fluor

Type p:

- nitrogen,
- sodium

5.1.1.1.5 Define Heterostructure

As shown in Fig. 5-5, there is a heterostructured arrangement of ITO / CdS / CdSe / Ag / Air, it is proposed to modify active layer thickness, due to the better electrical and optical behavior shown after its analysis, as shown in the results section.

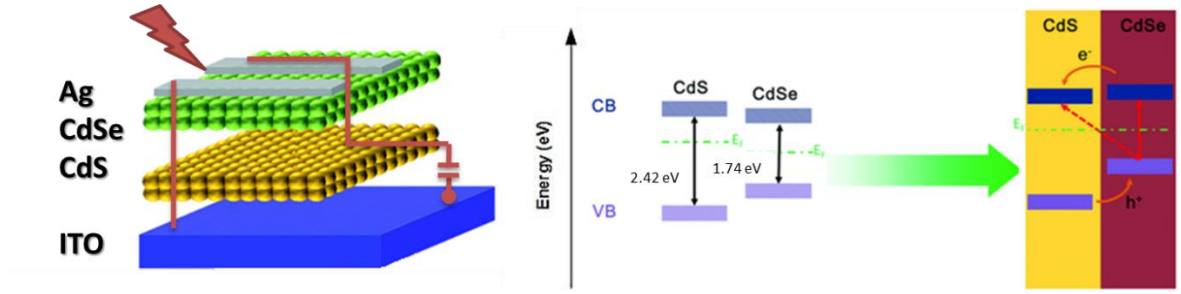

Fig. 5-5 Heterostructure ITO/CdS/CdSe/Ag/Air

Energy Level:

$$E_{gb}CdS = 2.42\ eV$$

$E_{gw}CdSe = 1.74\ eV$

$m_o = 9.11x10^{-31}Kg$

$\hbar = 1.0545x10^{-34}\ J.s$
$\hbar^2 = 1.11197x10^{-68}\ J.s$
$eV = 1.602x10^{-19}\ C$

$a = \frac{d}{2} = \frac{L_z}{2}$

$a = 4.5x10^{-11}\ m$

$L = 90\ Å = 45x10^{-9}\ m$

$q = 1.6x10^{-19}$

$\frac{kT}{q} = 0.026\ V$

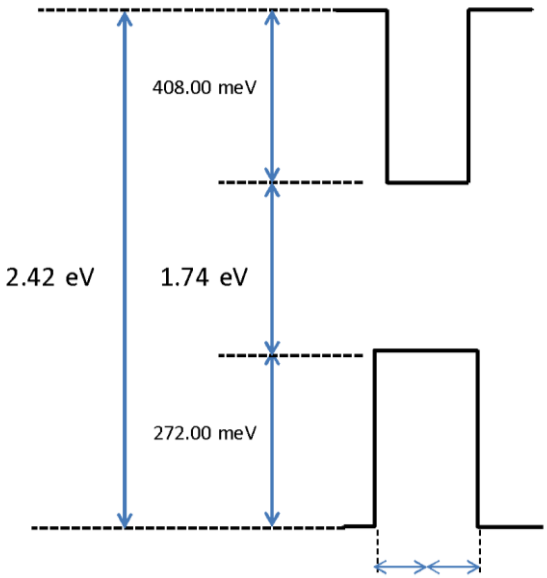

Fig. 5-6 Band Diagram CdS/CdSe

Conduction Band:

$m_{ewp} = 0.13\ * mo = 0.13 * 9.11x10^{-31}\ Kg = 1.1843x10^{-31}\ Kg$ *CdSe electron effective mass*
$m_{ebn} = 0.17\ * mo = 0.17 * 9.11x10^{-31}\ Kg = 1.5487x10^{-31}\ Kg$ *CdS electron effective mass*

$\frac{m_{eb}}{m_{ew}} = 1.3076$

$$\Delta Ec = Vo = (E_{gb} - E_{gw}) * 0.6 = (2.42\ eV - 1.74\ eV) * 0.6 = 0.408\ eV$$

Valence Band:

$$m_{hwp} = 0.45\ * mo = 0.45 * 9.11x10^{-31}\ Kg = 4.0995x10^{-31}\ Kg\ \ CdSe\ hole\ effective\ mass$$
$$m_{hbn} = 0.70 * mo = 0.70 * 9.11x10^{-31}\ Kg\ = 6.377x10^{-31}\ Kg\ \ CdS\ hole\ effective\ mass$$

$$\frac{m_{hb}}{m_{hw}} = 1.5555$$

$$\Delta Ev = Vo = (E_{gb} - E_{gw}) * 0.4 = (2.42\ eV - 1.74\ eV) * 0.4 = 0.272\ eV$$

5.1.1.1.6 Scattering Matrix Calculation

There is a hetero-structured system, wherein the center there is the active layer of $CdSe_{0.4}Te_{0.6}$, according to the matrix resolution technique it is necessary to calculate Interphase matrices and propagation matrices, for each pair of material systems. First, G (x) without quantum well is evaluated.

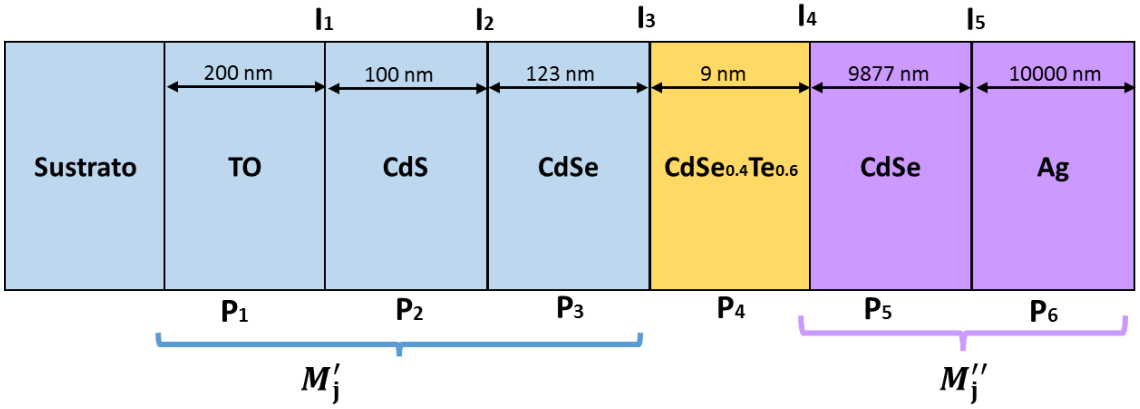

Fig. 5-7 Heterostructured Device

$$r_{ij} = \frac{n_2 - n_1}{n_2 + n_1}$$

$$t_{ij} = 1 + r_{ij}$$

$$I_x = \frac{1}{t_{ij}} * \begin{bmatrix} 1 & r_{ij} \\ r_{ij} & 1 \end{bmatrix} = \begin{bmatrix} \frac{1}{t_{ij}} & r_{ij} * \frac{1}{t_{ij}} \\ r_{ij} * \frac{1}{t_{ij}} & \frac{1}{t_{ij}} \end{bmatrix}$$

$$P_x = \begin{bmatrix} e^{+i\beta_j x} & 0 \\ 0 & e^{-i\beta_j x} \end{bmatrix}$$

$$\beta_j = \frac{2*\pi*d*n_j*coscos\,\theta}{\lambda}$$

$$e_{jx} = (x) + i\ sen(x)) =$$

$$e_{j^+j} = (\beta_j x) + i\ sen(\beta_j x)) =$$

$$e_{j^-j} = (\beta_j x) - i\ sen(\beta_j x)) =$$

$$M' = I_1 P_1 I_2 P_2 I_3 P_3$$

$$d_j = P_4$$

$$M'' = I_4 P_5 I_5\ P_6$$

Transmission coefficient computation

$$t_j' = \frac{1}{M'_{j,11}}$$

Positive reflection coefficient computation

$$r_j' = \frac{M'_{j,21}}{M'_{j,11}}$$

Negative reflection coefficient computation

$$r_{j-}' = -\frac{M'_{j,12}}{M'_{j,11}}$$

M_j'' Transmission coefficient computation

$$t_j'' = \frac{1}{M''_{j,11}}$$

Reflection coefficient computation

$$r_j'' = \frac{M''_{j,21}}{M''_{j,11}}$$

Positive transmission coefficient computation

$$t_j^+ = \frac{t_j'}{1-r_j'-(r_j''*e^{i2\beta_j})}$$

$$t_j^- = t_j^+ * (r_j'' * e^{i2\beta_j})$$

Propagation of the electric field in the study layer

$E_j(x) = \left(t_j^+\right) * \left[e^{i\beta_j x} + r_j'' + e^{i\beta_j(2*d_j - x)}\right] * (E_o^+)$

$E_o^+ = I_c$ Incident electric field

$\left|E_j(x)\right|^2 = (Re)^2 E_j(x) + (Im)^2 E_j(x)$

Flow of energy dissipated in the study layer

$Q_j(x) = \frac{1}{2}\left[C * \varepsilon_0 \alpha_j n_j \left|E_j(x)\right|^2\right]$

Where:

$C = 30X10^9$

$\varepsilon_0 = 8.85X10^{-12}$

$\alpha_j = \frac{4*\pi*k}{\lambda}$

Solving:

$\alpha_j = \frac{4 * \pi * k}{\lambda}$

The exciton generation rate is described with the following equation:

$G_{(x)} = n \int_{360}^{800} \frac{\lambda}{hc} Q_{(x,\lambda)} d\lambda$

Where: $n = 1$ y $h = 6.63X10^{-34}$

5.1.2. Use of Gummel iterative algorithm

To describe the spectrum, the heterostructure band profile, and be able to determine the density of carriers it is necessary to solve the Schrödinger and Poisson equations of the system. Such a solution assumes the following: known the enveloping functions of the occupied states of the heterostructure, as well as

the corresponding auto energies and the Fermi level of the system, there is the local density of charge produced by the carriers.

The presence of carriers in the quantum well significantly affects its potential profile, which in turn will result in different eigenvalues and self-functions when solving the Schrödinger equation, which makes a consistent self-solution of the problem necessary. To start the calculation, an initial solution is assumed, either from the Poisson equation (a potential) or from the Schrödinger equation (a charge density).

In the Gummel method, the equations are solved sequentially. The Poisson equation is solved assuming that Fermi's potentials are fixed. Then the new potential is substituted in the convergence equations, which are linear and can be solved directly.The new carrier concentrations are substituted in turn at the charge term of the Poisson equation and another cycle begins. In each step, only one equation is solved so that the matrix has N rows and N columns regardless of the number of carriers (0/1/2) for which it is simulated. It is a decoupled method: a group of variables remains fixed while solving for another group. The success of this method depends on the degree of coupling between the equations. The most important coupling is due to the carry-over term of the carrier current. As long as the drag stream is not relevant, Gummel's method will be appropriate.

Non-uniform carrier generation – n and p charge densities computation

Since the irradiation is not uniform throughout the entire material. a non-uniform charges generation method is used.

Because the properties of the materials are affected by the exciton generation rate, such as the generation of new charges both in the area of the P-type material and in the N, it is necessary to use different methods to calculate the new values.

One of these proposed methods is the use of the Gummel algorithm. This algorithm allows having a relationship between the load continuity equations (concentrations) and Poisson voltage.

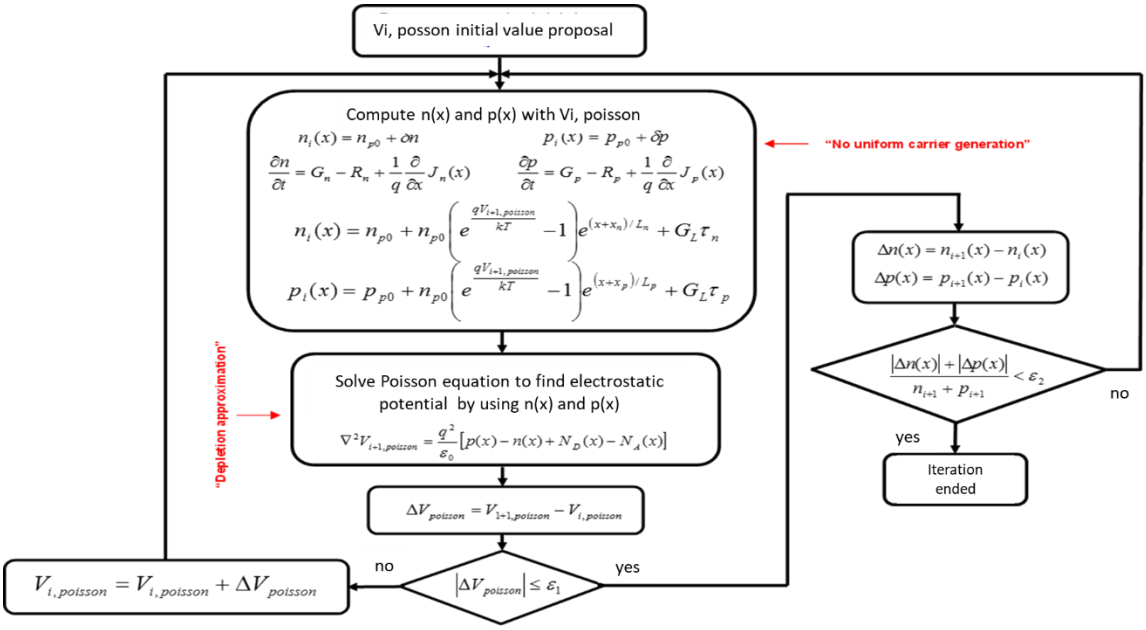

Fig. 5-8 Calculation of charge densities n and p y - "Non-uniform charrier generation"

Calculation of the electrostatic potential V0 (contact potential in a pN junction) by self-consistency in the solution of the Poisson equations - Continuity (Using Gummel's iterative algorithm). Having the concentrations calculated in each respective material, it is necessary to calculate the actual contact voltage or Poisson voltage.

A voltage is proposed and this will be compared with the voltage calculated with the previous equations, and if it meets a margin of error the voltage step is considered terminated, otherwise the previously proposed voltage is replaced:

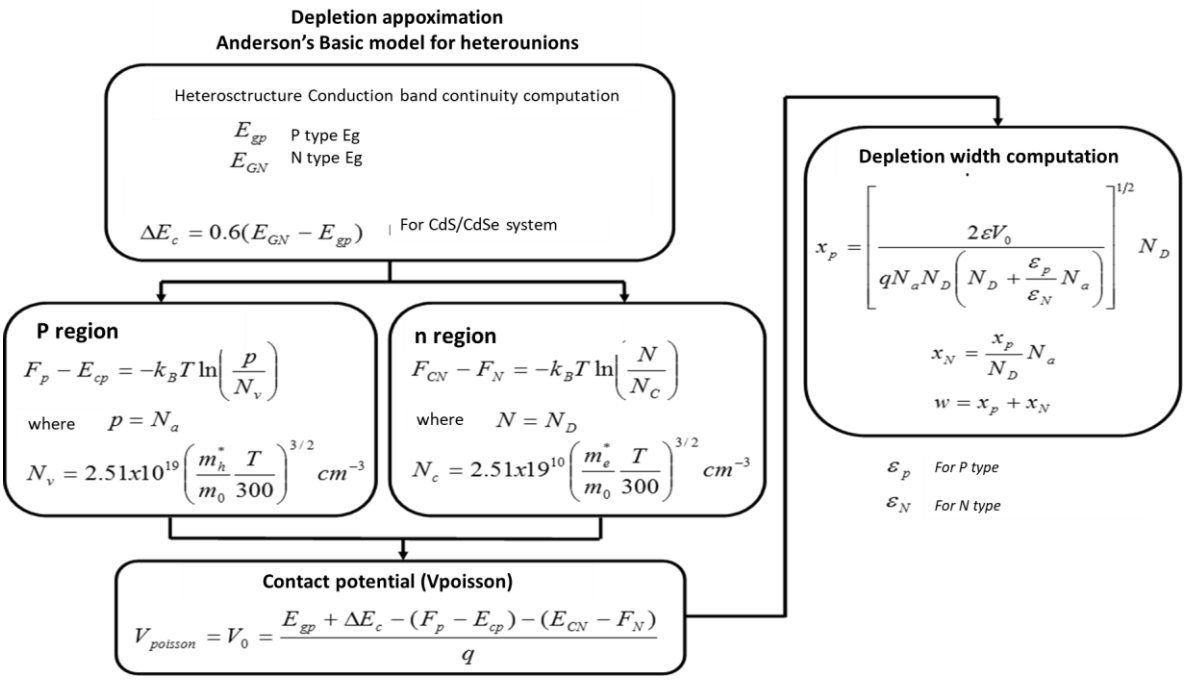

Fig. 5-9 Calculation of the electrostatic potential V0 (contact potential in a pN junction) by self-consistency in the solution of the Poisson equations - Continuity (Using Gummel's iterative algorithm).

5.1.2.1 Calculation of electron and hole diffusion distances

$G_L = 3.29294X10^{26}\frac{m}{s}^{-3}$ It is the rate of generation of minor charges due to photon absorption. Numerical value obtained from Matlab

N Region (CdS)

$n_{in} = 1.6\,x10^{10}\,cm^{-3}$ = intrinsic concentration of charges in CdS T=300K
$n_n = 1.6x10^{10}cm^{-3}$ = concentration of electrons in CdS
$\tau_n = 1\,x10^{-9}\,s$ = recombination time of minority charges in CdS
$\mu_{en} = 340\frac{cm}{Vs}^{2}$= electron mobility in CdS
$\mu_{hn} = 50\frac{cm}{Vs}^{2}$= hole mobility in CdS

$N_d = 5x10^{15} cm^{-3}$ = The concentration of carriers

$D_n = 1.4 \frac{cm}{s}^2$ = Diffusion coefficient of minority charges

$N_c = 2.51x10^{19} \left(\frac{m_{eb}}{m_0} * \frac{T}{300}\right)^{3/2} cm^{-3}$

$N_c = 2.51x10^{19} \left(\frac{0.17m_0}{m_0} * \frac{300}{300}\right)^{3/2} cm^{-3}$

$N_c = 2.51x10^{19}(0.17)^{3/2} cm^{-3} = 1.75x10^{18}$

P region (CdSe)

$n_{iP} = 7.07\ x10^3\ cm^{-3}$ = intrinsic concentration of charges CdSe T=800K

$\tau_p = 16\ x10^{-7}\ s$ = recombination time of minority charges in CdSe

$\mu_{ep} = 500 \frac{cm}{V-s}^2$= electron mobility in CdSe

$\mu_{hp} = 10 \frac{cm}{V-s}^2$= hole mobility in CdSe

$N_a = 1x10^{15} cm^{-3}$ = The concentration of carriers

$D_p = 15.25 \frac{cm}{s}^2$ = Diffusion coefficient of minority charges

$N_v = 2.51x10^{19} \left(\frac{m_{ew}}{m_0} * \frac{T}{300}\right)^{3/2} cm^{-3}$

$N_v = 2.51x10^{19} \left(\frac{0.45m_0}{m_0} * \frac{300}{300}\right)^{3/2} cm^{-3}$

$N_v = 2.51x10^{19}(0.45)^{3/2} cm^{-3} = 7.57x10^{18}$

Hole diffusion length

$L_n = \sqrt{D_n \tau_n} = \sqrt{\left(9 \frac{cm^2}{s}\right)(1\ x10^{-7}\ s\quad)}$

$L_n = 0.000949\ cm = 9.49 \mu m$

Electron diffusion length

$L_p = \sqrt{D_p \tau_p} = \sqrt{\left(15.25 \frac{cm^2}{s}\right)(1.5x10^{-8} s\quad)}$

$L_p = 0.000478 cm = 4.78 \mu m$

Concentration in minority charges

$$n_{P0} = \frac{n_{iP}^2}{N_a} = \frac{(7.07x10^3)^2}{1x10^{25}} = 4.998x10^{-18}cm^{-3}$$

$$P_{n0} = \frac{n_{in}^2}{N_d} = \frac{(1.6x10^{10})^2}{5x10^{25}} = 5.12x10^{-6}cm^{-3}$$

5.1.2.2 Calculation of Depletion zone limits - Gummel Algorithm

A contact voltage in proposed $V0$=0.6 V.

$$\varepsilon_n = 8.9$$

$$\varepsilon_P = 10.2$$

$$\varepsilon_0 = 8.854x10^{-12}C^2/Nm^2 = 8.854x10^{-14}C^2/Ncm^2$$

$$x_p = \left[\frac{2\varepsilon_p V_0}{qN_aN_d\left(N_d + \frac{\varepsilon_P}{\varepsilon_n}N_a\right)}\right]^{\frac{1}{2}} N_d$$

$$= \left[\frac{2(10.2)(8.854x10^{-14})(0.6)}{(1.6x10^{-19})(1x10^{15})(5x10^{15})\left(5x10^{15} + \frac{10.2}{8.9}(1x10^{15})\right)}\right]^{\frac{1}{2}} (5x10^{15})$$

$$x_n = \frac{x_p}{N_d}N_a = \frac{7.577x10^{-5}cm}{5x10^{15}}(1x10^{15}) = cm$$

$$x_w = x_p + x_n = cm$$

Calculation of charge concentrations - "Non uniform charrier generation"

$$P_N(x) = P_{NO} + P_{NO}\left(e^{\frac{qV_o}{kT}} - 1\right)e^{\frac{-(x-x_n)}{L_p}} + G_L\tau_p = \ cm^{-3}$$

$$n_p(x) = n_{po} + n_{po}\left(e^{\frac{qV_o}{kT}} - 1\right)e^{\frac{(x-x_p)}{L_n}} + G_L\tau_n = cm^{-3}$$

Calculation Poisson voltage

Since our model presents a heterojunction, it will be necessary to use the "Depletion approximation" algorithm, which is based on the calculation of quasifermis:

$$F_{CN} - F_N = -k_B T ln\left(\frac{n_p(x)}{N_c}\right) = eV$$

$$F_p - E_{cp} = -k_B T ln\left(\frac{P_N(x)}{N_v}\right) = eV$$

Contact potential calculation V0

$$V_{0=}\frac{\left[E_{gp} + \Delta Ec - \left(F_p - E_{cp}\right) - \left(F_{CN} - F_N\right)\right]q}{q} = mV$$

$$\Delta V_{poisson} = V_{i+1,poisson} - V_{i,poisson}$$

$$\Delta V_{poisson} = 1.624819 - .6$$

$|\Delta V_{poisson}| > 1$ **If yes, end of the iteration**

$x_w = 0.890775\mu m = 890.775\ nm$

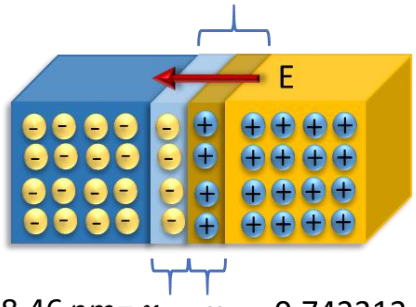

n=$3.292941x10^{11}cm^{-3}$ P=$1.173189x10^{15}cm^{-3}$

$0.1484625\mu m = 148.46\ nm = x_n$ $x_P = 0.742312\mu m = 742.31\ nm$

$$\boldsymbol{V_0 = V_{contacto-poisson}} = 1.5219\ V$$

$$G_L = 3.29294X10^{26}\frac{m^{-3}}{s}$$

Fig. 5-10 Calculation of Depletion zone limits

5.1.3 Characterization of the device without quantum well - Calculation of the photogenerated voltage at maximum power

To characterize the device, it is necessary to obtain the current and voltage parameters.

Open circuit voltage calculation

$$V_A = V_{oc} = \frac{kT}{q} ln \left(\frac{qG_L(L_p + L_n)}{(q\frac{D_p}{L_p} P_{NO} + q\frac{D_n}{L_n} n_{po})} + 1 \right)$$

To find the current density, values of VA from zero to Voc will be evaluated in the following function:

$$J_{SC} = \left(q\frac{D_p}{L_p} P_{NO} + q\frac{D_n}{L_n} n_{po} \right) \left(e^{\frac{qV_A}{kT}} - 1 \right) - qG_L(L_p + L_n) =$$

The short circuit current density is obtained by evaluating VA = 0, as follows:

$$J_{SC} = J = -qG_L(L_p + L_n)$$

Evaluating for all voltages, from VA = 0 to $VA = Voc$

To find the optimal load and the Fill-Factor Find the value of both V and J that offers the maximum power.

$$P = V \cdot J$$

$$V_{maxP} = 0.3104\ V$$

$$J_{maxP} = Maximum\ current\ density = \ 0.0050503\ A/cm^2$$

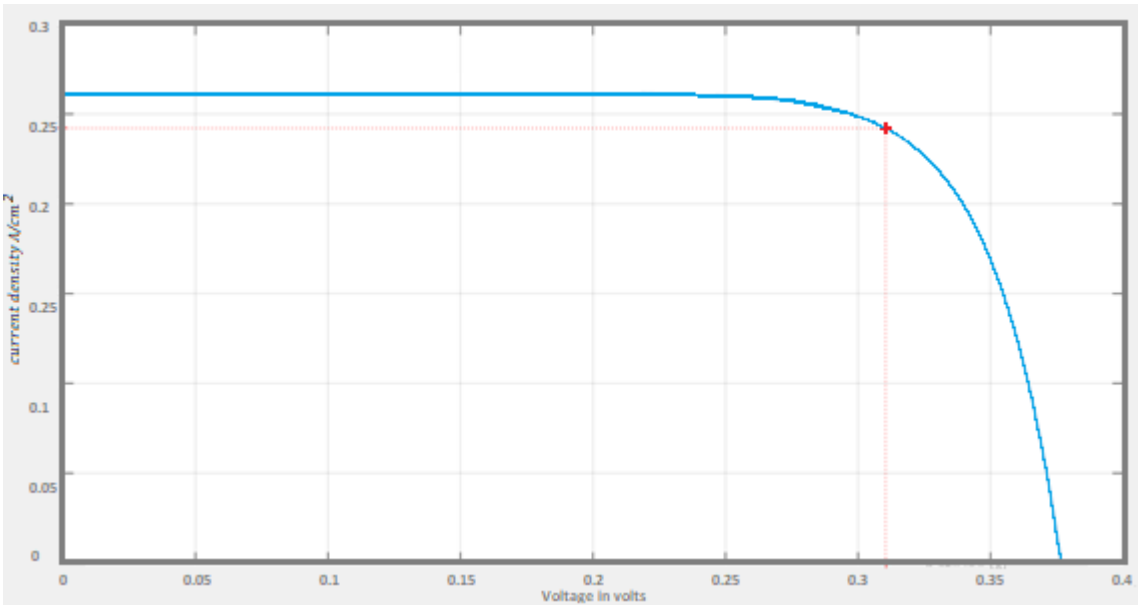

Fig. 5-11 Current Density Vs Voltage

W calculation

Substrates 100 μm wide by 100 μm long will be used.

$$W = x\% * \frac{Imax}{LJmax} = \mu m$$

Which is not less than the width of the substrate and does not meet the design requirements. Other important parameters to calculate are:

$P=V_{max} \bullet J_{max}= W/cm^2$

The maximum power current:

$I_{max}=J_{max}*W*L$=mA

The resistence:

$$R_{mp} = \frac{V_{max}}{I_{max}} = \Omega$$

The fill factor:

$$FF = \frac{V_{max}J_{max}}{V_{oc}J_{sc}}$$

Power conversion efficiency:

$$n_{power} = \frac{V_{mp}J_{mp}}{P_{incidente}} = FF\,\frac{V_{oc}J_{sc}}{P_{incidente}} =.$$

Unit cell necessary to meet the requirements defined at the beginning.

The number of unit cells is defined with respect to the maximum voltage, obtained from the graph, an initial requirement of 5 V is assumed:

$$\#CU = \frac{V_{mp}}{V_{max}} = \frac{5\ V}{0.3104\ \ V} = 16.10 \sim 16\ photodiodes$$

I_{max}=20 mA, I_{mp}= 300 mA for the current compliance of each mesh:

$$\#Mesh = \frac{I_{mp}}{I_{max}} = \frac{300\ mA}{22\ mA} = 13.63 \sim 14\ mesh$$

Nominally 14 meshes of 16 cells each are needed.

5.1.4 Inclusion of Quantum wells

For the inclusion of wells it is necessary to follow the following algorithm, defining central wavelength, width d of the active layer of the quantum well by self-consistency in the solution of the Schrodinger – Poisson equations.

5.1.4.1 Bang Gap Selection

However, it is desired to introduce a quantum well (QW) in the active layer depletion zone (CdSe).

The material of the quantum wells (QWs) must have a lower Band Gap than that of the material in the depletion zone and since it is required to focus the absorption of

the well at 825 nm, in order to achieve a higher solar incidence, according to the highest irradiance peak shown in Fig. 5-1 Photon incident flux spectrum standard and using the Plank relationship

$$E = \frac{hc}{\lambda}$$

$$E_g = \frac{1.24}{0.825} = 1.5eV$$

5.1.4.2 Materials selection

For Quantum Well Barriers:

Since the quantum well will be inserted into the depletion zone of the active layer of the PN junction, therefore, the barrier material will be the same material as the active layer of the pn CdSe junction (type p).

For Active Quantum Well Layer:

The material of the active layer of the quantum well must be a material with a network affinity to the barrier and a Band Gap of 1.5 eV, as previously defined, for which it is necessary to consult the chart of binary semiconductor compounds versus the constant network (Fig. 5-3), from which it is determined that the compound that satisfies the requirements of the Bang Gap is a ternary material with a composition $CdSe_xTe_{1-x}$.

The mole fractions of this ternary compound ($CdSe_xTe_{1-x}$) are determined using the following relationship [40]:

$$E_x = E_A + (E_B - E_A - b)x + bx^2$$

Where

Ex is the bandgap of the component $CdSe_xTe_{1-x}$

E_A is the bandgap of the CdTe component

E_B is the bandgap of the CdSe component

X composition of the Se

B Reverence or adjustment parameter

Once resolved for a Bang gap of the desired $CdSe_xTe_{1-x}$ component of 1.5, we obtain that x = 0.4 with an adjustment parameter of 0.508 [40], therefore the mole fractions are established as $CdSe_{0.4}Te_{0.6.}$ Given the above, knowing the materials, their effective masses, and the bandgap of each one of them, the energy diagram is as follows:

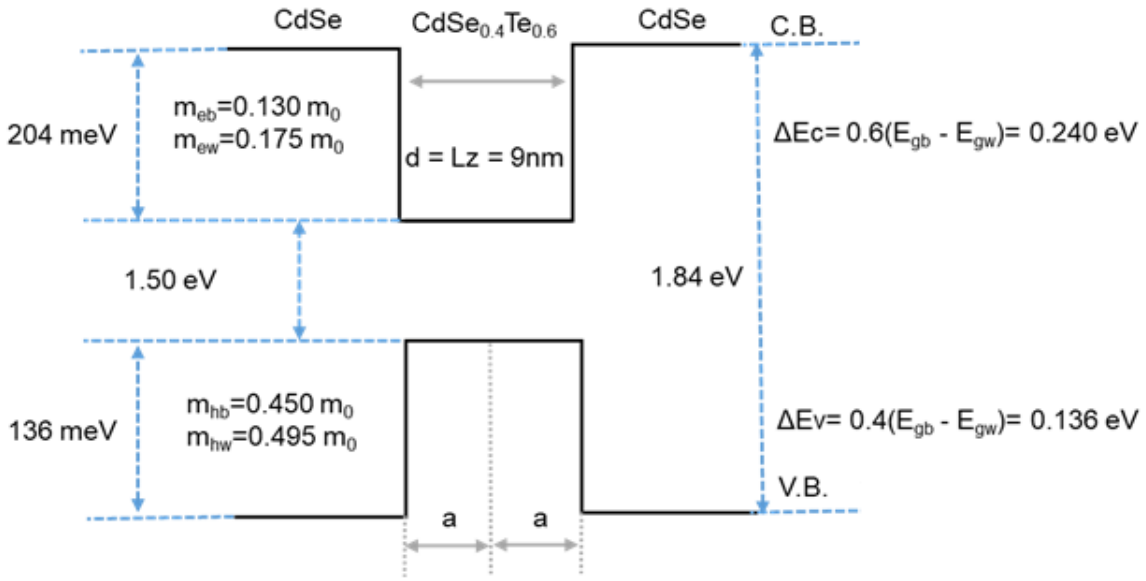

Fig. 5-12 Band Diagram CdSe/ $CdSe_{0.4}Te_{0.6}$

So given these conditions, the assigned device is left with the following structure:

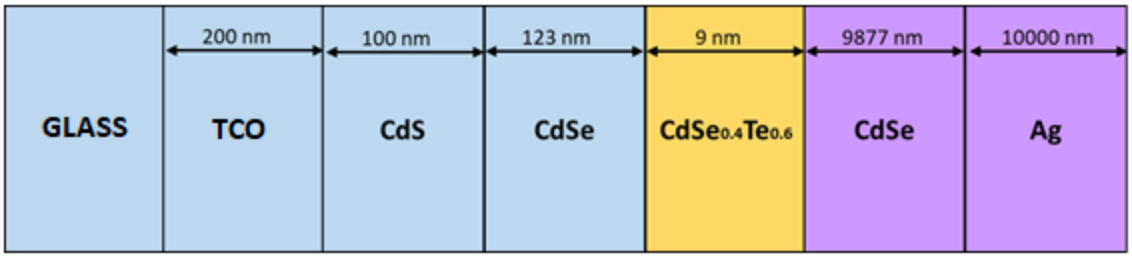

Fig. 5-13 Device to study with assigned and proposed active layer thickness

5.1.4.3 Calculation of energy levels and quasi-fermi levels

The energy levels in the conduction band and the valence band are calculated for a quantum well-formed by the CdSe / $CdSe_{0.4}Te_{0.6}$ / CdSe material system with different effective masses. Additionally, find quasi-fermi levels

$\boldsymbol{Eg(CdSe\ a\ 300\ K)=1.84\ eV}$
$\boldsymbol{Eg(CdSe0.4Te0.6\ a\ 300\ K)=1.50\ eV}$
$\boldsymbol{\Delta Eg=Eg}\text{barrier}-\boldsymbol{Eg}\text{welll}$
$\boldsymbol{\Delta Eg=1.84-1.50=0.34\ eV=340\ meV}$
$\boldsymbol{\Delta Ec=0.6\Delta Eg=240\ meV}$
$\boldsymbol{\Delta EV=0.4\Delta Eg=136\ me}\text{V}$

Constant and variable values for calculating conduction band levels.

$m_0 = 9.11x10^{-31}Kg$

$m_{be} = 0.130\, m_0$ electron effective mass in the CdSe (Kg)
$m_{we} = 0.175\, m_0$ electron effective mass in the $CdSe_{0.4}Te_{0.6}$ (Kg)
$V_0 = -204\, meV$

Constants and variables for the calculation of the levels of the valence band.

$m_0 = 9.11x10^{-31}Kg$

$m_{bh} = 0.450\, m_0$ hole effective mass in the CdSe (Kg)
$m_{wh} = 0.495\, m_0$ hole effective mass in the $CdSe_{0.4}Te_{0.6}$ (Kg)
$V_0 = -136\, meV$

$\hbar = 1.0545x10^{-34}\, J.s$
$\hbar^2 = 1.11197x10^{-68}\, J.s$
$eV = 1.602x10^{-19}\, C$

$$a = \frac{d}{2} = \frac{L_z}{2} = \frac{90x10^{-9}\, m}{2} = 45x10^{-9}\, m = 45\text{Å}$$

Solving the Schrödinger equation for finite dregs, to obtain the discrete representation of the energy levels of the system, the following equations are obtained:

$$K = \sqrt{-\frac{2*m_b*eV*001*E}{\hbar^2}}$$

$$K_{II} = \sqrt{\frac{2*m_{W*eV*001*(E+V_o)}}{\hbar^2}}$$

$$(K_{II}a)^2 + \frac{m_b}{m_w}(Ka)^2 = \frac{a^2 2m_W}{\hbar^2}V_o$$

$$Ka = \frac{m_b}{m_w}K_{II}a\ \ tan\, tan\,(K_{II}a)$$

$$Ka = -\frac{m_b}{m_w}K_{II}a\ \ cot\, cot\,(K_{II}a)$$

The “Eigen-equations” are the solutions for $\boldsymbol{K\ y\ KII}$ obtained from the intersections of the circle. The values of "eigen-energy" can be found with the following equations:

The following formula was used to obtain the energy levels of the conduction band:

$$E_{mc} = V_o - |E_{mn}|$$

Where the subscript m is an integer greater than zero but less than infinity, therefore to obtain the first two values of the conduction band, modify

$$E_{1c} = V_o - |E_{1n}|$$

$$E_{2c} = V_o - |E_{2n}|$$

The following formula was used to obtain the energy levels of the valence band:

$$E_{mv} = V_o - |E_{mp}|$$

Where the subscript m is an integer greater than zero but less than infinity, therefore to obtain the first two values of the valence band, modify the

$$E_{1v} = V_o - |E_{1p}|$$

$$E_{2v} = V_o - |E_{2p}|$$

Once you have the first levels of the conduction band and valence respectively, E1n and E1p, you can calculate the actual or effective wavelength of the system.

$$\lambda eff = \frac{1.24}{E_g + E_{1n} + E_{1p}}$$

Substituting the E1n, E1p and Eg values of the active layer

$$\lambda eff = 0.6856\, nm$$

Obtaining the differences of the first 2 levels of the conduction and valence bands of the well we have

$$\Delta E_n = E_{2c} - E_{1c}$$

$$\Delta E_p = E_{2v} - E_{1v}$$

Substituting the previously found values:

Quasi-Fermi´s

$$\left(1 + e^{\frac{E_{Fn}}{kT}}\right)\left(1 + e^{\frac{(E_{Fn} - \Delta E_n)}{kT}}\right)$$

$$\left(1 + e^{\frac{E_{Fp}}{kT}}\right)^Z \left(1 + e^{\frac{(E_{Fp} - \Delta E_p)}{kT}}\right)^Z$$

$$Z = \frac{m_p}{m_n}$$

Code in Matlab is used to obtain the Quasi Fermis, the values of Efn and Efp are searched iteratively. The graphics will be presented simultaneously with the Matlab subplot matrix function, the image of which is shown in the Fig 5-14.

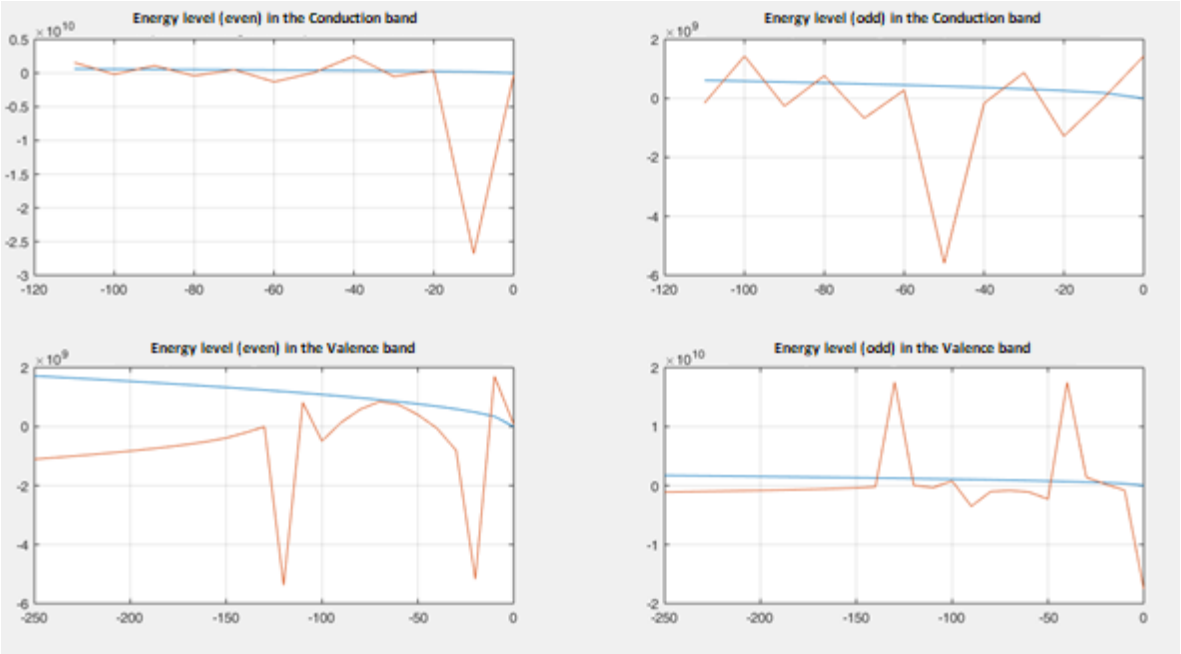

Fig. 5-14 Intersections for odd and even energy levels in the Valence Band and Conduction

Once the intersections are obtained, the calculation of energy levels and quasi-fermi levels are calculated, using a Matlab code, the following results are obtained:

the value of deltaEc is: = 2.040000e + 02 meV

the value of Ec1 is: a = 1.950394e + 02 meV

the value of Ec2 is: a = 1.840400e + 02 meV.

the value of Ec3 is: a = 1.689147e + 02 meV.

the value of Ec4 is: a = 1.712200e + 02 meV.

the value of Ec5 is: a = 1.216752e + 02 meV.

the value of Ec6 is: a = 1.340900e + 02 meV.

the value of Ec7 is: a = 9.874500e + 01 meV.

the value of Ec8 is: a = 1.176900e + 02 meV.

the value of Ec10 is: a = 9.950000e + 01 meV.

the value of deltaEv is: = 1.360000e + 02 meV.

the value of Ev1 is: a = 1.136800e + 02 meV.

the value of Ev2 is: a = 1.240500e + 02 meV.

the Ev3 value is: a = 1.534000e + 01 meV.

Assigned emission center frequency in micrometers at: 0.8250.

Actual system center emission frequency in micrometers at: 0.6856.

It is above the absorption length of the CdSe (673.9nm), therefore it satisfies the placement expectation of the quantum well.

Only the first two levels are considered in both camps.

the value of deltaEc is: = 2.040000e + 02 eV.

the value of En1 is: a = 1.950394e-01 eV.

the value of En2 is: a = 1.840400e-01 eV.

the value of deltaEv is: = 1.360000e + 02 eV.

the value of Ep1 is: a = 1.136800e-01 eV.

the value of Ep2 is: a = 1.240500e-01 eV.

Quasi-fermi levels

EFn =0.1950

EFp = 0.1137

EFm = 0.3087

Knowing the energy levels and the quasi-fermi levels, we proceed to calculate the Absorption Coefficient in a DQW for the case of partial selection of moment “k”.

$$\alpha(v) = \frac{1}{v_g}\left[B(v)hI_{abs}(E) + \frac{1}{\tau_{loss}}\right]$$

E_t= Maximum position in the Lorenzian function

$L_z = 90\ \text{Å} = 90x10^{-10}m$

$CdSeTe$

$m_0 = 9.1093x10^{-31}kg$

$m_n = 0.175m_0$

$m_p = 0.495m_0$

ħ= $1.054571x10^{-34}\frac{m^2kg}{s}$

ħ= $1.054571x10^{-30}\frac{cm^2kg}{s}$

ħ= $6.582118x10^{-16}eV * s$

$h = 6.63x10^{-30}\frac{cm^2kg}{s}$

$n_g = 3.2$

$E_g = 1.5\ eV$

$\tau_{loss} = 2.5x10^{-11}s$

$\tau_{in} = 1x10^{-12}s$

$Ab = 2x10^{-10}\frac{cm^3}{s}$

$\tau_{loss} = 2.5x10^{-11}s$

$c = 2.997x10^{-10}\frac{cm}{s}$

$$D_nD_p = \frac{m_nm_p\ x\ 10^{-8}}{\pi^2\hbar^4}$$

$$\lambda_{eff} = \frac{1.24}{E_g + E_{1n} + E_{1p}}$$

$$a = \frac{1}{\frac{m_n}{m_p} + 1}$$

$$b = 1 - a$$

$$B(v) = \frac{A_b c^3}{8\pi v^2} = \frac{A_b c^3}{8\pi(\frac{c}{\lambda})(\frac{c}{\lambda})} = \frac{A_b c \lambda^2}{8\pi} = \frac{cm^6}{s^2}$$

$$h\delta v_{min} = \frac{\hbar}{\tau_{in}}$$

$$v_g = \frac{c}{n_g}$$

5.1.4.4 for the calculation of the absorption coefficient α for photons the absorption

The absorption coefficient is given by:

$$\alpha(v) = \frac{1}{v_g}\left[B(v)hI_{abs}(E) + \frac{1}{\tau_{loss}}\right]$$

where:

$$I_{ABb} = \frac{D_{1n}D_{1p}}{Lz^2} * \frac{1}{1 + exp\left[\frac{E_{Fn} - ah\tilde{\nu}}{kT}\right]} * \frac{1}{1 + exp\left[\frac{E_{Pn} - bh\tilde{\nu}}{kT}\right]} * \frac{h\delta v_{min}}{2}\left[tan^{-1}\left(\frac{2bh\tilde{\nu}}{h\delta v_{min}}\right) + tan^{-1}\left(\frac{2ah\tilde{\nu}}{h\delta v_{min}}\right)\right]$$

For the case where E_{Fn} y E_{Pn} are very close to or below E_c y E_v:

$$I_{ABb} = \frac{D_{1n}D_{1p}}{Lz^2} * \frac{h\delta v_{min}}{2}\left[tan^{-1}\left(\frac{2bh\tilde{\nu}}{h\delta v_{min}}\right) + tan^{-1}\left(\frac{2ah\tilde{\nu}}{h\delta v_{min}}\right)\right]$$

Dividing into sections

$$Section\ 1 = B(v)h * \frac{D_{1n}D_{1p}}{Lz^2} * \frac{h\delta v_{min}}{2}$$

$$Section\ 2 = \left[tan^{-1}\left(\frac{2bh\tilde{\nu}}{h\delta v_{min}}\right) + tan^{-1}\left(\frac{2ah\tilde{\nu}}{h\delta v_{min}}\right)\right]$$

Thus:

$$\alpha(v) = \frac{1}{v_g}\left[section\ 1\ * section\ 2 + \frac{1}{\tau_{loss}}\right]$$

Graph of the absorption coefficient α against the energy of the absorbed photons. Absorption is given by:

$$\alpha(v) = \frac{1}{v_g}\left[B(v)hI_{abs}(E) + \frac{1}{\tau_{loss}}\right]$$

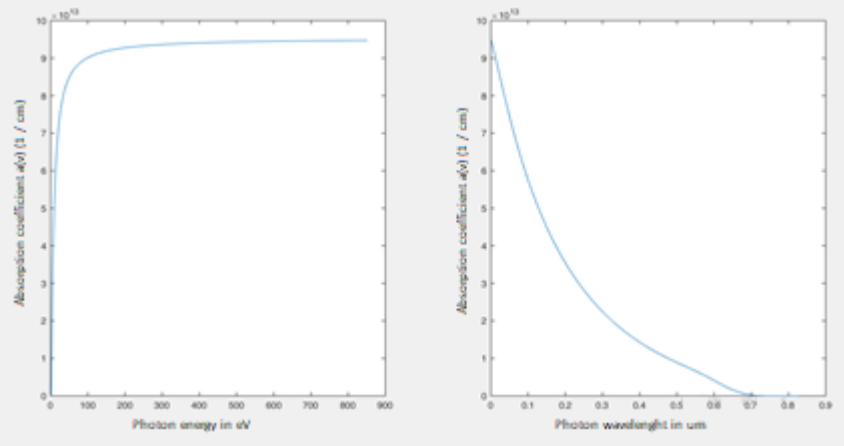

Fig. 5-15 Characterization results according to algorithm resolution in Matlab

Bv = 1.1209e-09 cm^6 / s^2

hsv Energy level up to which more than EFn = 6.5821 meV can be absorbed

Vg Group speed of photons in the material = 9365625000 cm / sec.

Density of states DnDp = 5.876530010066764e + 65 1 / J^2cm^4

Effective wavelength = 0.82119 um

Section1 = 306336139.6337

Section 2 = 0.0030385

Absorption coefficient at (v) = 930818.1898 (1 / cm).

Contribution of the quantum well in the generation of Excitons

You want to know what is the contribution of the quantum well in the generation of exitons, for which, the exciton generation rate is calculated in the quantum

well (G_{jTQW}) and this is adhered to the exciton rate of the device without quantum well (G_{jT}).

$$ni^2 = ni^2 + ni^2{}_{QW}$$
$$G_{jT} = G_{jT} + G_{jTQW}$$

Results obtained from the self-consistent solution of the Load-Poisson Continuity equations

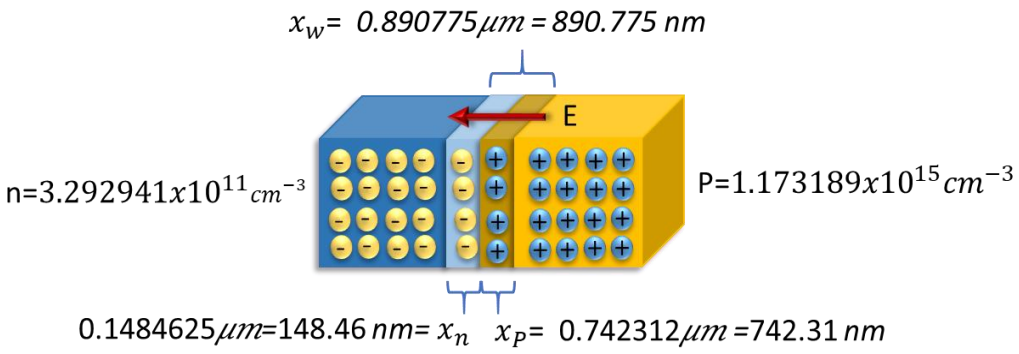

$$\boldsymbol{V_0 = V_{contacto-poisson}} = 1.5219\ V$$

$$G_L = 3.29294X10^{26}\frac{m^{-3}}{s}$$

Fig. 5-16 Dimensioning of the depletion zone in the device without quantum well

Depletion zone limit

Xp = 7.423126e-05 cm

Xn = 1.484625e-05 cm

XW = 8.907751e-05 cm.

Concentration of charges at x = 0,

Pn (x) = 1.173189e + 15 cm^{-3}

np (x) = 3.292941e + 11 cm^{-3}.

Vpoisson in region n and P: 6.009220e + 02 mV

Exciton generation: 3.29294E + 26

Vo = 1.521979e + 00 V

Results obtained for the width of the well

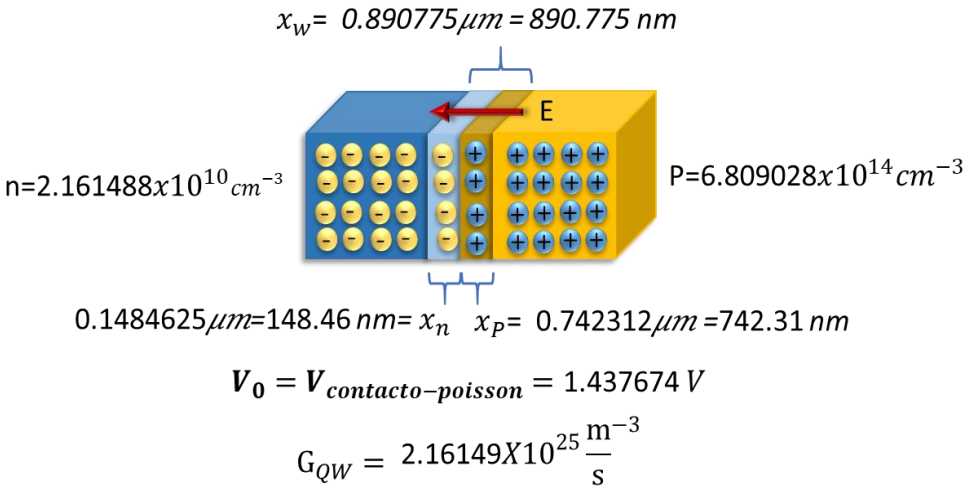

Fig. 5-17 Dimensioning of the depletion zone in the width of the well

Depletion zone limit

Xp = 7.423126e-05 cm

Xn = 1.484625e-05 cm

XW = 8.907751e-05 cm.

Charge concentration at x = 0,

PnQW (x) = 6.809028e + 14 cm^{-3}

npQW (x) = 2.161488e + 10 cm^{-3}.

Vpoisson in region n and P: 6.008377e + 02 mV

Generation of excitons GQW: 2.16149E + 25

Vo = 1.437674e + 00 V

Solving the equations

$ni^2 = 3.8632\ x\ 10^{26} cm^{-3}$

$ni^2{}_{QW} = 1.4717\ x\ 10^{25} cm^{-3}$

$G_{jT} = \ 3.2929 x\ 10^{26} m^{-3} s^{-1}$

$G_{jTQW} = 2.1614\ x\ 10^{25} m^{-3} s^{-1}$

$ni^2 = ni^2 + ni^2{}_{QW} = 4.0103\ x\ 10^{26} cm^{-3}$

$G_{jT} = G_{jT} + G_{jTQW} = 3.50904\ x\ 10^{26} m^{-3} s^{-1}$

5.2 References

[1] P. Winsemius, F. F. van Kampen, H. P. Lengkeek, and C. G. van Went, J. Phys. F 6, 1583 (1976)

[2] Mikhail Polyanskiy (2008-2020). RefractiveIndex. INFO website. Online at: https://refractiveindex.info/

[3] “Structural and optical studies of thermally evaporated CdSexTe1-x thin films” autores S.S.Patil y P.H.Pawar de la revista J. Chem.Bio. Phy.Sci. C,2012, Vol.2, No.3, 1472-1484

[4] Federal Standard 1037C (1996). Online at bldrdoc.gov

[5] Humberto Gabriel Castro Lora, Estudio de las propiedades ópticas y estructurales en películas delgadas de ZnSe Universidad Nacional de Colombia, Facultad de Ciencias Básicas, Departamento de Física. Bogotá, Colombia. 2013

[6] M. S. Hossain, R. Islam, M. Shahjahan and K. A. Khan, Studies on the thermoelectric effect in semiconducting ZnTe thin films, Journal of Materials Science: Materials in Electronics, 19, (2008) 1114-1121.

[7] J. Y. Pankov, Optical Processes in semiconductors. Dover Publications Inc, New York. 1971.

[8] R. H. Bube, Electronic Properties of Crystalline Solids: An Introduction to Fundamentals. Academic Press New York, 1974.

[9] J. Singh, Optical Properties of Condensed Matter and Applications, John Wiley & Sons Ltd, 2006.

[10] M. Fox, Optical Properties of Solids, Oxford University Press, 2001.

[11] KLA Corporation (2020) Refractive Index of ITO, Indium Tin Oxide, InSnO online at: http://www.filmetrics.com/refractive-index-database/ITO/Indium-Tin-Oxide-InSnO

[12] Johnson and Christy (1972) Optical constants of Ag (Silver) Online at https://refractiveindex.info/?shelf=main&book=Ag&page=Johnson

[13] US departament of energy. NREL Solar Spectra Online at: http://rredc.nrel.gov/solar/spectra/am1.5/astmg173/astmg173.html

[14] Raymond Serway & Jewett J (2003). Physics for scientists and engineers (6th ed.). Belmont CA: Thomson-Brooks/Cole. ISBN 0-534-40842-7

[15] John Archibald Wheeler, 'On the Mathematical Description of Light Nuclei by the Method. of Resonating Group Structure' Phys. Rev. 52, 1107 - 1122 (1937)

[16] Jagdish Mehra, Helmut Rechenberg, The Historical Development of Quantum Theory (Pages 990 and 1031) Springer, 2001 ISBN 0-387-95086-9, ISBN 978-0-387-95086-0

[17] American Meteorological Society (20 February 2012) extinction coefficient. Online at: http://glossary.ametsoc.org/wiki/Extinction_coefficient

[18] P. Schewe, B. Stein, D. Castelvecchi. Coherent Exciton Matter. (2006) AIP (Physics News Update), 800 (1), http://www.aip.org/pnu/2006/split/800-1.html

[19] Semiconductors, Physics of Group II-VI and I-VII compounds, Semimagnetic, Semiconductores, edited by K.-H. Hellwege and O. Madelung, Landolt-Bornstein, New Series, Group III,Vol. 17-B, Springer- Verlag, Berlin, (1982).

[20] Advances in the II-VI Compounds Suitable for Solar Cell Applications, 2014: 000-000 ISBN: 978-81-308-0533-7 Editor: Shadia J. Ikhmayies

[21] “Comparative theoretical study of the size dependent electronic and optical properties in CdS and CdSe spherical nanocrystals”. Amjad Nazzal and Huaxiang Fu Department of Physics, University of Arkansas, Fayetteville, Arkansas 72701, USA (Dated: July 31, 2008)

[22] Rodríguez Rodríguez, Pedro “Propiedades ópticas de nanoshells semiconductoras II-VI : efecto de temperatura y tamaño”., http://hdl.handle.net/10016/16076

[23] Low-dimensional CdS/CdTe multiple-quantum well heterostructure for optical refrigeration”. Julio C. Tarín-Cordero, Rafael Villa-Angulo, José R. Villa-Angulo, and Carlos Villa-Angulo* Autonomous University of Baja California, Institute of Engineering, s/n De la Normal Avenue, Insurgentes, Mexicali, B.C. 21280, México.

[24] Mikhail Polyanskiy (2008-2020). RefractiveIndex. INFO website. Online at: https://refractiveindex.info/?shelf=main&book=CdS&page=Treharne

[25] Mikhail Polyanskiy (2008-2020). RefractiveIndex. INFO website. Online at: https://refractiveindex.info/?shelf=main&book=CdSe&page=Lisitsa-o

[26] Christiana Honsberg and Stuart Bowden (2019) PVEducation. Online at: http://pveducation.org/pvcdrom/materials/CdSe

[27] Repositorio institucional e-Archivo http://e-archivo.uc3m.es Trabajos académicos Proyectos Fin de Carrera 2012-07

[28] Escuela técnica Superior de Ingenieros de telecomunicacion (2018) Online at: https://www.tel.uva.es/descargar.htm;jsessionid=2ABCCC69DA8C54AC1210AC74B819C09C?id=13322.

[29] B.G. Streetman, S. Banerjee, Solid State Electronic Devices, Prentice Hall, 2000

[30] Tesis Doctoral "EL GAS ELECTRÓNICO EN SISTEMAS CONFINADO SEMICONDUCTORES CUÁNTICOS MEMORIA presentada por LEONOR CHICO GÓMEZ, INSTITUTO DE CIENCIA DE MATERIALES, CSIC Madrid, 1993

[31] E. F. Schubert , Light-Emitting Diodes, 2nd ed. (Cambridge University Press, Cambridge, 2006),

[32] Fred Schubert National Compound Semiconductor Roadmap (2018) Online at: https://www.ecse.rpi.edu/~schubert/Light-Emitting-Diodes-dot-org/chap21/chap21.htm

[33] Helmut Föll (2017). III-V Semiconductors. Online at: https://www.tf.uni-kiel.de/matwis/amat/semitech_en/kap_2/backbone/r2_3_1.html

[34] Woodall J. Us Davis University of California AKA the "Crystal Grower's Chart" online at: https://woodall.ece.ucdavis.edu/resources/

[35] Atef Y. Shenouda *, El Sayed M. El Sayed Electrodeposition, characterization and photoelectrochemical properties of CdSe and CdTe Central Metallurgical R & D Institute (CMRDI), Tebbin, P.O. Box: 87, Helwan, Egypt Received 8 April 2014; revised 5 June 2014; accepted 24 July 2014

[36] Anuradha Purohit, Subhash Chander, Satya Pal Nehra, Mahendra Singh Dhaka. Thickness Dependent Physical Properties of Thermally Evaporated Nanocrystalline CdSe Thin Films. Acta Metallurgica Sinica(English Letters), 2015, 28(10): 1299-1304

[37] Anuradha Purohit,S. Chander,S.P. Nehra,C. Lal,M.S Effect of thickness on structural, optical, electrical and morphological properties of nanocrystalline CdSe thin films for optoelectronic applications. Dhaka Optical Materials Elsevier September 2015

[38] S. Mahato, Nanda Shakti, and A.K. Kar,“Annealing temperature dependent structural and optical properties of electro deposited CdSe thin films”, Elsevier, Materials Science in Semiconductor Processing, Volume 39, November 2015

[39] H. METIN*, S. ERAT, M. ARIa, M. BOZOKLUa Characterization of CdSe films prepared by chemical bath deposition method OPTOELECTRONICS AND ADVANCED MATERIALS – RAPID COMMUNICATIONS Vol. 2, No. 2, February 2008, p. 92 – 98

[40] S:S Patil and P. H. Pawar, “Structural and optical studies of thermally evaporated CdSexTe1-x thin films” , Journal of chimical, Biological and Physical Science , section C, May-July, 2012, Vol2, No. 3, 1472 – 1484.

Chapter 6

Conclusions and Future Work

"Do not be afraid of being free thinkers. If you think strongly enough you will be forced by science to the belief in God, which is the foundation of all Religion. You will find science not antagonistic, but helpful to Religion."

Sir William Thomson, Lord Kelvin (1824-1907), Physics
Formulator of the First and Second Laws of Thermodynamics.

6.1 General Conclusions

In the present doctoral study, device structures were fabricated, using different techniques and materials. All the devices were electrical characterized using a Keithley Source meter switch system in darkness and under a light with an optical power source Pin = 100 mW/m^2.

Results are explained in chapter 4, where it is shown the feasibility of the inclusion of quantum wells using vacuum technologies as Thermal Evaporation and RF Sputter chambers.

A novel approach was done on the desing of a PV cell architecture where two very well known techniques were used (Chemical Bath deposition and RF Sputter) in combination in order to fabricate a device with better electrical properties and stability. Results show that in the novel proposed architecture FTO/CdS(CBD)/CdSe(CBD)/PbS(TE)/Ag not only the prevention of a decrease in Voc was achieved, but also an increase of the Voc itself from 0.111 V to 0.2165 V.

In the search to obtain the best of each of the properties of the semiconductors from the II-VI group, a well-known architecture of a PV cell (CdS-CdTe) has been taken and a top layer of PbS has been added as buffer layer by RF Sputering technique. In addition, different TCO´s (ITO, FTO and ZnO) have been tested comparing the electrical properties resulting from the use of each one of them. Devices with the configuration of ITO/CdS 250 nm/CdTe 1000 nm/ PbS 1000 nm/Ag did not generate any power at all, instead, those with FTO and ZnO did have a response, as shown in Fig. 4-15, where it is observed an average increment in Voc from 0.1 (FTO) V to 0.38 V (ZnO), as well as an increment in Jsc from 1.15 mA/cm2 to 37.32 mA/cm2 between the first to the second structure. Such increments represent power conversion efficiency (PCE) in the systems of 0.0468% to 4.98% respectively. Such increment in the PCE of both arrangements can be attributed to the ZnO layer. The highest Voc achieved was 0.42 V with a CdTe thickness of ~1000 nm, which is also the CdTe thickness where the tandem

cell was found to exhibit the best overall performance. For more information, results are summarized in Table 4-6

On the other hand, in order to enhance the Voc, an alternative strategy to the former architectures is proposed. In this novel structure, a CdSexTe1−x ultrathin film is deposited away from the P-N interface but within the P-type semiconducting layer, as shown in Fig 4-8 (c). Two photonic detectors were fabricated using thermal evaporation technique. The first device, a Glass/ITO/CdS/CdSe/Ag arrangement, was performed as a comparison device. In the second device, an ultrathin film of CdSe0.6Te0.4 was deposited some nanometers away from the depletion region of the first arrangement. I.e. buried certain distance away from CdS/CdSe interface within the CdSe layer, keeping the structure, Glass/CdS/CdSe/CdSe0.6Te0.4/CdSe/Ag.

Table 6-1: Summarized Electrical characterization results

Heterostructure	Voc (v)	Jsc (mA/cm²)
FTO-CdS(CBD) - PbS(TE)-Ag	0.111	-0.0008
FTO-CdS(CBD) - CdSe(CBD) - PbS(TE)-Ag	0.2165	-0.003
ITO-CdS-CdSe-Ag	0.58	14.6
ITO-CdS-CdSe-$CdSe_{0.6}Te_{0.4}$-CdSe-Ag	1.54	21.1
ITO-CdS(S) - CdTe(S)- PbS(S)-Ag	-	-
ZnO-CdS(S) - CdTe(S)- PbS(S)-Ag	0.38	37.32
FTO-CdS(S) - CdTe(S)- PbS(S)-Ag	0.10	1.15

This study, showed the best results achieved, where it is observed an increment in Voc from 0.58 V to 1.54 V, as well as an increment in Jsc from 14.68 mA/cm^2 to 21.11 mA/cm^2 between the conventional and the proposed structure. Such increments represent power conversion efficiency (PCE) in the systems of 3.1% to 11.6% respectively. Such increment in the PCE of the proposed structure can be attributed to the insertion of a $CdSe_{0.6}Te_{0.4}$ thin film within the depletion region of the p-type CdS and n-type CdSe interface.

The different results has demonstated that the combination of techniques and materials is feasible and, besides the obtained efficiencies, an increment in

Voc and Jsc are present, proofs that more work needs to be done. II-VI group semiconductor materials are very well-known promising materials, but they need to be examined with novel approaches to enhance their good properties, and achieve better PCE in PV devices. For more clarity in the overall results, Voc and Jcs are summarized in Table 6-1.

6.2 Future Work

6.2.1 Introduction

The greatest challenge in achieving temperatures below 10 kelvin in semiconductor materials through photoluminescence up conversion is that at these temperatures, in phonon-acoustic components predominate in semiconductors and their dispersion rate becomes comparable with the radioactive transition rate from band to band. This problem can be significantly alleviated by the use of quantum confinement systems, where the relaxation of the conservation of the wave vector in the confinement direction reduces the magnitude of the conductivity of the material almost three times its original value. Although previous studies have reported theoretical and experimental analyzes of optical cooling characteristics in coarse semiconductor materials, the electrons transition from band to the band due to photon absorption and emission under optical cooling conditions in confinement systems exhibiting quantum effects due to their nanometric scale dimensions have been practically not applied. In future work, a theoretical-practical investigation of the conditions for optical cooling in low dimension heterostructures of CdSe / $CdSe_xTe_{1-x}$ / CdSe of simple and multiple quantum well (MQW) needs to be carried out. In these structures, the carriers injected into the active region are limited to mechanically move in one dimension (1D). The effects of quantum charge confinement on the photon absorption and photoluminescence process were analyzed under cooling conditions. Even more important, the absorption and photoluminescence spectra of the CdS / $CdSe_xTe_{1-x}$ / CdSe heterostructure for cooling conditions were defined in terms of the thickness of the absorbent layer (active layer) and the number of quantum wells in the entire heterostructure.

Humanity's technological ability to produce, by laser cooling, samples of ultra-cold atoms (almost at the very limit of the coldest temperature allowed by the laws of physics) revolutionized experimental atomic physics, and allowed us to build powerful devices, from atomic clocks (which are the heart of the Global Positioning System (GPS)) to more experimental and entirely new ones, such as some of the parts that will be needed to make a quantum computer. The concept of laser cooling may sound impossible, because a laser beam tends to heat everything it touches, not cool it down. However, on an atomic scale, it is feasible to push atoms and molecules in the desired way using slight impacts produced by a constant stream of photons (light particles), emitted by a laser. Using laser beams to, for example, hit selected atoms from opposite directions; you can slow down their movements. Laser techniques of this type are known as laser cooling, because the temperature is a direct measure of the speeds of movement of a group of molecules or atoms. In this sense, reducing the movements of atoms to, for example, making them almost immobile is equivalent to lowering their temperatures to almost Absolute Zero (273 degrees Celsius below zero), the coldest temperature that can exist. However, current laser techniques that are commonly used to cool atoms from room temperature to very close to Absolute Zero are limited to atoms with a suitable electronic structure. As a result, only a small part of the atomic elements, along with a few diatomic molecules, have been cooled in this way. On the other hand, the greatest challenge in achieving temperatures below 10 kelvin in semiconductor materials through photoluminescence up conversion (optical cooling), is that at these temperatures, in the semiconductors, the phonon-acoustic components predominate and The scattering rate of these becomes comparable to the radioactive transition rate from band to band. This problem can be significantly alleviated by the use of quantum confinement systems, where the relaxation of the conservation of the wave vector in the confinement direction reduces the magnitude of the conductivity of the material almost three times its original value. Although previous studies have reported theoretical and experimental analyzes of optical cooling characteristics in coarse semiconductor materials, the transition from band to band electrons due to

absorption and emission of photons under conditions of optical cooling in confinement systems exhibit effects quantum due to their nanometric scale dimensions. These effects have not been fully analyzed in conventional theoretical studies.

Therefore, this work is justified by carrying out a theoretical-practical investigation of the optical cooling conditions in a low-dimension heterostructure with simple and multiple quantum wells (MQW). In these structures, the carriers injected into the active region are limited to mechanically move in one dimension (1D). Likewise, to analyze the effects of quantum charge confinement on the photon absorption and photoluminescence process under cooling conditions. Even more important, define the absorption and photoluminescence spectra of the heterostructure for cooling conditions in terms of the thickness of the absorbent layer (active layer) and the number of quantum wells in the complete heterostructure.

6.2.2 Overview

The term optical cooling "Optical Cooling" or laser cooling "Laser Cooling", which does not imply cooling of light or lasers, is used to describe the cooling of atoms or ions, by Opto-thermal effects, at extremely low temperatures. There are different methods of optical cooling of atoms or ions, for example, Doppler cooling [1], where the intensity of the incident light is the main source for the process of absorption and subsequent spontaneous emission of photons. The rate of these processes depends on the Doppler shift effect on the temperature of the atoms or ions. This method is limited in terms of the temperature achievable by the Doppler limit. Sisyphus cooling [2], which implies a polarization gradient for what is sometimes called a refrigerant polarization gradient, which allows temperatures below the Doppler limit to be obtained substantially.

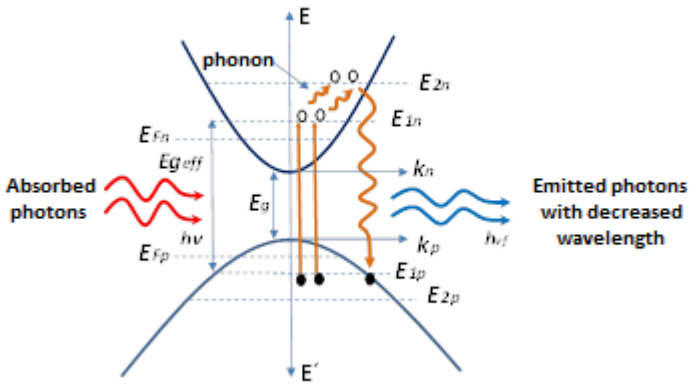

Fig. 6-1 Schematic diagram of the optical solid cooling cycle.

This area of science has progressed rapidly in the past three decades and has facilitated the observation of Bose-Einstein condensation and other related phenomena [3], [4]. It is surprising that it has been little more than half a century of having observed the Doppler cooling of atoms and more than thirty-five years before the invention of the laser, the German physicist Peter Pringsheim proposed the cooling of solids by fluorescence (up-conversion) [5]. Some materials have been shown to emit light at shorter wavelengths than those with which the material is illuminated due to thermal interactions (phonons) with the excited atoms, as shown in Fig. 6-1. Electrons in the valence band transition to the conduction band by absorbing a photon with hv energy from the incident light. The electrons in the conduction band undergo an energy exchange through inelastic collisions absorbing thermal vibrations from the material. After gaining energy in collisions, electrons in the conduction band decay to the valence band, emitting incoherent photons with decreased wavelength (incoherent blueshifted photon) with hvf energy which is generated through radioactive recombination dissipating heat from the material. As a result, the material is cooled by incident light [5].

This process was called anti-Stokes fluorescence, as opposed to Stokes fluorescence in which the emitted wavelength is greater than that absorbed. Since anti-Stokes fluorescence involves the emission of higher energy photons than those that were absorbed, net anti-Stokes fluorescence can cause the removal of thermal energy from the illuminated material and, as a consequence, it's cooling.

Of course, it is essential that quantum efficiency is high, and that almost all anti-Stokes fluorescence light can leave the material without being reabsorbed. Contrary to what happens in gases, where particles (molecules, atoms, ions, electrons, etc.) are in random motion, in solids, atoms do not have relative translational motion. In solids, thermal energy is largely found in the vibratory modes of the material's structural network (phonons). Solid laser cooling (also called laser cooling, optical cooling, or anti-Stokes fluorescence cooling) is similar to laser cooling of atoms and ions: photons on the red side of the spectrum are absorbed from a monochromatic source followed by anti-fluorescence Stokes of photons with blue shift with higher energy. These anti-Stokes photons remove the phonons from the material and consequently cool it.

6.2.3 Overall objective

The general objective of this thesis work is to carry out a theoretical-practical investigation of the optical cooling conditions in low-dimension heterostructure of CdSe / $CdSe_xTe_{1-x}$ / CdSe with simple and multiple quantum wells (MQW) considering the scoop that for these Carrier structures injected into the active region are limited to mechanically moving in one dimension (1D). Similarly, to analyze the effects of quantum charge confinement on photon absorption and photoluminescence under cooling conditions. As well as identifying and defining, in terms of the thickness of the absorbent layer (active layer) and the number of quantum wells in the complete heterostructure, the absorption and photoluminescence spectra of the CdS / CdTe heterostructure for cooling conditions.

6.2.4 Goals

To achieve the general objective of this thesis work, the following specific goals are proposed:

1. To propose a photon-absorbing heterostructure based on CdSe / $CdSe_xTe_{1-x}$ / CdSe with the capacity to obtain optical cooling using the solar radiation spectrum as an excitatory source.

2. Develop mathematical modeling of photon absorption and optical cooling phenomena in the proposed structure.

3. Carry out a comparative study of photon absorption and cooling capacity in the proposed structure using different moment selection criteria.

4. Define the absorption and photoluminescence spectra of the proposed heterostructure for optical cooling conditions in terms of the thickness of the absorbent layer (active layer) and the number of quantum wells in the complete heterostructure.

5. Define the optimal dimensioning of the active layer of the proposed structure, to obtain maximum photon absorption and optical cooling based on the spectrum of solar irradiation.

6. Manufacture the proposed structure using deposits by thermal evaporation and ion erosion (sputtering).

7. Correlate the theoretical results with the resulting practical results

6.2.5 Methodology

The methodology to be followed consists of two stages. The first stage, theoretical development, is based on the use of principles of optical cooling of solids and quantum physics for the development of mathematical modeling of phenomena that interrelate photon absorption and photoluminescence in the proposed structures. The photon absorption and the photoluminescence spectral density for the proposed heterostructures will be modeled using the theory supporting the deduction of equations (1) and (2) as described in the references [6, 7, 8 and 9].

$$\alpha(\nu) = \frac{1}{\nu_g}\left[\overline{B}(\nu)hT_{AB}(E) + \frac{1}{\tau_{loss}}\right],$$

$$R(\nu) = \frac{8\pi n^2 \nu^2}{c^2}\alpha(\nu)\left\{\frac{f_c(1-f_v)}{(f_v - f_c)}\right\}$$

Where equation (1) is the absorption coefficient and photoluminescence spectral density of the active layer of a multilayer structure with a quantum well. each of the components of these equations is clearly described in the references [6-9].

The second stage, practical implementation and characterization tests, is based on the fabrication of the structure shown in Fig. 6-2. For the fabrication, a TCO-coated soda-lime glass substrate will be used, after which the CdS / structure will be deposited. CdSe / $CdSe_xTe_{1-x}$ / CdSe using the techniques of Thermal Evaporation and Ionic Erosion (sputtering).

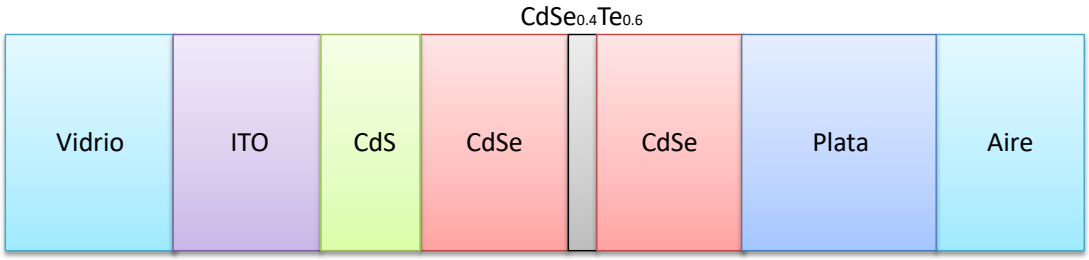

Fig. 6-2 Structure of a photovoltaic device that includes a CdSe / $CdSe_{0.4}Te_{0.6}$ / CdSe quantum well as a photoluminescent structure.

The structural, optical and electrical characterization of the heterostructure will be using techniques such as FT-IR, Raman, UV-vis spectroscopy, X-ray Photoelectron Spectrometer XPS, Scanning Electron Microscope, Ray diffraction X, ellipsometry and Filmetrics analyzer. Keithley multimeter, sources, etc. Later, for the thermal tests, a cryostat, a photoluminescence detector, an infrared camera for thermal mapping, among others, will be used.

6.2.6 Expected Results.

Among the expected results is the proposal of photon-absorbing heterostructures based on CdSe / $CdSe_xTe_{1-x}$ / CdSe with the capacity to obtain optical cooling using the solar radiation spectrum as an excitatory source. The development of mathematical modeling of the photon absorption and optical cooling phenomena in the proposed structure. The detailed description of the absorption and photoluminescence spectra of the proposed heterostructure for optical cooling conditions in terms of the thickness of the absorbent layer (active layer) and the number of quantum wells in the complete heterostructure. A methodology to define the optimal dimensioning of the active layer of the proposed structure. According to the present doctoral work, the fabrication of the proposed structure can be achieve by Thermal evaporation and RF sputtering techniques.

6.3 References

[1] T. W. Hänsch and A. L. Schawlow, “Cooling of gases by laser radiation,” Opt. Commun, vol. 13, pp. 68–69, 1975.

[2] J. Dalibard and C. Cohen-Tannoudji, “Dressed-atom approach to atomic motion in laser light: the dipole force revisited,” J. Opt. Soc. Am. B, vol. 2, no. 11, pp. 1707–1720, 1985.

[3] W. D. Chu, S. Cohen-Tannoudji, C. Philips, “for Development of methods to cool and trap atoms with laser light.,” Nobel Prize Phys., 1997.

[4] E. A. Cornel, W. Ketterle, and C. E. and Weiman, “for the achievement of Bose-Einstein condensation in dilute gases of alkali atoms, and for early fundamentals studies of the properties of the condensates.,” Nobel Prize Phys., 2001.

[5] P. Pringsheim, “‘Zwei Bemerkungen über dan Unterschied von Lumineszenz und Temperaturstrahlung,’” ZeitschriftPhysik, vol. 57, no. 11, pp. 739–746, 1929.

[6] Jose R. Villa-Angulo, Rafael Villa-Angulo and Carlos Villa-Angulo, “Photon Absorption Coefficient (α) for a Low-dimensional CdS/CdTe Absorber by a Partial k-selection Approach”, SPIE Journal of Nanophotonics, Vol. 61, No. 4, April (2012),

[7] Jose R. Villa-Angulo, Rafael Villa-Angulo, Karina Solorio-Ferrales, Silvia E. Ahumada-Valdez and Carlos Villa-Angulo, “Effect of effective mass mismatch in CdS/CdTe heterojunctions on the fundamental design parameters of nanophotonics devices”, SPIE Journal of Nanophotonics, Vol. 8, pp. 083096-1, Jan. (2014),

[8] J. Yao, W. Zheng, H. Opper, J. Cai, and G. W. Taylor, “Intersubband absorption in modulation doped heterostructures,” J. Appl. Phys., vol. 108, no. 1, p. 013104, 2010.

[9] G. W. Taylor, “Theory of operation of the quantum-well injection laser without k-selection,” J. Appl. Phys., vol. 70, no. 5, pp. 2508–2535, 1991.

[10] Julio C. Tarin-Cordero, Rafael Villa-Angulo, Jose. R. Villa-Angulo and Carlos Villa-Angulo, “Low-dimensional CdS/CdTe multiple quantum well heterstructure for optical refrigeration”, SPIE Journal of Nanophotonics, Vol. 9, pp. 093085-1, Mar. (2015),

Appendix 1

Code for calculating energy levels, quasi-fermis, absorption coefficient

```
clear; close all; clc
%Egb=input('Band gap barrera en el CdSe (Kg) conduccion:'); %capa Activa
1.84
Egb=1.84; %eV
disp('Band gap barrera en el CdSe (eV):');
disp(Egb);
%Egw=input('Band gap barrera en el CdSe0.4Te0.6 (eV) pozo:'); %capa
Activa 1.84
Egw=1.5; %eV
disp('Band gap activa:');
disp(Egw);
Lz=90*10^-9; %m
a=Lz/2; %m;
disp('Lz:');
disp(Lz);
deltaEc=0.6*(Egb-Egw)*1000; %meV
deltaEv=0.4*(Egb-Egw)*1000; %meV
mo= 0.91*10^-30; %Kg
eV=1.602*10^-19; %C
%Vo_c=204;
%Vo_v=136;
miew=0.175;     % mn masa efectiva del electron en el CdSe0.4Te0.6 (Kg)
pozo
mieb=0.130;     % masa efectiva del electron en el CdSe (Kg) conduccion
mihw=0.495;     % mp masa efectiva del hueco en el CdSe0.4Te0.6 (Kg) pozo
mihb=0.450;     % masa efectiva del hueco en el CdSe (Kg) conduccion
mew= miew*mo; %Kg
meb= mieb*mo; %Kg
mhw= mihw*mo; %Kg
mhb= mihb*mo; %Kg
Vo=deltaEc*eV;
htestada=1.05499*10^-34; %J.s
h=6.63*10^-34; %m2kgs-1
hcm=6.63*10^-30;                            % cm^2*kg/seg
disp('masa efectiva de electron en barrera:');
disp(mieb);
disp('masa efectiva de electron en pozo:');
disp(miew);
disp('masa efectiva del hueco en barrera:');
disp(mihb);
disp('masa efectiva del hueco en pozo:');
disp(mihw);

%%%%%%%%%%%%%%%%%%%%%%%%%%%%%%%%%%%%%%%%%%%%%%%%%%%%%%%%%%%%%%%%%%%%%%%%%%%%
%%%%%%%%%%
% PARA LA BANDA DE CONDUCCION OBTENIENDO EL VALOR DEL RADIO PARA
ELECTRONES EN V0 %
%%%%%%%%%%%%%%%%%%%%%%%%%%%%%%%%%%%%%%%%%%%%%%%%%%%%%%%%%%%%%%%%%%%%%%%%%%%%
%%%%%%%%%%
```

```
% LOS VALORES DE ENERGIA PUEDEN SER ENCONTRADOS CON LAS SIGUIENTES
ECUACIONES
KIIc= sqrt(((2*mew)/(htestada^2))*(1.602*10^-19)*(.001));
alfapreviac=sqrt(((2*mieb)*(0.91*10^-30)*(1.602*10^-
19)*(.001))/htestada^2);
Ecpar=[0:-10:-110];
f_Ecpar=(meb/mew)*KIIc*sqrt(Ecpar+deltaEc).*tan(KIIc*a*sqrt(Ecpar+deltaEc
));
Ecpar=[0:-10:-110]; alfac=alfapreviac*sqrt(-1*Ecpar);
Ecimpar=[0:-10:-110]; f_Ecimpar=(-
1*(meb/mew)*KIIc*sqrt(Ecimpar+deltaEc).*cot(KIIc*a*sqrt(Ecimpar+deltaEc))
);
Ecimpar=[0:-10:-110]; alfac=alfapreviac*sqrt(-1*Ecimpar);
display('se seleccionan las intercciones de forme alternada iniciando con
impares')
display('alimentar estos valores en seccion de calculo de nivles EC y
EV')
display ('intersecciones Nivel impar de energía en capa de condicción')
%plot(Ecimpar,alfac,Ecimpar,f_Ecimpar),title('Nivel impar de energía en
capa de Conducción'); grid()
[xint] = polyxpoly(Ecimpar,alfac,Ecimpar,f_Ecimpar)
display ('intersecciones Nivel par de energía en capa de condicción')
%plot(Ecpar,alfac,Ecpar,f_Ecpar),title('Nivel par de energía en capa de
Conducción'); grid()
[xint] = polyxpoly(Ecpar,alfac,Ecpar,f_Ecpar)

%%%%%%%%%%%%%%%%%%%%%%%%%%%%%%%%%%%%%%%%%%%%%%%%%%%%%%%%%%%%%%%%%%%%%%%%
%%%%%%%%
% PARA LA BANDA DE VALENCIA OBTENIENDO EL VALOR DEL RADIO PARA ELECTRONES
EN V0 %
%%%%%%%%%%%%%%%%%%%%%%%%%%%%%%%%%%%%%%%%%%%%%%%%%%%%%%%%%%%%%%%%%%%%%%%%
%%%%%%%%

% LOS VALORES DE ENERGIA PUEDEN SER ENCONTRADOS CON LAS SIGUIENTES
ECUACIONES
KIIv= sqrt(((2*mhw)/(htestada^2))*(1.602*10^-19)*(.001));
alfapreviav=sqrt(((2*mihb)*(0.91*10^-30)*(1.602*10^-
19)*(.001))/htestada^2);
Evpar=[0:-10:-250];
f_Evpar=(mhb/mhw)*KIIv*sqrt(Evpar+deltaEv).*tan(KIIv*a*sqrt(Evpar+deltaEv
));
Evpar=[0:-10:-250]; alfav=alfapreviav*sqrt(-1*Evpar);
Evimpar=[0:-10:-250]; f_Evimpar=(-
1*(mhb/mhw)*KIIv*sqrt(Evimpar+deltaEv).*cot(KIIv*a*sqrt(Evimpar+deltaEv))
);
Evimpar=[0:-10:-250]; alfav=alfapreviav*sqrt(-1*Evimpar);
display ('intersecciones Nivel impar de energía en capa de Valencia')
%plot(Evimpar,alfav,Evimpar,f_Evimpar),title('Nivel impar de energía en
capa de Valencia'); grid()
[xint] = polyxpoly(Evimpar,alfav,Evimpar,f_Evimpar)
display ('intersecciones Nivel par de energía en capa de Valencia')
%plot(Evpar,alfav,Evpar,f_Evpar),title('Nivel par de energía en capa de
Valencia'); grid()
[xint] = polyxpoly(Evpar,alfav,Evpar,f_Evpar)

%%%%%%%%%%%%%%%%%%%%%%%%%%%%%%%%%%%%%%%%%%%%%%%%%%%%%%%%%%%%%%%%%%%%%%%%
```

```
% CALCULO DE EC Y EV DE LOS PUNTOS DE INTERSECCION DE LAS GRAFICAS %
%%%%%%%%%%%%%%%%%%%%%%%%%%%%%%%%%%%%%%%%%%%%%%%%%%%%%%%%%%%%%%%%%%%%%%%
%de la interseccion de las graficas nivel impar de energia en capa
conduccion
Ec1=deltaEc-8.9606;
Ec3=deltaEc-35.0853;
Ec5=deltaEc-82.3248;
Ec7=deltaEc-105.2550;
%de la interseccion de las graficas nivel par de energia en capa
conduccion
Ec2=deltaEc-19.96;
Ec4=deltaEc-32.78;
Ec6=deltaEc-69.91;
Ec8=deltaEc-86.31;
Ec10=deltaEc-104.5;
%de la interseccion de las graficas nivel impar de energia en capa
valencia
Ev1=deltaEv-22.32;
Ev3=deltaEv-120.66;
%de la interseccion de las graficas nivel par de energia en capa valencia
Ev2=deltaEv-11.95;
fprintf (' \n el valor de deltaEc es: =%d meV\n el valor de Ec1 es:a =%d
meV\n el valor de Ec2 es:a =%d  meV\n el valor de Ec3 es:a =%d  meV\n el
valor de Ec4 es:a =%d  meV\n el valor de Ec5 es:a =%d  meV\n el valor de
Ec6 es:a =%d  meV\n el valor de Ec7 es:a =%d  meV\n el valor de Ec8 es:a
=%d  meV\n el valor de Ec10 es:a =%d
meV\n\n',deltaEc,Ec1,Ec2,Ec3,Ec4,Ec5,Ec6,Ec7,Ec8,Ec10);
fprintf (' \n el valor de deltaEv es: =%d meV\n el valor de Ev1 es:a =%d
meV\n el valor de Ev2 es:a =%d  meV\n el valor de Ev3 es:a =%d
meV\n\n',deltaEv,Ev1,Ev2,Ev3);

%%%%%%%%%%%%%%%%%%%%%%%%%%%%%%%%%%%%%%%%%%%%%%%%%%%%%%%%%%%%%%%%%%%%%%%
%%%%%%%%%%%%%%%% LONGITUD DE ONDA REAL %%%%%%%%%%%%%%%%%%
%%%%%%%%%%%%%%%%%%%%%%%%%%%%%%%%%%%%%%%%%%%%%%%%%%%%%%%%%%%%%%%%%%%%%%%

Longitudonda=0.825; %micrometros 825 nm
Eg_eV=1.24/Longitudonda; %eV
disp('frecuencia central de emisión asignada en micrómetros en:');
disp(Longitudonda)
longitudrealsist=(1.24/(Egw+(Ec1/1000)+(Ev1/1000)));
disp('frecuencia central de emisión real del sistema en micrómetros
en:');
disp(longitudrealsist)
if (longitudrealsist)>(673.9)
    disp('Esta por arriba de la longitud de absorción del CdSe (673.9nm),
por lo tanto satisface la expectativa de colocación del pozo cuántico')
%elseif (longitudrealsist)<(673.9)
    %disp('la frecuencia central de emisión es menor a la asignada.')
else
    disp('Esta por arriba de la longitud de absorción del CdSe (673.9nm),
por lo tanto satisface la expectativa de colocación del pozo cuántico')
end

%%%%%%%%%%%%%%%%%%%%%%%%%%%%%%%%%%%%%%%%%%%%%%%%%%%%%%%%%%%%%%%%%%%%%%%
%%%%%%%%%%%%%%%%%% CUASIFRMIS %%%%%%%%%%%%%%%%%%%%%%%%%%
%%%%%%%%%%%%%%%%%%%%%%%%%%%%%%%%%%%%%%%%%%%%%%%%%%%%%%%%%%%%%%%%%%%%%%%
```

```
Z= mhw/mew; %mp/mn
dumy=1000;
k=1.38*10^-23;
T=300; %K
q=1.602*10^-19;

%Algoritmo para Calcular Niveles QuasiFermis
close all
En2=Ec2/1000; %eV Declare cual es el Segundo Nivel Energetico de los
Electrones
En1=Ec1/1000; %eV Declare cual es el Primer Nivel Energetico de los
Electrones
Ep2=Ev2/1000; %eV Declare cual es el Segundo Nivel Energetico de los
Huecos
Ep1=Ev1/1000; %eV Declare cual es el Primer Nivel Energetico de los
Huecos
fprintf (' \n el valor de deltaEc es: =%d eV\n el valor de En1 es:a =%d
eV\n el valor de En2 es:a =%d  eV\n\n',deltaEc,En1,En2);
fprintf (' \n el valor de deltaEv es: =%d eV\n el valor de Ep1 es:a =%d
eV\n el valor de Ep2 es:a =%d  eV\n\n',deltaEv,Ep1,Ep2);
aa=En1:(En2-En1):En2; %aa=En1:(En2-En1)/1000:En2;
bb=Ep1:(Ep2-Ep1):Ep2; %bb=Ep1:(Ep2-Ep1)/1000:Ep2;

%Se asume kT/q igual a 0.026 para simplificacion de resultados.
izq= (1+exp(aa/0.026)).*(1+exp((aa-(deltaEc/1000))/0.026));
der= ((1+exp(bb/0.026)).^Z).*((1+exp((bb-(deltaEv/1000))/0.026)).^Z);
ii=1;
id=1;
 for (i=1:1:length(aa))

    for(j=1:1:length(bb))

    temp= abs(izq(1,i)-der(1,j));

    if (temp<dumy)

       dumy=temp;
       ii=i;
       id=j;

    end

    end

 end
      EFn=aa(ii)
      EFp=bb(id)
      EFm= (aa(1,ii)+bb(1,id))

%%%%%%%%%%%%%%%%%%%%%%%%%%%%%%%%%%%%%%%%%%%%%%%%%%%%%%%%%%%%%%%%%%%%%%%%%
%%%%%%%%%%
% CALCULO DE COEFICIENTE DE ABSORCION PARA POZO CUANTICO %
```

```
%%%%%%%%%%%%%%%%%%%%%%%%%%%%%%%%%%%%%%%%%%%%%%%%%%%%%%%%%%%%%%%%%%%%%%%%%%
%%%%%%%%%%

Ab=2*10^-10; %Es el coeficiente de Einstein cm^3/Seg
c=2.997*10^10;                   %  velocidad luz m/seg
ng=3.2;
Tauin=1*10^-12;                  % segundos
Tauloss=2.5*10^-11;
htestadam=1.054571*10^-34; %(m^2kg)/s
htcm=1.054571*10^-34; %(cm^2kg)/s
hm=6.63*10^-34;%(m^2kg)/s
hcm=6.63*10^-30;%(cm^2kg)/s
a=1/((mew/mhw)+1);
b=1-a;
Bv=(Ab*c*((longitudrealsist*10^-4)^2))/(8*3.1416);
hsv=(((htestadam)/Tauin)*(6.2415*10^18))*(100)^2; %meV Nivel de energías
hasta la cual puede absorberse mayor a EFn
Vg=c/ng;        % Velocidad de grupo de los fotones en el material cm/seg
hvtestada=(1.24-Egw-En1-Ep1); %hv-Eg-ein-e1p
D1nD1p=((mew*mhw)*(1*10^-8))/(3.1416^2*htestadam^4);
E=1.24/longitudrealsist;
%absorcion de fotones
S1=(Bv*hcm)*((D1nD1p*(1*10^-8))/(Lz*(1*10^-
8))^2)*((hsv/(6.2415*10^18))/2);
S2=(atan((2*b*hvtestada)/hsv*10^3*0.001)+atan((2*a*hvtestada)/hsv*10^3*0.
001));
CoefAbs=(1/Vg)*(S1*S2+(1/Tauloss));

%%%%%%%%%%%%%%%%%%%%%%%%%%%%%%%%%%%%%
hvtestada1=[0:0.01:850]; %[0:0.01:1] [680:0.01:790]
longonda1=1.24./(Egw+hvtestada1);
%S11=(((D1nD1p/((Lz)^2))*((hsv/2)))).*(1./(1+exp((EFn-
(a*hvtestada1))/0.026))).*(1./(1+exp((EFp-(b*hvtestada1))/0.026)));
S11=((D1nD1p*1.054571*10^-18*hcm*Bv)./((Lz)^2*2*Vg)).*(1./(1+exp((EFn-
(a*hvtestada1))/0.026))).*(1./(1+exp((EFp-(b*hvtestada1))/0.026)));
S22=(atan(2*b*hvtestada1/(hsv*10^3*0.001)))+(atan(2*a*hvtestada1/(hsv*10^
3*0.001)));
CoefAbs1=((S11.*S22)+(1/(Vg*Tauloss))); %/(1/10^8);
subplot(1,2,1),plot((Egw+hvtestada1),CoefAbs1),xlabel('Energía del foton
en eV'),ylabel('Coeficiente de absorcion a(v)(1/cm)')
subplot(1,2,2),plot(longonda1,CoefAbs1),xlabel('Longitud de onda del
foton en um'),ylabel('Coeficiente de absorcion a(v)  (1/cm)')
%%%%%%%R E S U L T A D O S %%%%%%%%%%%
fprintf(['Bv = ',num2str(Bv),' cm^6/s^2',...
'\nhsv Nivel de energías hasta la cual puede absorberse mayor a EFn =
',num2str(hsv),...
' meV \n'])
fprintf(['Vg Velocidad de grupo de los fotones en el material=
',num2str(Vg),...
' cm/seg\nDensidad de estados DnDp  = ',num2str(D1nD1p),...
' 1/J^2 * cm^4\nLongitud de onda efectiva  = ',num2str(longonda1(i)),...
' um\nSeccion1 = ',num2str(S11(i)),...
' \nSeccion 2 = ',num2str(S22(i)),...
' \nCoeficiente de absorcion a(v)  = ',num2str(CoefAbs1(i)),...
' (1/cm)\n'])
```

```
fprintf(['rango de Longitud de onda efectivas= '
,num2str(longonda1*1000), 'nm\n'])
fprintf(['rango de Coeficiente de absorcion a(v)= ' ,num2str(CoefAbs1),
'(1/cm)\n'])

%plot(Egw+hvtestada1,CoefAbs1)
%xlabel('Energía del Foton (eV)')
%ylabel('Coeficiente de absorción')
%grid on
%figure

%plot(longonda1,CoefAbs1)
%xlabel('Longitud de onda del Foton (micrometros)')
%ylabel('Coeficiente de absorción')
%grid on
```

Resultados

```
 el valor de deltaEc es: =2.040000e+02 meV
 el valor de Ec1 es:a =1.950394e+02  meV
 el valor de Ec2 es:a =1.840400e+02  meV
 el valor de Ec3 es:a =1.689147e+02  meV
 el valor de Ec4 es:a =1.712200e+02  meV
 el valor de Ec5 es:a =1.216752e+02  meV
 el valor de Ec6 es:a =1.340900e+02  meV
 el valor de Ec7 es:a =9.874500e+01  meV
 el valor de Ec8 es:a =1.176900e+02  meV
 el valor de Ec10 es:a =9.950000e+01  meV


 el valor de deltaEv es: =1.360000e+02 meV
 el valor de Ev1 es:a =1.136800e+02  meV
 el valor de Ev2 es:a =1.240500e+02  meV
 el valor de Ev3 es:a =1.534000e+01  meV

frecuencia central de emisión asignada en micrómetros en:
    0.8250

frecuencia central de emisión real del sistema en micrómetros
en:
    0.6856

Esta por arriba de la longitud de absorción del CdSe
(673.9nm), por lo tanto satisface la expectativa de
colocación del pozo cuántico

 el valor de deltaEc es: =2.040000e+02 eV
 el valor de En1 es:a =1.950394e-01  eV
```

```
 el valor de En2 es:a =1.840400e-01  eV


 el valor de deltaEv es: =1.360000e+02 eV
 el valor de Ep1 es:a =1.136800e-01  eV
 el valor de Ep2 es:a =1.240500e-01  eV


EFn =

    0.1950


EFp =

    0.1137


EFm =

    0.3087

Bv = 1.1209e-09 cm^6/s^2
hsv Nivel de energías hasta la cual puede absorberse mayor a
EFn = 6.5821 meV
Vg Velocidad de grupo de los fotones en el material=
9365625000 cm/seg
Densidad de estados DnDp  = 5.876530010066764e+65 1/J^2 *
cm^4
Longitud de onda efectiva  = 0.82119 um
Seccion1 = 306336139.6337
Seccion 2 = 0.0030385
Coeficiente de absorcion a(v)  = 930818.1898 (1/cm)
```

Appendix 2

Gt calculation code

```
clear; close all; clc

longitdonda=[350,360,370,380,390,400,410,420,430,440,450,460,470,480,490,
500,510,520,530,540,550,560,570,580,590,600,610,620,630,640,650,660,670,6
80,690,700,710,720,730,740,750,760,770,780,790,800];
nito = [2.2106, 2.1904, 2.1708, 2.1516, 2.1331, 2.1152, 2.098,
2.0815,2.0657, 2.0505, 2.036, 2.0221, 2.0088, 1.9961, 1.9839, 1.9723,
1.9613,1.9507, 1.9405, 1.9308, 1.9216, 1.9127, 1.9042, 1.8961, 1.8883,
1.8808,1.8737, 1.8668, 1.8602, 1.8539, 1.8478, 1.842, 1.8364, 1.831,
1.8259,1.8209, 1.8161, 1.8115, 1.807, 1.8028, 1.7986, 1.7946, 1.7908,
1.7871,1.7835, 1.7801 ]';
kito = [0.05851254, 0.05400554, 0.05037373, 0.04748415,
0.04522533,0.04350352, 0.04223955, 0.04136638,0.04082706, 0.04057307,
0.04056298,0.0407613, 0.04113761, 0.04166571, 0.04232306, 0.04309022,
0.04395034,0.04488888, 0.04589323, 0.04695242,0.04805696, 0.04919859,
0.05037013,0.05156533, 0.05277875, 0.05400567, 0.05524196, 0.05648406,
0.05772886,0.05897364, 0.06021609, 0.06145417, 0.06268614, 0.06391049,
0.06512594,0.06633137, 0.06752584, 0.06870857, 0.06987888, 0.07103622,
0.07218014,0.07331026, 0.07442628, 0.07552799, 0.07661521, 0.07768784 ]';
nCdS = [ 2.5220, 2.5155, 2.5105, 2.5084, 2.5076, 2.5097, 2.5113, 2.5164,
2.5229, 2.5332, 2.5430, 2.5620, 2.5817, 2.6229, 2.6114, 2.6797, 2.6115,
2.6079, 2.5537, 2.5236,2.4921, 2.4715, 2.4571, 2.44, 2.4253, 2.4126,
2.4004,2.3940, 2.3860, 2.3774, 2.3718, 2.3645, 2.3578, 2.3574,2.3475,
2.3407, 2.3378, 2.3344, 2.3299, 2.3257, 2.3223,2.3197, 2.3161, 2.3183,
2.3105, 2.3097]';
kCdS = [ 0.3664, 0.3614, 0.3554, 0.3493, 0.3449, 0.3368,0.3342, 0.3278,
0.3223, 0.3158, 0.3110, 0.3037, 0.2968,0.2756, 0.2316, 0.1476, 0.0861,
0.0286, 0.0062, 0.0016,0.0001, 0.0000, 0.0000, 0.00, 0.0000, 0.0000,
0.0000,0.0000, 0.0000, 0.0000, 0.0000, 0.0000, 0.0000, 0.0000, 0.0000,
0.0000, 0.0000, 0.0000, 0.0000, 0.0000, 0.0000,0.0000, 0.0000, 0.0000,
0.0000, 0.0000]';
nCdSe = [ 2.767, 2.765, 2.763, 2.724, 2.762, 2.762,2.764, 2.698, 2.764,
2.696, 2.773, 2.694, 2.785,2.703, 2.796, 2.708, 2.708, 2.802, 2.812,
2.728,2.829, 2.829, 2.760, 2.853, 2.866, 2.758, 2.853,2.837, 2.740,
2.733, 2.834, 2.733, 2.739, 2.862,2.755, 2.797, 2.812, 2.856, 2.856,
2.821, 2.761,2.660, 2.721, 2.691, 2.673, 2.635]';
kCdSe = [ 0.850, 0.817, 0.781, 0.682, 0.731, 0.709,0.688, 0.602, 0.649,
0.566, 0.619, 0.546, 0.583,0.523, 0.551, 0.496, 0.496, 0.524, 0.506,
0.478,0.482, 0.482, 0.481, 0.440, 0.402, 0.427, 0.344,0.311, 0.275,
0.257, 0.268, 0.242, 0.247, 0.270,0.231, 0.230, 0.230, 0.162, -0.0001, -
0.0001, -0.0001,-0.0001, -0.0001, -0.0001, -0.0001, -0.0001]';
nCdSe04Te06  = [ 0.8, 0.823, 0.846, 0.869, 0.891, 0.82, 0.841, 0.861,
0.882, 0.902, 1.125, 1.150, 1.175, 1.200, 1.225, 1.25, 1.275, 1.300,
1.325, 1.350, 1.4, 1.425, 1.451, 1.476, 1.502, 1.5, 1.525, 1.550, 1.575,
1.600, 1.562, 1.586, 1.610, 1.634, 1.658, 1.593, 1.616, 1.639, 1.661,
1.684, 1.687, 1.709, 1.732, 1.754, 1.777, 1.8]';
kCdSe04Te06 = [ 0.5, 0.514, 0.529, 0.543, 0.557, 0.55, 0.564, 0.578,
0.591, 0.605, 0.41, 0.419, 0.428, 0.437, 0.446, 0.35, 0.357, 0.364,
0.371, 0.378, 0.3, 0.305, 0.311, 0.316, 0.322, 0.25, 0.254, 0.258, 0.263,
0.267, 0.225, 0.228, 0.232, 0.235, 0.239, 0.2, 0.203, 0.206, 0.209,
0.211, 0.15, 0.152, 0.154, 0.156, 0.158, 0.1]';
```

```
nAg =
[0.11436,0.0870299,0.066912,0.052206,0.05,0.05,0.05,0.046105,0.040291,0.0
4,0.04,0.044439,0.049317,0.05,0.05,0.05,0.05,0.05,0.053285,0.056895,0.059
582,0.056597,0.053612,0.050627,0.052277,0.055159,0.05804,0.059251,0.05690
9,0.054567,0.052225,0.049889,0.047667,0.045444,0.043222,0.041,0.038932,0.
03699,0.035049,0.033107,0.031165,0.030614,0.032151,0.033687,0.035223,0.03
6759]';
kAg =
[1.3196,1.5198,1.689,1.8412,1.9741,2.1035,2.2325,2.3478,2.4566,2.5528,2.6
484,2.7511,2.8545,2.9476,3.0391,3.1309,3.2233,3.3157,3.4101,3.5074,3.5974
,3.6786,3.7598,3.8409,3.9249,4.0097,4.0944,4.1768,4.2543,4.3318,4.4094,4.
4869,4.5658,4.6447,4.7236,4.8025,4.8811,4.9596,5.038,5.1165,5.1949,5.2718
,5.3463,5.4208,5.4953,5.5698]';
nAire = 1;
kAire = 1i*0;
Ict = [ 0.32913, 0.3924, 0.51666, 0.49751, 0.58457, 0.83989,0.8091,
0.88467, 0.70134, 1.0993, 1.2881, 1.2791, 1.2749,1.3825, 1.3968, 1.3391,
1.3497, 1.3349, 1.3598, 1.3096,1.3648, 1.3885, 1.324, 1.3455, 1.2316,
1.3278, 1.3237,1.3299, 1.2589, 1.2962, 1.2299, 1.2668, 1.2853,
1.265,1.0746, 1.1636, 1.1954, 0.8994, 1.0294, 1.1119, 1.1273,0.24716,
1.0646, 1.0687, 1.0045, 0.98859]'; %(W(m^-2)(nm^-1))
Ic = Ict*0.8;

dito = 200;
%dCdS =100; %ventana
dCdS=input('ancho de la ventana (CdS-p) en nm:'); %capa Activa
%dCdSe =123; %capa Activa
dCdSe=input('ancho de capa activa (CdSe-N) en nm:'); %capa Activa
%dCdSe04Te06=input('ancho de pozo cuantico (CdSe0.4Te.06) en nm:'); %capa
Activa
dCdSe04Te06=9;
dAg = 10000;
pi=3.14159265359;
E=zeros(46,dCdSe04Te06);
Q=zeros(46,dCdSe04Te06);
G=zeros(46,dCdSe04Te06);

x=1;
for ok=1:1:46 %Para longitudes de onda
    n1=(nito(ok) + (kito(ok)*1i));
    n2=(nCdS(ok) + (kCdS(ok)*1i));
    n3=(nCdSe(ok) + kCdSe(ok)*1i);
    n4=(nCdSe04Te06(ok) + kCdSe04Te06(ok)*1i);
    n5=(nAg(ok) + kAg(ok)*1i);
    %Interface 1
    ritoCdS =(n2-n1)/(n2+n1);
    titoCdS =1+ ritoCdS;
    IitoCdS =(1/ titoCdS)*[1 ritoCdS; ritoCdS 1];
    %Interface 2
    rCdSCdSe =(n3-n2)/(n3+n2);
    tCdSCdSe =1+rCdSCdSe;
    ICdSCdSe =(1/tCdSCdSe)*[1 rCdSCdSe;rCdSCdSe 1];
    %Interface 3
    rCdSeCdSe04Te06 =(n4-n3)/(n4+n3);
    tCdSeCdSe04Te06 =1+rCdSeCdSe04Te06;
```

```
    ICdSeCdSe04Te06 =(1/tCdSeCdSe04Te06)*[1
rCdSeCdSe04Te06;rCdSeCdSe04Te06 1];
    %Interface 4
    rCdSe04Te06CdSe =(n3-n4)/(n3+n4);
    tCdSe04Te06CdSe =1+rCdSe04Te06CdSe;
    ICdSe04Te06CdSe =(1/tCdSe04Te06CdSe)*[1
rCdSe04Te06CdSe;rCdSe04Te06CdSe 1];
    %Interface 5
    rCdSeAg =(n5-n3)/(n5+n3);
    tCdSeAg =1+rCdSeAg;
    ICdSeAg =(1/tCdSeAg)*[1 rCdSeAg;rCdSeAg 1];
    %Matriz de propagacion libre
    %Propagacion1 (ITO)
     betaito=(((2*pi*dito)/longitdonda(ok))*n1*(cos(0)));
    Pito=[exp(1i*betaito) 0;0 exp(-1i*betaito)];
    %Propagacion2 (CdS)
    betaCdS=(((2*pi*dCdS)/longitdonda(ok))*n2*(cos(0)));
    PCdS=[exp(1i*betaCdS) 0;0 exp(-1i*betaCdS)];
     %Propagacion3y5 (CdSe)
    betaCdSe=(((2*pi)/ longitdonda(ok))*n3*(cos(0)));
    PCdSe=[exp(1i*betaCdSe) 0;0 exp(-1i*betaCdSe)];
     %Propagacion4 (CdSe04Te06)
    betaCdSe04Te06=(((2*pi)/ longitdonda(ok))*n4*(cos(0)));
    PCdSe04Te06=[exp(1i*betaCdSe04Te06) 0;0 exp(-1i*betaCdSe04Te06)];
    %Propagacion6 (Ag)
    betaAg =(((2*pi*dAg)/ longitdonda(ok))*n5*(cos(0)));
    PAg=[exp(1i*betaAg) 0;0 exp(-1i*betaAg)];

Mpj=IitoCdS*Pito*ICdSCdSe*PCdS*ICdSeCdSe04Te06*PCdSe; %matriz prima en j
Mbpj=ICdSe04Te06CdSe*PCdSe*ICdSeAg*PAg; %matriz biprima en j
tpj=1/Mpj(1,1);  %coeficiente de transmisión
rpjn=-Mpj(1,2)/Mpj(1,1);%coeficiente de reflexión negativo
rbpj=Mbpj(2,1)/Mbpj(1,1);
tjpos=tpj/(1-rpjn*(rbpj*exp(1i*2*betaCdSe))); %coeficiente de transmisión
positivo
alfa=(4*pi*kCdSe04Te06(ok))/longitdonda(ok);%coeficiente de absorcion

    for x=1:1:dCdSe04Te06 %Para espesor de capa activa

E(ok,x)=abs(tjpos*((exp(1i*betaCdSe04Te06*x)+(rbpj+exp(1i*betaCdSe04Te06*
(2*(dCdSe04Te06-x))))))*(Ict(ok)*0.8)); %campo electrico para una forma
de onda
       %E(lng,x)=abs(tp*((exp(1i*bj*x)+(rjpp*exp(1i*bj*(2*(d-
x))))))*Ic(lng)*(0.8));
        E(ok,x);
        Q(ok,x)=(1/2)*(3*10^8)*(8.85*10^-
12)*alfa*nCdSe04Te06(ok)*E(ok,x)^2;
        %Q(lng,x)=(1/2)*(3*10^8)*(8.85*10^-12)*aj*CdSen(lng)*E(lng,x)^2;
        Q(ok,x);
        G(ok,x)=( longitdonda(ok)*Q(ok,x))/((6.62606957*10^-
34)*(3*10^8));
        G(ok,x);
    end
end

SE=sum(E);%Sumatoria de todos los valores de matriz E.
```

```
SQ=sum(Q);%Sumatoria de todos los valores de matriz Q
SG=sum(G);%Sumatoria de todos los valores de la matriz G
Gt=sum(SG)%Suma total Taza de Generacion de Excitones.

z=1:1:dCdSe;
lambdamesh = longitdonda'*ones(1,length(z));
zmesh = ones(length(longitdonda),1)*z;

%%%%%%P O I S S O N%%%%%%%%%%%%%%
Gl=Gt; %m^-3/s,taza de generacion de excitones 6.5558*10^27
T=300; %kelvin
q=1.6*10^-19; %eV
k=8.617*10^-5; %constante de Boltzman
kT=0.0258;
eo=8.854*10^-14;
mo=9.1039*10^-31; %masa del electron
Vpoisson=600; %mV, voltaje de poisson propuesto
deltaVpoisson=100;

%Información del material tipo P (CdSe)
Na=1*10^15; %cm^-3 1*10^20
Dp=15.25; %cm^2/s, constante de difusión 12
tp=16; %s, tiempo de vida  -----
        %tp= 1.5; % *10^(-8)s tiempo de recombinacion de cargas en CdSe
CELDAS FOTOVOLTAICAS EN GENERACION DISTRIBUIDA ISIDRO ELVIS PEREDA SOTO
         %tp = 5; % us tiempo de recombinacion de cargas en CdSe
niPCdSe=7.07*10^3; %cm^-3, concentración intrinseca cdse
                %niPCdSe = 6*10^13;  %cm ^-3 concentracion intrinseca de
cargas en CdSe subvolumen B II-VI submagnetic compounds springer pdf
ep=10.2; %constante dielectrica
Egp=1.74; %eV,bandgap
mep=0.13; %masa del electron
mhp=0.45; %masa del hueco
mh=[ ];

%Información del material tipo n+ (CdS) mayormente dopado
Nd=5*10^15; %cm^-3 5*10^23
Dn=1.4; %cm^2/s, constante de difusión---
        %Dn=9; %cm^2/s, Coeficiente de difusión de cargas minoritarias
CcS Solar cells pag 74 materials and processing table 4.1
        %Dn=36.4; %cm^2/s, Coeficiente de difusión de cargas minoritarias
CcS Solar cells pag 74 materials and processing table 4.1
tn=1; %s, tiempo de vida   ----
        %tn = 2; % us tiempo de recombinacion de cargas en CdS
ninCdS=1.6*10^10; %cm^-3, concentración intrinseca cds
                %niCdS = 1.9*10^19; % cm ^-3 concentracion intrinseca de
cargas en CdS en nhttp://www.pveducation.org/pvcdrom/materials/CdS
en=8.9; %constante dielectrica
Egn=2.42; %eV,bandgap
men=0.17; %masa del electron
mhn=0.70; %masa del hueco
me=[ ];
Lp=sqrt(Dp*tp*10^-7); %cm, distancia de difusión de cargas
Ln=sqrt(Dn*tn*10^-9); %cm, distancia de difusión de cargas
npo=(niPCdSe^2)/(Na); %concentración de cargas minoritarias en equilibrio
pno=(ninCdS^2)/(Nd); %concentración de cargas minoritarias en equilibrio
```

```
i=1;

while deltaVpoisson > 1

    xp=(((2*ep*eo*Vpoisson*10^-3)/(q*Na*Nd*(Nd+(ep/en)*Na)))^(1/2))*Nd;
%cm
    xn=(xp/Nd)*Na; %cm
    w=xp+xn; %cm

    p=pno+pno*(exp((Vpoisson*10^-3)/kT)-1)*exp(xn/Lp)+(Gl*10^-6)*tp*10^-
7; %concentración de cargas en equilibrio
    n=npo+npo*(exp((Vpoisson*10^-3)/kT)-1)*exp(xp/Ln)+(Gl*10^-6)*tn*10^-
9; %concentración de cargas en equilibrio

    deltaEc=0.6*(Egn-Egp);
    Nv=(2.51*10^19)*(((mhp*mo)/mo)*(T/300))^(3/2);
    FpEcp=-kT*log(p/Nv);
    Nc=(2.51*10^19)*(((men*mo)/mo)*(T/300))^(3/2);
    FcnFn=-kT*log(n/Nc);

    Vo=(Egp+deltaEc-FpEcp-FcnFn);
    deltaVpoisson=Vo-(Vpoisson*10^-3);

    Vpoisson=(Vpoisson)+deltaVpoisson;
    mh(i)=p;
    me(i)=n;
    i=i+1;
end

%deltap = mh(i-1) - mh(i-2);%Calculo de la diferencia de concentraciones
p
%deltan = me(i-1) - me(i-2);%Calculo de la diferencia de concentraciones
n
%dcon = (abs(deltan)+abs(deltap))/(mh(i-1)+me(i-1));

cuasiv=sprintf('FpEcp=-kT*log(p/Nv)= %s eV',FpEcp);
disp(cuasiv)
cuasic=sprintf('FcnFn=-kT*log(n/Nc)= %s eV',FcnFn);
disp(cuasic)

%%%%%%%% C A R A C T E R I Z A C I O N %%%%%%%%%%%%

npoc=Na/(niPCdSe^2) %concentración de cargas minoritarias en equilibrio
pnoc=Nd/(ninCdS^2) %concentración de cargas minoritarias en equilibrio.

Voc=(0.0258)*log((((q*Gt*10^-
6)*(Lp+Ln))/(q*(((Dp/Lp)*(pnoc))+((Dn/Ln)*(npoc)))))+1) %Voltaje Circuito
Abierto, V
Jsc=q*(Gl*10^-6)*(Lp+Ln) %Corriente Corto Circuito, A
V=0:0.0001:Voc;
J=(((Dp/Lp)*(pnoc*q))+((Dn/Ln)*(npoc*q)))*(exp(V/0.0258)-1)-Jsc;
%Densidad de Corriente, A/cm^2

 plot(V,-J) %Grafica V vs J invertida
```

```
grid on
%Title('Grafica J-V')
xlabel('Voltaje en Volts')
ylabel('Densidad de Corriente en A/cm^2')

hold on
JP=abs(V.*J); %Potencia W/cm^2
x=find(JP==max(JP));
JPmax=JP(x)
Vmax=V(x)
Jmax=-J(x)

plot([0 V(x)],[-J(x) -J(x)],'r:+')
plot([V(x) V(x)],[0 -J(x)],'r:+')
Potinc = 0.09; %900/1*10^4; %Eficiencia de conversión de potencia
FF=(V(x)*-J(x))/(Voc*Jsc)
eficiencia=(Vmax*Jmax)/Potinc
Imaxdeseada=0.05 %A

L = 100;    %100 micrometros a  0.01cm % 25 mm a cm
porcentaje=0;
W=0;
if W<L
porcentaje=porcentaje+0.00045;
W=((porcentaje*Imaxdeseada)/(L*(Jmax*10^-8)));  %ancho, cm a um
end
A=((W)*(L)); %area transversal, cm^2 a um^2
Imax=(Jmax*10^-8)*(A); %Coriente maxima, A
Rmax=Vmax/Imax; %Resistencia, ohms
Pmax=(JPmax*10^-8)*(A); %Potencia maxima

%eficiencia=(Vmax*Jmax)/Potinc;

%%%%%%%R E S U L T A D O S %%%%%%%%%%
fprintf(['Potencia Máxima Pmax = ',num2str(JP(i)*W*L),' W\n',...
'\nVoltaje Máximo = ',num2str(V(i)),' V\nDensidad de Corriente corto
circuito = ',...
num2str(abs(J(i))),' A/cm2\n'])
fprintf(['ancho W %% = ',num2str(W),...
' micrometro\nlargo L  = ',num2str(L),...
' micrometro\nArea A  = ',num2str(A),...
' um^2\nResistencia Máxima Rmax = ',num2str(Rmax),...
' Ohms\nDensidad corriente Máxima Jmax = ',num2str(Jmax),...
' A/cm^2\nCorriente Máxima Deseada = ',num2str(Imaxdeseada*10^3),...
' mA\nCorriente Máxima del dispositivo Imax = ',num2str(Imax),...
' A\nVoltaje circuito abierto Voc = ',num2str(Voc),...
' mA\nFactor de llenado FF = ',num2str(FF),...
' \nEficiencia de Conversión de Potencia = ',num2str(eficiencia),'\n'])
%figure(2)
%clf
%plot(V,-I,'LineWidth',2)
%grid
%xlabel('Voltaje')
%ylabel('Corriente en A')
%hold on
%plot([0 V(i)],[-I(i) -I(i)],'k--')
```

```
%plot([V(i) V(i)],[0 -I(i)],'k--')
%text(V(i),-I(i),' Pmax')

%figure(3)
%subplot(2,2,1), plot(SE),xlabel('Profundidad de la capa
activa,d(nm)'),ylabel('Campo eléctrico, E(V/m^2)'); grid() %Grafica 2D de
todas las longitudes de onda)
%subplot(2,2,2), surf(lambdamesh,zmesh,E),ylabel('Profundidad capa
activa,d(nm)'),zlabel('Campo eléctrico, E(V/m^2)'),xlabel('Longitud de
onda,lambda (nm)'); grid()
%subplot(2,2,3), plot(SQ),xlabel('Profundidad de la capa
activa,d(nm)'),ylabel('Qj,Energía promedio disipada Q (W*m^-2)'); grid()
%Grafica 2D de todas las longitudes de onda)
%subplot(2,2,4), surf(lambdamesh,zmesh,Q),ylabel('Profundidad capa
activa,d(nm)'),zlabel('Qj,Energía promedio disipada Q (W*m^-
2)'),xlabel('Longitud de onda,lambda (nm)'); grid()

%figure(4)
%subplot(2,2,1), plot(SG),xlabel('Profundidad de la capa
activa,d(nm)'),ylabel('Gj,Taza de Generación de Excitones,(m^-3 s^-1)');
grid() %Grafica 2D de todas las longitudes de onda)
%subplot(2,2,2), surf(lambdamesh,zmesh,G),ylabel('Profundidad capa
activa,d(nm)'),zlabel('Gj,Taza de Generacion de Excitones (cm^-3 s^-
1'),xlabel('Longitud de onda,lambda (nm)'); grid()

ite=sprintf('\nCantidad de iteraciones realizadas:%d',i);
disp(ite)
lim=sprintf('Limite de la zona de agotamiento Xp=%s cm    Xn= %s cm
XW=%s cm',xp,xn,w);
disp(lim)
con=sprintf('Concentración de cargas en x=0, Pn(x)=%s cm^-3     np(x)=%s
cm^-3',p,n);
disp(con)
poi=sprintf('Vpoisson en la región n y P: %s mV',Vpoisson);
disp(poi)
exc=sprintf('Generacion de excitones:%G',Gt);
disp(exc)
vpoi=sprintf('Vo= %s V',Vo);
disp(vpoi)
fprintf (' \n espesor de ITO =%d nm\n espesor CdS ventana =%d nm\n
espesor CdSe capa activa =%d nm\n',dito,dCdS,dCdSe);
```

resultados

```
FpEcp=-kT*log(p/Nv)= 2.263469e-01 eV
FcnFn=-kT*log(n/Nc)= 3.996742e-01 eV

npoc =

   2.0006e+07
```

```
pnoc =

   1.9531e-05

Voc =

    0.3767

Jsc =

    0.2622

JPmax =

    0.0752

Vmax =

    0.3104

Jmax =

    0.2421

FF =

    0.7609

eficiencia =

    0.8350

Imaxdeseada =

    0.0500

Potencia Máxima Pmax = 0.24369 W

Voltaje Máximo = 0.0001 V
```

```
Densidad de Corriente corto circuito = 0.26223 A/cm2
ancho W % = 92.9294 micrometro
largo L  = 100 micrometro
Area A  = 9292.9359 um^2
Resistencia Máxima Rmax = 13795.5556 Ohms
Densidad corriente Máxima Jmax = 0.24212 A/cm^2
Corriente Máxima Deseada = 50 mA
Corriente Máxima del dispositivo Imax = 2.25e-05 A
Voltaje circuito abierto Voc = 0.37666 mA
Factor de llenado FF = 0.7609
Eficiencia de Conversión de Potencia = 0.83504

Cantidad de iteraciones realizadas:2
Limite de la zona de agotamiento Xp=7.423126e-05 cm    Xn=
1.484625e-05 cm   XW=8.907751e-05 cm
Concentración de cargas en x=0, Pn(x)=1.173189e+15 cm^-3
np(x)=3.292941e+11 cm^-3
Vpoisson en la región n y P: 6.009220e+02 mV
Generacion de excitones:3.29294E+26
Vo= 1.521979e+00 V

 espesor de ITO =200 nm
 espesor CdS ventana =200 nm
 espesor CdSe capa activa =10000 nm
```

Appendix 3

GQW calculation code

```
clear; close all; clc

longitdonda=[680,690,700,710,720,730,740,750,760,770,780,790,800];
nito = [1.831, 1.8259,1.8209, 1.8161, 1.8115, 1.807, 1.8028, 1.7986,
1.7946, 1.7908, 1.7871,1.7835, 1.7801 ]';
kito = [0.06391049, 0.06512594,0.06633137, 0.06752584, 0.06870857,
0.06987888, 0.07103622, 0.07218014,0.07331026, 0.07442628, 0.07552799,
0.07661521, 0.07768784 ]';
nCdS = [ 2.3574,2.3475, 2.3407, 2.3378, 2.3344, 2.3299, 2.3257,
2.3223,2.3197, 2.3161, 2.3183, 2.3105, 2.3097]';
kCdS = [ 0.0000, 0.0000, 0.0000, 0.0000, 0.0000, 0.0000, 0.0000,
0.0000,0.0000, 0.0000, 0.0000, 0.0000, 0.0000]';
nCdSe = [ 2.862,2.755, 2.797, 2.812, 2.856, 2.856, 2.821, 2.761,2.660,
2.721, 2.691, 2.673, 2.635]';
kCdSe = [ 0.270,0.231, 0.230, 0.230, 0.162, -0.0001, -0.0001, -0.0001,-
0.0001, -0.0001, -0.0001, -0.0001, -0.0001]';
nCdSe04Te06  = [1.634, 1.658, 1.593, 1.616, 1.639, 1.661, 1.684, 1.687,
1.709, 1.732, 1.754, 1.777, 1.8]';
kCdSe04Te06 = [0.235, 0.239, 0.2, 0.203, 0.206, 0.209, 0.211, 0.15,
0.152, 0.154, 0.156, 0.158, 0.1]';
nAg =
[0.045444,0.043222,0.041,0.038932,0.03699,0.035049,0.033107,0.031165,0.03
0614,0.032151,0.033687,0.035223,0.036759]';
kAg =
[4.6447,4.7236,4.8025,4.8811,4.9596,5.038,5.1165,5.1949,5.2718,5.3463,5.4
208,5.4953,5.5698]';
nAire = 1;
kAire = 1i*0;
Ict = [1.265,1.0746, 1.1636, 1.1954, 0.8994, 1.0294, 1.1119,
1.1273,0.24716, 1.0646, 1.0687, 1.0045, 0.98859]'; %(W(m^-2)(nm^-1))
Ic = Ict*0.8;

dito = 200;
%dCdS =100; %ventana
dCdS=input('ancho de la ventana (CdS-p) en nm:'); %capa Activa
%dCdSe =123; %capa Activa
dCdSe=input('ancho de capa activa (CdSe-N) en nm:'); %capa Activa
dCdSe04Te06=input('ancho de pozo cuantico (CdSe0.4Te.06) en nm:'); %capa
Activa
dAg = 10000;
pi=3.14159265359;
E=zeros(13,dCdSe04Te06);
Q=zeros(13,dCdSe04Te06);
G=zeros(13,dCdSe04Te06);

x=1;
for ok=1:1:13 %Para longitudes de onda
    n1=(nito(ok) + (kito(ok)*1i));
    n2=(nCdS(ok) + (kCdS(ok)*1i));
    n3=(nCdSe(ok) + kCdSe(ok)*1i);
```

```
    n4=(nCdSe04Te06(ok) + kCdSe04Te06(ok)*1i);
    n5=(nAg(ok) + kAg(ok)*1i);
    %Interface 1
    ritoCdS =(n2-n1)/(n2+n1);
    titoCdS =1+ ritoCdS;
    IitoCdS =(1/ titoCdS)*[1 ritoCdS; ritoCdS 1];
    %Interface 2
    rCdSCdSe =(n3-n2)/(n3+n2);
    tCdSCdSe =1+rCdSCdSe;
    ICdSCdSe =(1/tCdSCdSe)*[1 rCdSCdSe;rCdSCdSe 1];
    %Interface 3
    rCdSeCdSe04Te06 =(n4-n3)/(n4+n3);
    tCdSeCdSe04Te06 =1+rCdSeCdSe04Te06;
    ICdSeCdSe04Te06 =(1/tCdSeCdSe04Te06)*[1
rCdSeCdSe04Te06;rCdSeCdSe04Te06 1];
    %Interface 4
    rCdSe04Te06CdSe =(n3-n4)/(n3+n4);
    tCdSe04Te06CdSe =1+rCdSe04Te06CdSe;
    ICdSe04Te06CdSe =(1/tCdSe04Te06CdSe)*[1
rCdSe04Te06CdSe;rCdSe04Te06CdSe 1];
    %Interface 5
    rCdSeAg =(n5-n3)/(n5+n3);
    tCdSeAg =1+rCdSeAg;
    ICdSeAg =(1/tCdSeAg)*[1 rCdSeAg;rCdSeAg 1];
    %Matriz de propagacion libre
    %Propagacion1 (ITO)
     betaito=(((2*pi*dito)/longitdonda(ok))*n1*(cos(0)));
    Pito=[exp(1i*betaito) 0;0 exp(-1i*betaito)];
    %Propagacion2 (CdS)
    betaCdS=(((2*pi*dCdS)/longitdonda(ok))*n2*(cos(0)));
    PCdS=[exp(1i*betaCdS) 0;0 exp(-1i*betaCdS)];
     %Propagacion3y5 (CdSe)
    betaCdSe=(((2*pi)/ longitdonda(ok))*n3*(cos(0)));
    PCdSe=[exp(1i*betaCdSe) 0;0 exp(-1i*betaCdSe)];
     %Propagacion4 (CdSe04Te06)
    betaCdSe04Te06=(((2*pi)/ longitdonda(ok))*n4*(cos(0)));
    PCdSe04Te06=[exp(1i*betaCdSe04Te06) 0;0 exp(-1i*betaCdSe04Te06)];
    %Propagacion6 (Ag)
    betaAg =(((2*pi*dAg)/ longitdonda(ok))*n5*(cos(0)));
    PAg=[exp(1i*betaAg) 0;0 exp(-1i*betaAg)];

Mpj=IitoCdS*Pito*ICdSCdSe*PCdS*ICdSeCdSe04Te06*PCdSe; %matriz prima en j
Mbpj=ICdSe04Te06CdSe*PCdSe*ICdSeAg*PAg; %matriz biprima en j
tpj=1/Mpj(1,1);  %coeficiente de transmisión
rpjn=-Mpj(1,2)/Mpj(1,1);%coeficiente de reflexión negativo
rbpj=Mbpj(2,1)/Mbpj(1,1);
tjpos=tpj/(1-rpjn*(rbpj*exp(1i*2*betaCdSe))); %coeficiente de transmisión
positivo
alfa=(4*pi*kCdSe04Te06(ok))/longitdonda(ok);%coeficiente de absorcion
%alfa=930818.1898;

    for x=1:1:dCdSe04Te06 %Para espesor de capa activa

E(ok,x)=abs(tjpos*((exp(1i*betaCdSe04Te06*x)+(rbpj+exp(1i*betaCdSe04Te06*
(2*(dCdSe04Te06-x))))))*(Ict(ok)*0.8)); %campo electrico para una forma
de onda
```

```
       %E(lng,x)=abs(tp*((exp(1i*bj*x)+(rjpp*exp(1i*bj*(2*(d-
x))))))*Ic(lng)*(0.8));
        E(ok,x);
        Q(ok,x)=(1/2)*(3*10^8)*(8.85*10^-
12)*alfa*nCdSe04Te06(ok)*E(ok,x)^2;
        %Q(lng,x)=(1/2)*(3*10^8)*(8.85*10^-12)*aj*CdSen(lng)*E(lng,x)^2;
        Q(ok,x);
        G(ok,x)=( longitdonda(ok)*Q(ok,x))/((6.62606957*10^-
34)*(3*10^8));
        G(ok,x);
    end
end

SE=sum(E);%Sumatoria de todos los valores de matriz E.
SQ=sum(Q);%Sumatoria de todos los valores de matriz Q
SG=sum(G);%Sumatoria de todos los valores de la matriz G
GtQW=sum(SG)%Suma total Taza de Generacion de Excitones.

z=1:1:dCdSe04Te06;
lambdamesh = longitdonda'*ones(1,length(z));
zmesh = ones(length(longitdonda),1)*z;

%%%%%%P O I S S O N%%%%%%%%%%%%%%%
Gl=GtQW; %m^-3/s,taza de generacion de excitones 6.5558*10^27
T=300; %kelvin
q=1.6*10^-19; %eV
k=8.617*10^-5; %constante de Boltzman
kT=0.0258;
eo=8.854*10^-14;
mo=9.1039*10^-31; %masa del electron
Vpoisson=600; %mV, voltaje de poisson propuesto
deltaVpoisson=100;

%Información del material tipo P (CdSe)
Na=1*10^15; %cm^-3 1*10^20
Dp=15.25; %cm^2/s, constante de difusión 12
tp=16; %s, tiempo de vida  -----
        %tp= 1.5; % *10^(-8)s tiempo de recombinacion de cargas en CdSe
CELDAS FOTOVOLTAICAS EN GENERACION DISTRIBUIDA ISIDRO ELVIS PEREDA SOTO
         %tp = 5; % us tiempo de recombinacion de cargas en CdSe
niPCdSe=7.07*10^3; %cm^-3, concentración intrinseca cdse
                %niPCdSe = 6*10^13;  %cm ^-3 concentracion intrinseca de
cargas en CdSe subvolumen B II-VI submagnetic compounds springer pdf
ep=10.2; %constante dielectrica
Egp=1.74; %eV,bandgap
mep=0.13; %masa del electron
mhp=0.45; %masa del hueco
mh=[ ];

%Información del material tipo n+ (CdS) mayormente dopado
Nd=5*10^15; %cm^-3 5*10^23
Dn=1.4; %cm^2/s, constante de difusión---
        %Dn=9; %cm^2/s, Coeficiente de difusión de cargas minoritarias
CcS Solar cells pag 74 materials and processing table 4.1
        %Dn=36.4; %cm^2/s, Coeficiente de difusión de cargas minoritarias
CcS Solar cells pag 74 materials and processing table 4.1
```

```
tn=1; %s, tiempo de vida   ----
        %tn = 2; % us tiempo de recombinacion de cargas en CdS
ninCdS=1.6*10^10; %cm^-3, concentración intrinseca cds
                %niCdS = 1.9*10^19; % cm ^-3 concentracion intrinseca de
cargas en CdS en nhttp://www.pveducation.org/pvcdrom/materials/CdS
en=8.9; %constante dielectrica
Egn=2.42; %eV,bandgap
men=0.17; %masa del electron
mhn=0.70; %masa del hueco
me=[ ];
Lp=sqrt(Dp*tp*10^-7); %cm, distancia de difusión de cargas
Ln=sqrt(Dn*tn*10^-9); %cm, distancia de difusión de cargas
npo=(niPCdSe^2)/(Na); %concentración de cargas minoritarias en equilibrio
pno=(ninCdS^2)/(Nd); %concentración de cargas minoritarias en equilibrio
i=1;

while deltaVpoisson > 1

    xp=(((2*ep*eo*Vpoisson*10^-3)/(q*Na*Nd*(Nd+(ep/en)*Na)))^(1/2))*Nd;
%cm
    xn=(xp/Nd)*Na; %cm
    w=xp+xn; %cm

    pQW=pno+pno*(exp((Vpoisson*10^-3)/kT)-1)*exp(xn/Lp)+(Gl*10^-
6)*tp*10^-7; %concentración de cargas en equilibrio
    nQW=npo+npo*(exp((Vpoisson*10^-3)/kT)-1)*exp(xp/Ln)+(Gl*10^-
6)*tn*10^-9; %concentración de cargas en equilibrio

    deltaEc=0.6*(Egn-Egp);
    Nv=(2.51*10^19)*(((mhp*mo)/mo)*(T/300))^(3/2);
    FpEcp=-kT*log(pQW/Nv);
    Nc=(2.51*10^19)*(((men*mo)/mo)*(T/300))^(3/2);
    FcnFn=-kT*log(nQW/Nc);

    Vo=(Egp+deltaEc-FpEcp-FcnFn);
    deltaVpoisson=Vo-(Vpoisson*10^-3);

    Vpoisson=(Vpoisson)+deltaVpoisson;
    mh(i)=pQW;
    me(i)=nQW;
    i=i+1;
end

%deltap = mh(i-1) - mh(i-2);%Calculo de la diferencia de concentraciones
p
%deltan = me(i-1) - me(i-2);%Calculo de la diferencia de concentraciones
n
%dcon = (abs(deltan)+abs(deltap))/(mh(i-1)+me(i-1));

ite=sprintf('Cantidad de iteraciones realizadas:%d',i);
disp(ite)
lim=sprintf('Limite de la zona de agotamiento Xp=%s cm    Xn= %s cm
W=%s cm',xp,xn,w);
disp(lim)
```

```
con=sprintf('Concentración de cargas en x=0, Pn(x)=%s cm^-3     np(x)=%s
cm^-3',pQW,nQW);
disp(con)
poi=sprintf('Vpoisson en la región n y P: %s mV',Vpoisson);
disp(poi)
cuasiv=sprintf('FpEcp=-kT*log(p/Nv)= %s eV',FpEcp);
disp(cuasiv)
cuasic=sprintf('FcnFn=-kT*log(n/Nc)= %s eV',FcnFn);
disp(cuasic)
vpoi=sprintf('Vo= %s V',Vo);
disp(vpoi)


%%%%%%%% C A R A C T E R I Z A C I O N %%%%%%%%%%%%

npoc=Na/(niPCdSe^2) %concentración de cargas minoritarias en equilibrio
pnoc=Nd/(ninCdS^2) %concentración de cargas minoritarias en equilibrio.

Voc=(0.0258)*log((((q*GtQW*10^-
6)*(Lp+Ln))/(q*(((Dp/Lp)*(pnoc))+((Dn/Ln)*(npoc)))))+1) %Voltaje Circuito
Abierto, V
Jsc=q*(Gl*10^-6)*(Lp+Ln) %Corriente Corto Circuito, A
V=0:0.0001:Voc;
J=(((Dp/Lp)*(pnoc*q))+((Dn/Ln)*(npoc*q)))*(exp(V/0.0258)-1)-Jsc;
%Densidad de Corriente, A/cm^2

 plot(V,-J) %Grafica V vs J invertida
grid on
%Title('Grafica J-V')
xlabel('Voltaje en Volts')
ylabel('Densidad de Corriente en A/cm^2')

hold on
JP=abs(V.*J); %Potencia W/cm^2
x=find(JP==max(JP));
JPmax=JP(x)
Vmax=V(x)
Jmax=-J(x)

plot([0 V(x)],[-J(x) -J(x)],'r:+')
plot([V(x) V(x)],[0 -J(x)],'r:+')
Potinc = 0.09; %900/1*10^4; %Eficiencia de conversión de potencia
FF=(V(x)*-J(x))/(Voc*Jsc)
eficiencia=(Vmax*Jmax)/Potinc
Imaxdeseada=0.05 %A

L = 100;    %100 micrometros a  0.01cm % 25 mm a cm
porcentaje=0;
W=0;
if W<L
porcentaje=porcentaje+0.00003;
W=((porcentaje*Imaxdeseada)/(L*(Jmax*10^-8)));  %ancho, cm a um
end
A=((W)*(L)); %area transversal, cm^2 a um^2
Imax=(Jmax*10^-8)*(A); %Coriente maxima, A
```

```
Rmax=Vmax/Imax; %Resistencia, ohms
Pmax=(JPmax*10^-8)*(A); %Potencia maxima

%eficiencia=(Vmax*Jmax)/Potinc;

%%%%%%%R E S U L T A D O S %%%%%%%%%%
fprintf(['Potencia Máxima Pmax = ',num2str(JP(i)*W*L),' W\n',...
'\nVoltaje Máximo = ',num2str(V(i)),' V\nDensidad de Corriente corto
circuito = ',...
num2str(abs(J(i))),' A/cm2\n'])
fprintf(['ancho W %% = ',num2str(W),...
' micrometro\nlargo L  = ',num2str(L),...
' micrometro\nArea A  = ',num2str(A),...
' um^2\nResistencia Máxima Rmax = ',num2str(Rmax),...
' Ohms\nDensidad corriente Máxima Jmax = ',num2str(Jmax),...
' A/cm^2\nCorriente Máxima Deseada = ',num2str(Imaxdeseada*10^3),...
' mA\nCorriente Máxima del dispositivo Imax = ',num2str(Imax),...
' A\nVoltaje circuito abierto Voc = ',num2str(Voc),...
' mA\nFactor de llenado FF = ',num2str(FF),...
' \nEficiencia de Conversión de Potencia = ',num2str(eficiencia),'\n'])
%figure(2)
%clf
%plot(V,-I,'LineWidth',2)
%grid
%xlabel('Voltaje')
%ylabel('Corriente en A')
%hold on
%plot([0 V(i)],[-I(i) -I(i)],'k--')
%plot([V(i) V(i)],[0 -I(i)],'k--')
%text(V(i),-I(i),' Pmax')

%figure(3)
%subplot(2,2,1), plot(SE),xlabel('Profundidad de la capa
activa,d(nm)'),ylabel('Campo eléctrico, E(V/m^2)'); grid() %Grafica 2D de
todas las longitudes de onda)
%subplot(2,2,2), surf(lambdamesh,zmesh,E),ylabel('Profundidad capa
activa,d(nm)'),zlabel('Campo eléctrico, E(V/m^2)'),xlabel('Longitud de
onda,lambda (nm)'); grid()
%subplot(2,2,3), plot(SQ),xlabel('Profundidad de la capa
activa,d(nm)'),ylabel('Qj,Energía promedio disipada Q (W*m^-2)'); grid()
%Grafica 2D de todas las longitudes de onda)
%subplot(2,2,4), surf(lambdamesh,zmesh,Q),ylabel('Profundidad capa
activa,d(nm)'),zlabel('Qj,Energía promedio disipada Q (W*m^-
2)'),xlabel('Longitud de onda,lambda (nm)'); grid()

%figure(4)
%subplot(2,2,1), plot(SG),xlabel('Profundidad de la capa
activa,d(nm)'),ylabel('Gj,Taza de Generación de Excitones,(m^-3 s^-1)');
grid() %Grafica 2D de todas las longitudes de onda)
%subplot(2,2,2), surf(lambdamesh,zmesh,G),ylabel('Profundidad capa
activa,d(nm)'),zlabel('Gj,Taza de Generacion de Excitones (cm^-3 s^-
1'),xlabel('Longitud de onda,lambda (nm)'); grid()

ite=sprintf('\nCantidad de iteraciones realizadas:%d',i);
disp(ite)
```

```
lim=sprintf('Limite de la zona de agotamiento Xp=%s cm    Xn= %s cm
XW=%s cm',xp,xn,w);
disp(lim)
con=sprintf('Concentración de cargas en x=0, PnQW(x)=%s cm^-3
npQW(x)=%s cm^-3',pQW,nQW);
disp(con)
poi=sprintf('Vpoisson en la región n y P: %s mV',Vpoisson);
disp(poi)
exc=sprintf('Generacion de excitones GQW:%G',GtQW);
disp(exc)
fprintf (' \n espesor de ITO =%d nm\n espesor CdS ventana =%d nm\n
espesor CdSe capa activa =%d nm\n espesor CdSe04Te06 pozo cuantico =%d
nm\n',dito,dCdS,dCdSe,dCdSe04Te06);
```

resultados

```
Potencia Máxima Pmax = 0.016577 W

Voltaje Máximo = 0.0001 V
Densidad de Corriente corto circuito = 0.017213 A/cm2
ancho W % = 96.3086 micrometro
largo L  = 100 micrometro
Area A  = 9630.863 um^2
Resistencia Máxima Rmax = 163800 Ohms
Densidad corriente Máxima Jmax = 0.015575 A/cm^2
Corriente Máxima Deseada = 50 mA
Corriente Máxima del dispositivo Imax = 1.5e-06 A
Voltaje circuito abierto Voc = 0.30639 mA
Factor de llenado FF = 0.72562
Eficiencia de Conversión de Potencia = 0.04252

Cantidad de iteraciones realizadas:2
Limite de la zona de agotamiento Xp=7.423126e-05 cm    Xn=
1.484625e-05 cm   XW=8.907751e-05 cm
Concentración de cargas en x=0, PnQW(x)=6.809028e+14 cm^-3
npQW(x)=2.161488e+10 cm^-3
Vpoisson en la región n y P: 6.008377e+02 mV
Generacion de excitones GQW:2.16149E+25

 espesor de ITO =200 nm
 espesor CdS ventana =200 nm
 espesor CdSe capa activa =10000 nm
 espesor CdSe04Te06 pozo cuantico =9 nm
```

Appendix 4

Refractive index and extinction coefficients for the different materials used in heterostructures.

ITO (Indium tin oxide)		
Wavelength λ (nm)	Refractive index n (-)	Extinction coefficient k ()
350	2.2106	0.05851254
360	2.1904	0.05400554
370	2.1708	0.05037373
380	2.1516	0.04748415
390	2.1331	0.04522533
400	2.1152	0.04350352
410	2.098	0.04223955
420	2.0815	0.04136638
430	2.0657	0.04082706
440	2.0505	0.04057307
450	2.036	0.04056298
460	2.0221	0.0407613
470	2.0088	0.04113761
480	1.9961	0.04166571
490	1.9839	0.04232306
500	1.9723	0.04309022
510	1.9613	0.04395034
520	1.9507	0.04488888
530	1.9405	0.04589323
540	1.9308	0.04695242
550	1.9216	0.04805696
560	1.9127	0.04919859
570	1.9042	0.05037013
580	1.8961	0.05156533
590	1.8883	0.05277875
600	1.8808	0.05400567
610	1.8737	0.05524196
620	1.8668	0.05648406
630	1.8602	0.05772886
640	1.8539	0.05897364
650	1.8478	0.06021609
660	1.842	0.06145417
670	1.8364	0.06268614
680	1.831	0.06391049
690	1.8259	0.06512594
700	1.8209	0.06633137
710	1.8161	0.06752584
720	1.8115	0.06870857
730	1.807	0.06987888
740	1.8028	0.07103622
750	1.7986	0.07218014
760	1.7946	0.07331026
770	1.7908	0.07442628
780	1.7871	0.07552799
790	1.7835	0.07661521
800	1.7801	0.07768784

CdS		
Wavelength λ (nm)	Refractive index n (-)	Extinction coefficient k ()
350	2.522	0.3664
360	2.5155	0.3614
370	2.5105	0.3554
380	2.5084	0.3493
390	2.5076	0.3449
400	2.5097	0.3368
410	2.5113	0.3342
420	2.5164	0.3278
430	2.5229	0.3223
440	2.5332	0.3158
450	2.543	0.311
460	2.562	0.3037
470	2.5817	0.2968
480	2.6229	0.2756
490	2.6114	,0.2316
500	2.6797	0.1476
510	2.6115	0.0861
520	2.6079	0.0286
530	2.5537	0.0062
540	2.5236	0.0016
550	2.4921	0.0001
560	2.4715	0
570	2.4571	0
580	2.44	0
590	2.4253	0
600	2.4126	0
610	2.4004	0
620	2.394	0
630	2.386	0
640	2.3774	0
650	2.3718	0
660	2.3645	0
670	2.3578	0
680	2.3574	0
690	2.3475	0
700	2.3407	0
710	2.3378	0
720	2.3344	0
730	2.3299	0
740	2.3257	0
750	2.3223	0
760	2.3197	0
770	2.3161	0
780	2.3183	0
790	2.3105	0
800	2.3097	0

CdSe		
Wavelength λ (nm)	Refractive index n (-)	Extinction coefficient k ()
350	2.767	0.85
360	2.765	0.817
370	2.763	0.781
380	2.724	0.682
390	2.762	0.731
400	2.762	0.709
410	2.764	0.688,
420	2.698	0.602, ,
430	2.764	0.649,
440	2.696	0.566
450	2.773	0.619
460	2.694	0.546
470	2.785	0.583
480	2.703	0.523
490	2.796	0.551
500	2.708	0.496
510	2.708	0.496
520	2.802	0.524
530	2.812	0.506
540	2.728	0.478
550	2.829	0.482
560	2.829	0.482
570	2.76	0.481
580	2.853	0.44
590	2.866	0.402
600	2.758	0.427
610	2.853	0.344
620	2.837	0.311
630	2.74	0.275
640	2.733	0.257
650	2.834	0.268
660	2.733	0.242
670	2.739	0.247
680	2.862	0.27
690	2.755	0.231
700	2.797	0.23
710	2.812	0.23
720	2.856	0.162
730	2.856	-0.0001
740	2.821	-0.0001
750	2.761	-0.0001
760	2.6605	-0.0001
770	2.721	-0.0001
780	2.691	-0.0001
790	2.673	-0.0001
800	2.63	-0.0001

$CdSe_{0.4}Te_{0.6}$		
Wavelength λ (nm)	Refractive index n (-)	Extinction coefficient k ()
350	0.8000	0.5000
360	0.8229	0.5143
370	0.8457	0.5286
380	0.8686	0.5429
390	0.8914	0.5571
400	0.8200	0.5500
410	0.8405	0.5638
420	0.8610	0.5775
430	0.8815	0.5913
440	0.9020	0.6050
450	1.1250	0.4100
460	1.1500	0.4191
470	1.1750	0.4282
480	1.2000	0.4373
490	1.2250	0.4464
500	1.2500	0.3500
510	1.2750	0.3570
520	1.3000	0.3640
530	1.3250	0.3710
540	1.3500	0.3780
550	1.4000	0.3000
560	1.4255	0.3055
570	1.4509	0.3109
580	1.4764	0.3164
590	1.5018	0.3218
600	1.5000	0.2500
610	1.5250	0.2542
620	1.5500	0.2583
630	1.5750	0.2625
640	1.6000	0.2667
650	1.5620	0.2250
660	1.5860	0.2285
670	1.6101	0.2319
680	1.6341	0.2354
690	1.6581	0.2388
700	1.5930	0.2000
710	1.6158	0.2029
720	1.6385	0.2057
730	1.6613	0.2086
740	1.6840	0.2114
750	1.6870	0.1500
760	1.7095	0.1520
770	1.7320	0.1540
780	1.7545	0.1560
790	1.7770	0.1580
800	1.8000	0.1000

Ag (Silver)		
Wavelength λ (nm)	Refractive index n (-)	Extinction coefficient k ()
350	0.1144	1.3196
360	0.0870	1.5198
370	0.0669	1.6890
380	0.0522	1.8412
390	0.0500	1.9741
400	0.0500	2.1035
410	0.0500	2.2325
420	0.0461	2.3478
430	0.0403	2.4566
440	0.0400	2.5528
450	0.0400	2.6484
460	0.0444	2.7511
470	0.0493	2.8545
480	0.0500	2.9476
490	0.0500	3.0391
500	0.0500	3.1309
510	0.0500	3.2233
520	0.0500	3.3157
530	0.0533	3.4101
540	0.0569	3.5074
550	0.0596	3.5974
560	0.0566	3.6786
570	0.0536	3.7598
580	0.0506	3.8409
590	0.0523	3.9249
600	0.0552	4.0097
610	0.0580	4.0944
620	0.0593	4.1768
630	0.0569	4.2543
640	0.0546	4.3318
650	0.0522	4.4094
660	0.0499	4.4869
670	0.0477	4.5658
680	0.0454	4.6447
690	0.0432	4.7236
700	0.0410	4.8025
710	0.0389	4.8811
720	0.0370	4.9596
730	0.0350	5.0380
740	0.0331	5.1165
750	0.0312	5.1949
760	0.0306	5.2718
770	0.0322	5.3463
780	0.0337	5.4208
790	0.0352	5.4953
800	0.0368	5.5698